OKINAWA INSTITUTE OF SCIENCE AND TECHNOLOGY
GRADUATE UNIVERSITY

Thesis submitted for the degree

Doctor of Philosophy

Imaging Electronic States in the Charge Density Wave Material CeTe$_3$

by

Barnaby Robert Magellan Smith

Supervisor: **Yoshinori Okada**

August 2023
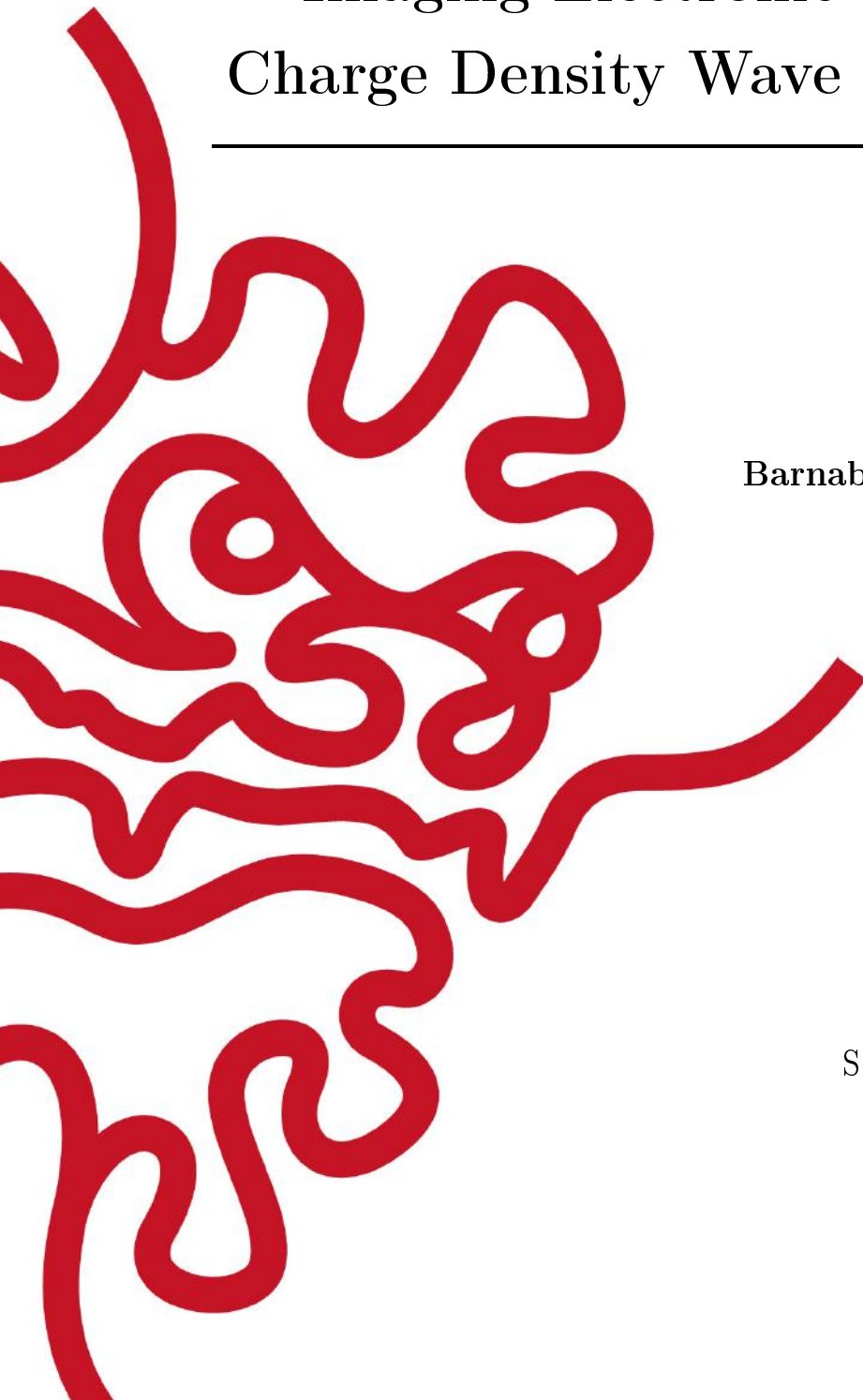
Declaration of Original and Sole Authorship

I, Barnaby Robert Magellan Smith, declare that this thesis entitled *Imaging Electronic States in the Charge Density Wave Material CeTe$_3$* and the data presented in it are original and my own work.

I confirm that:

- No part of this work has previously been submitted for a degree at this or any other university.

- References to the work of others have been clearly acknowledged. Quotations from the work of others have been clearly indicated, and attributed to them.

- In cases where others have contributed to part of this work, such contribution has been clearly acknowledged and distinguished from my own work.

- None of this work has been previously published elsewhere, with the exception of the following:

    - R. Okuma, D. Ueta, S. Kuniyoshi, Y. Fujisawa, B. Smith, c. H. Hsu, Y. inagaki, W. Si, T. Kawae, H. Lin, F. C. Chuang, T. Masuda, R. Kobayashi & Y. Okada. Fermionic Order by Disorder in a van der Waals Antiferromagnet, Scientific Reports, 2020;10(1):15311.
    B. Smith made a significant contribution to the publication, including sample fabrication, data collection and analysis, and manuscript preparation.

Date: August 2023

Signature:

iii

Abstract

The study of condensed phases plays a crucial role in our understanding of physics. In particular, Charge Density Waves (CDWs) are an important phenomenon due to their close connection with a material's fermiology, in addition to their coexistence and competition with superconducting, magnetic, and other exotic phases. Rare earth tritellurides (RTe_3) are a prototypical 2D material system which provide an excellent test platform for investigating these phases and the interplay between them. In this thesis, I will present the first low temperature STM study of $CeTe_3$, with the first comprehensive discussion and simulation of quasiparticle interference (QPI) in any RTe_3 compound. At 4.2 K, we confirm that $CeTe_3$ shows the unidirectional CDW that is present at higher temperatures. We then use SX-ARPES to fit an interacting tight binding model and demonstrate that the observed QPI can be interpreted with JDOS simulations based on this model band structure. We reveal the unexpected result that the QPI arises mainly from scattering between the original bands and their shadow band replicas, with backscattering being relatively suppressed. This pioneering study can be powerfully extended in the future to use QPI measurements to understand the interaction of the CDW state and other phases.

Acknowledgment

No man is an island, and this is especially true in research. The work involved in the production of thesis has been assisted and guided over the course of many years by many hands, and I am eternally grateful to the owners of said hands.

Firstly I would like to thank my supervisor Yoshinori Okada, who's breadth of knowledge of physics, enthusiasm and continual support has been invaluable to my PhD project. His lab has been a welcoming and stimulating place to spend 5 years and I will remember my time here fondly.

I would like to give special mention to Yuita Fujisawa, who has been my mentor and day to day supervisor from my first day in the Quantum Materals Science unit all the way until the present day. His unending patience, intelligence and diligence have taught me almost everything I know about experimental physics. My PhD would not be possible without him and there are not words to express the depth of my gratitude.

The ARPES data presented in this thesis were collected by Dr Yosuke Arai and Professor Takeshi Kondo from the Institute of Solid State Physics, University of Tokyo and Professor Kenta Kuroda from the Graduate School of Advanced Science and Engineering, Hiroshima University and International Institute for Sustainability with Knotted Chiral Meta Matter (WPI-SCKM^2) at Hiroshima University. I thank them for their collaboration and support.

Thanks go to Professor Yuhki Kohsaka for fruitful discussions on the nature of quasiparticle interference, and additionally for his work building and maintaining the SIDAM macro.

I would like to extend my thanks to the Engineering Section at OIST, especially Kieran Deasy, Patrick Kennedy, Mouez Lassoued, Syuta Ikemiyagi and Makoto Kuroda for help with the design and fabrication of mechanical parts. Many thanks also to Kazuma Takada for support with cryogens and gas. I would like to thank Hyung-Been Kang and Serhii Vasylevskyi for X-Ray diffraction support, and Noriko Ishizu for help with scanning electron microscopy. My personal thanks also go to Toshiyuki Kishimoto from Unisoku Co. Ltd. for support during the installation and troubleshooting of our STM over a 2 year period.

I would like thank the current and former members of Graduate School for their help

Abbreviations

- **ARPES** Angle Resolved Photoemission Spectroscopy
- **BZ** Brillouin Zone
- **CDW** Charge density wave
- **CEC** Constant Energy Contour
- **DOS** Density of States
- **EPC** Electron-Phonon Coupling
- **FFT** Fast Fourier Transform
- **FS** Fermi Surface
- **FSN** Fermi Surface Nesting
- **JDOS** Joint Density of States
- **LDOS** Local Density of States
- **NMR** Nuclear Magnetic Resonance
- **QPI** Quasiparticle Interference
- **RKKY** Ruderman–Kittel–Kasuya–Yosida
- **SC-XRD** Single Crystal X-Ray Diffraction
- **SI-STM** Spectroscopic Imaging Scanning Tunnelling Spectroscopy
- **STM** Scanning Tunnelling Microscopy
- **STS** Scanning Tunnelling Spectroscopy
- **SX-ARPES** Soft X-ray Angle Resolved Photoemission Spectroscopy
- **TB** Tight Binding
- **UHV** Ultra High Vacuum
- **XRD** X-Ray Diffraction
- **vdW** van der Waals

Contents

List of Figures

List of Tables

Chapter 1

Introduction

1.1 Motivations

Since the advent of modern physics with De Broglie, Schrödinger and Dirac, humans have had a good idea of how a single electron behaves in a vacuum. In contrast, the behaviour of electrons in multi-particle systems is generally much more complicated, and in these settings inter-particle interactions can result in emergent phenomena that are both fundamentally fascinating and technologically useful. Condensed matter physics is the largest branch of modern physics, and much of it consists of the study of these "strongly-correlated electron materials".

These emergent phenomena manifest through the appearance of electronic condensed phases such as superconductivity, charge density waves, and magnetism. The phases often coexist and compete, with the electronic phase diagram of many important materials resembling a technicolour patchwork. A thorough understanding of the nature and interaction of condensed electronic phases is extremely important due to their huge significance for electronic devices and nanotechnology. However, our actual understanding of these phases and their interactions is incomplete, despite concerted effort on the part of many physicists, chemists, materials scientists, and engineers. One of the difficulties is the overall complexity of an intertwined system, so in order to understand the whole it is rational to break it into parts that can be tackled individually. The part that we have chosen to tackle (or at least chip away at) in this thesis is the phenomenon of charge density waves.

Charge density waves, or more generally charge ordering, is a phenomenon in which electron density in real space is modulated to form a superlattice.[1] This phase transition is found in many low-dimensional systems, and is an important neighbour to superconductivity and colossal magnetoresistance.[2–4] In order to probe this effect without the excessive complexity of many competing phases, we must look for a model system in which to perform our studies.

As will be expanded upon later, charge density waves are largely a low-dimensional phenomenon. As such, we choose to work with van der Waals materials. These materials are inherently 2D in nature, consisting of stacks of covalently bonded sheets held together by weak van der Waals (vdW) interactions. The most tangible example of a vdW material for the layman is graphite, which consists of many graphene sheets tenuously held together by these vdW forces. This is what results in the ability to

abrade the graphite in a pencil onto paper, and also what results in our ability to separate monolayer graphene from the bulk reliably and efficiently using only simple manual techniques.

We therefore seek a material that hosts exotic condensed states, particularly charge density waves, in addition to being a vdW 2D material. After considering many possible materials, we arrive at rare earth tritellurides (RTe_3) as an excellent candidate. They have been studied extensively as a model system for CDW behaviour, hosting competing CDW transitions in addition to exotic magnetism, superconductivity under pressure, and possible unconventional electronic behaviour.[5–8] Recent years have also seen an uptick in research due to the ability to study modifications to the electronic ground state caused by external fields, mechanical stress and ultrashort light pulses, as well as the demonstration of the use of RTe_3 as model system for the study of subatomic particle analogues.[9–16] Now we have a model material, we must ask what experimental technique should we use to study the interacting electrons in the CDW state?

Determining the response of electrons as a function of energy requires us to utilise a single-particle approach, of which there are few. Most probes measure the coupling between a charge or field and the particle of interest, meaning we measure a correlation function rather than the inherent properties of our target.[17] Single-particle probes of special note are angle-resolved photoemission spectroscopy (ARPES) and scanning tunnelling microscopy (STM), which allow the most direct access to information about the electronic band structure (especially for 2D systems and surface states).[18–20] In particular, when we wish to investigate how electronic structure modulates in real space, spectroscopic-imaging scanning tunnelling microscopy (SI-STM) is uniquely suited to the measurement of correlated systems due to its ability to investigate both real and momentum space with unparalleled spatial and energy resolution. This, in combination with its ability to operate in magnetic fields and extremely low temperatures, makes SI-STM an extremely powerful technique to study the cutting edge of condensed matter physics.

In this thesis we detail our pioneering SI-STM studies of the rare earth tritelluride $CeTe_3$, presenting an understanding of the quasiparticle interference in the paramagnetic state. We hope that this provides a strong foundation for future research in the area to build upon, particularly QPI measurements in the magnetic phases of the material.

1.2 Background

1.2.1 Charge Density Waves

Charge density waves (CDW) are a phenomenon wherein the charge carrier density in a system is modified outside the simply expected periodic structure to form a superlattice, which is also associated with a distortion of the underlying crystal lattice.[1] These distortions are a type of condensed phase, and they frequently coexist with other condensed phases such as superconductivity and magnetism in the temperature dependent

phase diagrams of many systems.[21]

Peierls Instability and the Kohn Anomaly

The historical origin of CDWs can be traced to Peierls analysis of 1D chains of atoms, which have a fundamental instability.[22] He showed that given an equally spaced chain of atoms with separation a and Fermi wave number $\mathbf{k}_F$ (figure 1.1a,c), an electronic disturbance with wavevector $\mathbf{q} = 2\mathbf{k}_F = \pi/a$ changes the atomic periodicity of the lattice to $2a$ and opens an energy gap at the zone boundary (figure 1.1b,d). It was asserted that the gain in electronic energy would be larger than the energetic cost associated with restructuring the lattice, resulting in a metal to insulator transition at T_c (also called the Peierls transition).

To understand the mechanism of this distortion we can look at the susceptibility of an electron gas. The response of said electron gas to a time independent potential Φ is given by $\rho^{ind}(\mathbf{q}) = \chi(\mathbf{q})\Phi(\mathbf{q})$ with the potential and the induced charge $\rho^{ind}(\mathbf{q})$ given in terms of their Fourier components. The susceptibility $\chi(\mathbf{q})$ is given by the Lindhard response function, given for dimensionality d by

$$\chi(\mathbf{q}) = \int \frac{d\mathbf{k}}{2\pi^d} \frac{f_{\mathbf{k}} - f_{\mathbf{k+q}}}{\varepsilon_{\mathbf{k}} - \varepsilon_{\mathbf{k+q}}} \tag{1.1}$$

where $f_{\mathbf{k}} = f(\varepsilon_{\mathbf{k}})$ is the Fermi function.[23]

By evaluating this expression for $d = 1$ and $\mathbf{q} = 2\mathbf{k}_F$, we can also determine the mean field transition temperature T_{MF}, below which the uniform charge density becomes unstable:

$$k_B T_{MF} = 1.14\varepsilon_0 \, exp(\frac{-1}{g \, n(\epsilon_F)}) \tag{1.2}$$

where ε_0 is an arbitrary cut-off energy usually taken as ε_F, $n(\epsilon_F)$ is the density of states at the Fermi energy and g is an electron-phonon coupling constant.

In the 1D case, the real part of the susceptibility $\chi(\mathbf{q})$ has a divergent singularity at $\mathbf{q} = 2\mathbf{k}_F$ (fig 1.1e), resulting in the electron gas being unstable to perturbations and forming a standing wave with a wavevector $\mathbf{q}_{CDW} = 2\mathbf{k}_F$. This opens an energy gap at E_F. We can say that the wavevector $\mathbf{q}_{CDW}$ is able to perfectly nest all portions of the Fermi surface since the FS consists of two fixed points at $\mathbf{k}_F = 2\mathbf{k}_F$. When we expand to two dimensions however, this is no longer the case, and a single wavevector cannot perfectly nest all regions of the FS. Indeed when we consider the same susceptibility in two and three dimensions, we see that there is no longer a divergence or even a local maximum in the Lindhard function (figure 1.1e).

This is obviously contrary to experimental observations, where CDWs are well reported in 2D systems. This can be understood in the Peierls picture by the fact that for many CDW systems, the FS is quasi-2D, with regions that are nearly parallel. This results in partial nesting being possible by a single wavevector, giving rise to Peierls transition based CDWs in 2D systems being possible.

Kohn considered the interaction between the electron gas and the lattice phonons, and showed that due to the zero-energy electronic excitations at $2\mathbf{k}_F$, any phonon mode with this wavenumber will be screened, causing renormalisation of the mode to have

Figure 1.1: Illustration of the Peierls Picture of CDW Formation
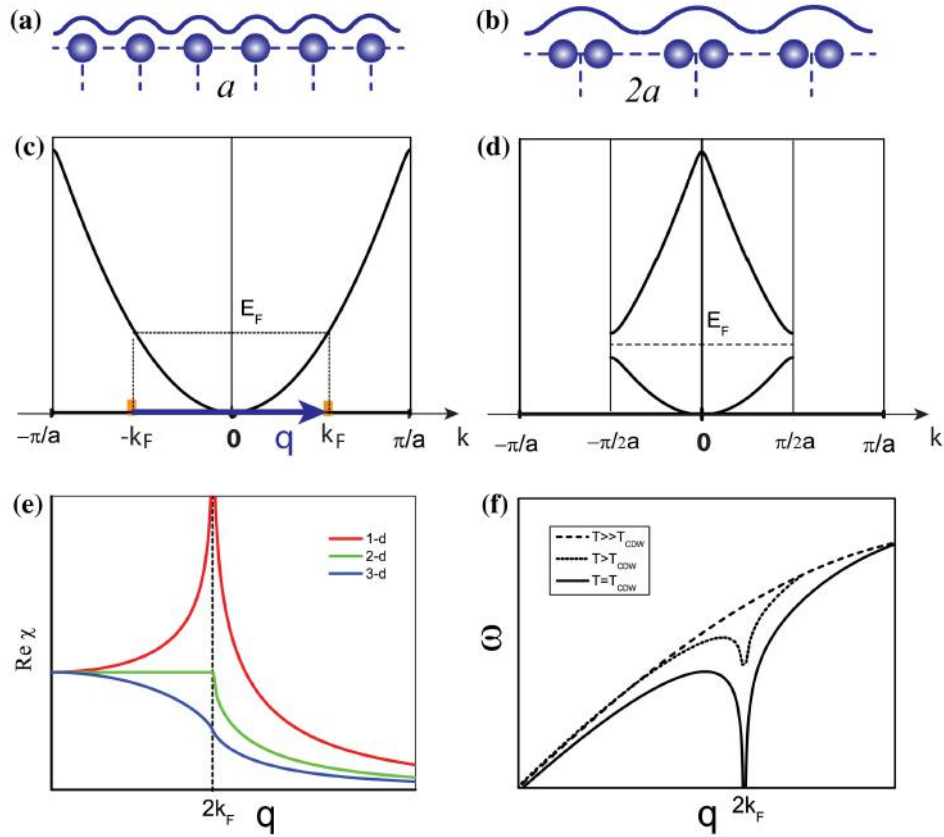
(**a**) 1D atomic chain above T_{CDW} with lattice spacing a (**b**) 1D atomic chain below T_{CDW} with lattice spacing changed to $2a$. (**c**) Free electron band of the 1D chain above T_{CDW}. (**d**) Free electron band of the 1D chain below T_{CDW}, with the gap opening at $\mathbf{k}_F$ (**e**) Plots of the real part of the Lindhard function for 1D, 2D and 3D free electron gas models. (**f**) Phonon energy of a 1D atomic chain at different temperatures. Reproduced from Zhu et al. [24]

a lower energy (referred to as phonon mode softening).[25] This strong renormalisation is known as the Kohn anomaly, and drives the lattice distortion associated with the Peierls transition. The Kohn anomaly is strongly temperature dependant; the phonon dispersion of the 1D atomic chain at different temperatures is shown in figure 1.1f. At or below T_{CDW}, the energy of the phonon mode with wavenumber $2\mathbf{k}_F$ becomes zero, resulting in the static lattice distortion. At temperatures just above T_{CDW}, there is a sharp dip in the phonon dispersion but no static lattice restructuring. This frozen phonon mode leads to a second order phase transition into the CDW state.

Beyond the Peierls Model

We can summarise the key signatures of the Peierls model as: Fermi surface nesting in the electronic structure, a Kohn anomaly in the phonon dispersion, a structural transition and a metal-insulator transition. In some real CDW materials, such as the

quasi-1D compound TTF-TCNQ, all of these signatures are present and the Peierls model appears to be a good fit.[26−30] In other real CDW materials however, we find these signatures are not present and it becomes clear that the Peierls model alone fails to fully explain CDW phenomena.

For example, in the prototypical 2D CDW material $NbSe_2$, we see the presence of the Kohn anomaly and a structural transition, but Fermi surface nesting, a sharp peak in the Lindhard function, and a metal-insulator transition are all absent.[31−38] While it could be proposed that this is a consequence of moving from 1 dimension into 2, this is negated by studies of 2D Sn/Ge films that show all the hallmarks of Peierls transition behaviour.[39−42]

This issue was investigated in a seminal paper by Johannes and Mazin [43], who illustrate that Fermi surface nesting may not play as large a role as previously thought. Their calculations show that divergence of the susceptibility is extremely sensitive to even small deviations from perfect Fermi surface nesting conditions. The extreme fragility of the Peierls condition, even for a 1D chain of sodium atoms, means that it is unlikely to have a strong bearing on the properties of real materials. They propose that the nesting condition is therefore not the sole driving force behind CDW formation, and instead a **q**-dependant electron-phonon coupling (EPC) is responsible. In this scenario, the nested Fermi surfaces either play a supporting role or are completely incidental. This is supported experimentally via phonon measurements in $NbSe_2$.[33,44] While FSN and EPC are both forms of electron-lattice interaction, they fundamentally differ in that FSN involves elastic scattering and EPC inelastic.[45]

Much of the interest in charge ordering phenomena is thanks to its association with superconductivity, particularly in the high temperature superconducting copper oxides. The cuprate superconductors have a perovskite structure, with 2D CuO_2 planes sandwiched between charge reservoir layers.[46,47] They are considered to have a quasi-2D electronic structure. Different charge ordering phenomena have been demonstrated, with stripe phase charge order in $La_{1.6−x}Nd_{0.4}Sr_xCuO_4$, a chequerboard phase and short range charge order in $Bi_2Sr_2CaCu_2O$, and long range charge order in $YBa_2Cu_3O_{6+x}$.[3,48−55] The origin of this charge order is also not simple however; it has been shown that neither FSN nor EPC are the direct cause of charge order/charge density waves in the cuprates.[45,56] STM results indicate that an unconventional density wave phase exists, with electron correlations playing an important part.[57]

Zhu et al. [45] have proposed that these inconsistencies can be explained by classifying CDWs into three classes based on the driving force behind their formation: type I CDWs arise from Fermi surface nesting and follow the hallmarks of the Peierls transition, type II CDWs arise from **q**-dependant electron-phonon coupling and type III CDWS arise from neither FSN nor EPC, with their root cause being currently unclear but likely originating in electron-electron correlations.

1.3   Materials

In order to investigate the behaviour of charge density waves, we need a suitable material to test. As will become clear in the following section, the rare earth tritellurides provide an ideal testbed in which to perform our experiments.

1.3.1   Rare Earth Tritellurides

Crystal Structure

Whilst rare earth tritellurides (RTe_3) have been known as a stable crystallographic phase since at least the 1960s, modern interest in their properties as a quantum material hosting interesting condensed phases began with Dimasi et al. in 1994.[58–61] Since then, the family have shown themselves to be an excellent model system for investigating exotic condensed phases including charge density waves, superconductivity, and exotic magnetism in a vdW coupled 2D system.[5]. The currently extant members of the family consist of R = Y, La, Ce, Pr, Nd, Sm, Gd, Tb, Dy, Ho, Er, and Tm. Even though Y is not technically a rare earth element, it forms a stable +3 oxidation state and YTe_3 has similar properties to RTe_3, hence its inclusion in the family. Eu bucks the trend of the rare earth series and preferentially forms Eu(II) rather than Eu(III), meaning $EuTe_3$ is not known. $YbTe_3$ and $LuTe_3$ have also not been observed experimentally, likely due to the rare earth elements great rarity and expense rather than because they are not possible to make. The trend of heavier rare earth elements forming more unstable RTe_3 compounds also means that $YbTe_3$ and $LuTe_3$ would be extremely air sensitive. Pm forms a stable +3 oxidation state and so $PmTe_3$ is chemically feasible, however Pm is highly radioactive and extremely rare, so $PmTe_3$ has not been demonstrated and would be extremely difficult/expensive/hazardous to make. All RTe_3 compounds are unstable in air, with the surface oxidising over the course of a few hours in atmosphere.

Figure 1.2: Summary of Rare Earth Tritelluride Element Dependent Properties
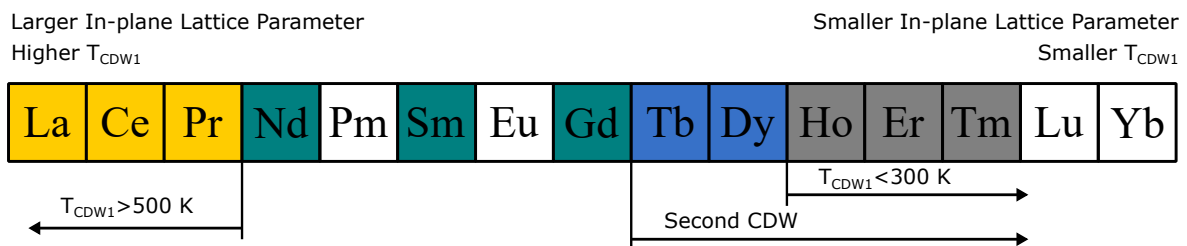
Lanthanide series of the periodic table, elements with coloured boxes are known to form stable tritelluride compounds. Trends across the series are indicated. Adapted from Straquadine [62]

The RTe_3 family crystallises into a layered structure, shown in figure 1.3a. This structure consists of a rare earth telluride slab which is flanked on either side by a square net tellurium sheet. These Te sheets are separated from a neighbouring Te sheet by a van der Waals (vdW) gap, forming a bilayer. This vdW gap results in the material being considered quasi-2D due to the weak coupling between the layers, which can

be observed experimentally through the extremely anisotropic electrical resistivity and almost perfect $\sec(\theta)$ angular dependence of de Haas-van Alphen oscillations.[61,63,64] It additionally makes cleavage of the crystal to form a charge neutral Te surface extremely facile and repeatable. Note that due to crystallographic convention, the b axis of this crystal system is out-of-plane.

Figure 1.3: Crystal structure of RTe_3
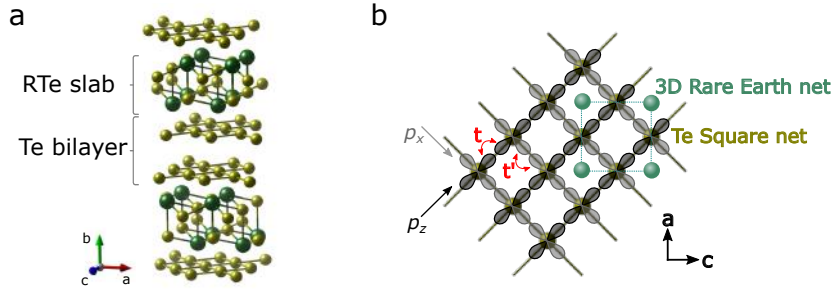
(**a**) side view of the crystal structure of RTe_3 with the RTe slab layer and the Te bilayer indicated. (**b**) Top view of the crystal with the inequivalent Te and Rare earth square nets indicated. The p_x and p_z chains that define the electronic structure near the Fermi level are labelled in black and grey, and the t and t' parameters used to construct the tight binding band structure model are marked in red. Images produced using Vesta software.[65]

The crystal structure of RTe_3 has orthorhombic symmetry, with the space group *Cmcm*. This instance of the space group has a glide plane along one in-plane axis of the vdW gap but not the other, which results in the inequivalence of the **a** and **c** crystal axes. This presents as a difference of a few tenths of a percent in the lattice constant of the axes, with **c** being larger than **a**. This difference increases as the rare-earth element becomes lighter.[66]

Crystals of RTe_3 can be grown either through the flux melt or binary melt method, which are described in detail in the methods section.

Electronic Structure and Charge Density Waves in RTe_3

We discuss the full electronic structure theory and calculations in detail in the methods section, however we will briefly show the results here in order to inform the discussion of the Fermi surface nesting in CDW formation. The metallic electronic behaviour of the RTe_3 compounds derives from the Te sheet, with the RTe slab being insulating. The main effect of the rare earth element substitution is through the size of the ion, with heavier R elements causing a smaller lattice constant and therefore a monotonic change in the behaviour of the electrons originating from the Te p-orbitals.

The band structure of RTe_3 is modelled as chains of collinear p-orbitals, which after hybridisation form square pockets centred around the Γ and K points of the 2D Brillouin zone. After band folding effects due to the different symmetry of the 2D Te net and the overall 3D structure, we arrive at the Fermi surface shown in figure 1.4a. The nesting vector $\mathbf{q}_{CDW}$ is indicated, and the band folding creates a second, equivalent nesting vector $\mathbf{q}'_{CDW}$ between the original and the folded bands, with $\mathbf{q}_{CDW} = \mathbf{c}^* - \mathbf{q}'_{CDW}$

(where $\mathbf{c}^*$ is the unit cell wavevector for the 3D periodic structure). These nesting vectors correspond to a unidirectional stripe phase CDW, known as CDW1. While these vectors are shown for the k_x direction, it can be seen that a nesting condition will also exist in the k_y direction, allowing for a secondary perpendicular CDW phase known as CDW2.

Figure 1.4: Fermi Surface and CDW Transition Temperature vs Lattice Parameter a for the RTe$_3$ Family
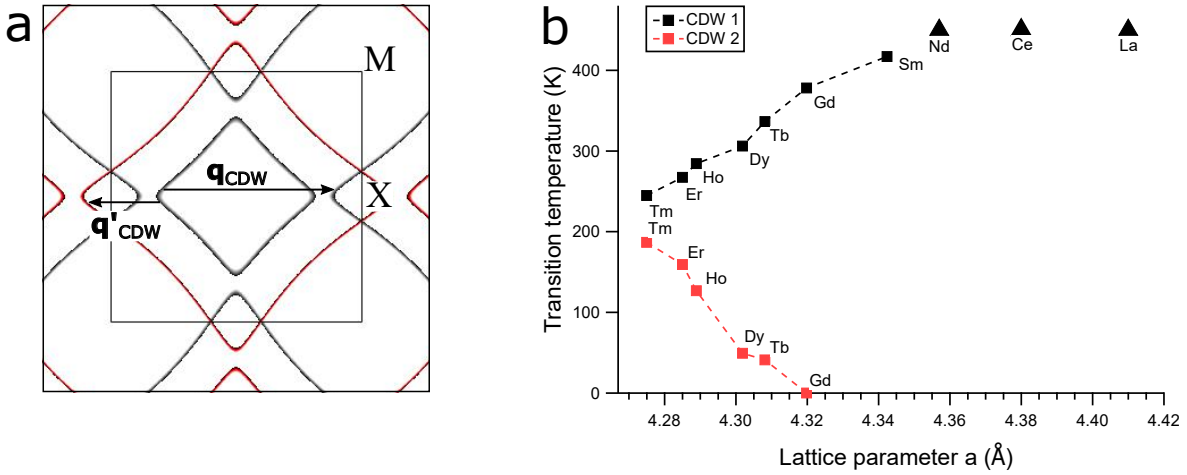
(a) Tight binding Fermi surface of RTe$_3$, with the equivalent CDW nesting vectors indicated with arrows. Inner black square indicates the first 3D Brillouin zone with high symmetry points indicated. (b) CDW transition temperature vs lattice parameter a. Nd, Ce and La transition temperatures are known only to be above 400 K. Black markers indicate the transition temperature for the unidirectional CDW1, and red markers indicate the transition temperature for the orthogonal CDW2.

All RTe$_3$ compounds show the unidirectional CDW1 with the wavevector $\mathbf{q}_{\mathrm{CDW1}} = (\frac{5}{7})\mathbf{c}^*$, which occurs below the transition temperature T_{CDW1}. This transition temperature monotonically varies, with the lowest being approximately 240 K for TmTe$_3$ and increasing to above 500 K for LaTe$_3$. For the rare earth elements Tm-Tb, the a-axis CDW2 occurs at lower temperatures, with a wavevector of $\mathbf{q}_{\mathrm{CDW2}} = (\frac{1}{3})\mathbf{a}^*$. The phase diagram for the CDW transition temperatures as a function of the lattice parameter a is shown in figure 1.4b, with the decrease in T_{CDW1} corresponding with an increase in T_{CDW2}, both of which are a function of increasing chemical pressure due to the lanthanide contraction decreasing the ionic radii of the rare earth element moving across the series. This is supported by the fact that applying physical pressure can mimic the effect of chemical pressure and modify T_{CDW} in the expected manner.[67]

The full band ab initio band structure calculated using the linear muffin tin orbital approximation is shown in figure 1.5.[68] The Fermi surface in 1.5a is very similar to that calculated from the tight binding method, with the addition of a bilayer splitting of the pockets from the inequivalent Te planes. The inner diamond shaped pockets with strong nesting are shown in 1.5b, and the X pockets in 1.5c. The band structure plot in 1.5d shows the very slight dispersion along the b axis, and demonstrates that the inner diamonds are hole-like pockets and the outer sheets are electron-like.

Figure 1.5: LMTO ab initio calculation for LuTe$_3$
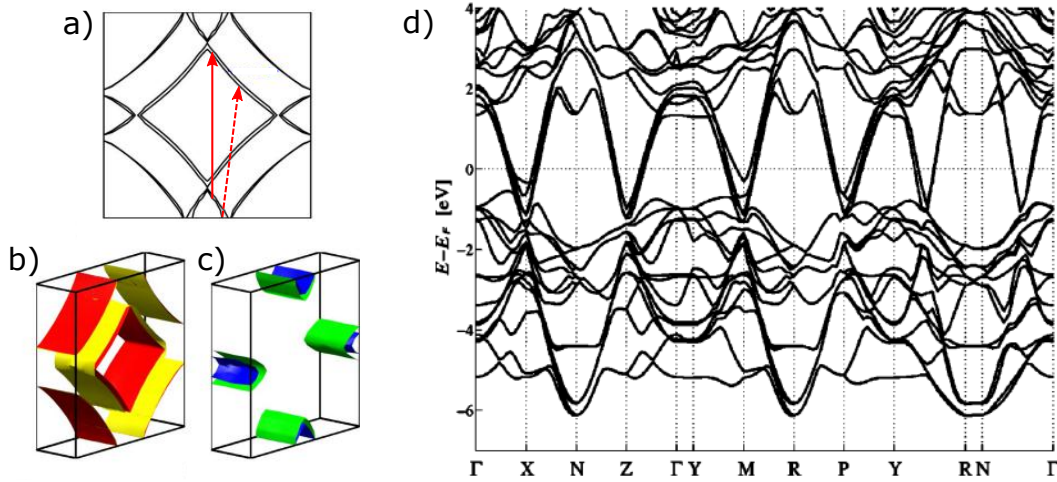
Linear muffin tin orbital approximation calculated band structure for LuTe3. **(a)** Fermi surface **(b)** Inner diamond shaped sheets **(c)** pockets at the X points **(d)** Band structure plot. Reproduced from Laverock, J., et al. "Fermi surface nesting and charge-density wave formation in rare-earth tritellurides." Physical Review B 71.8 (2005), used with permission of the American Physical Society

There are multiple nesting vectors available in the RTe$_3$ Fermi surface. If there was no curvature of the bands, a single wavevector would perfectly nest the parallel chains. The finite curvature of the chains however creates a situation where a wavevector exists that perfectly nests one of the bands but poorly nests the other, and a second wavevector exists that does an acceptable but imperfect job of nesting both bands. The former wavevector is indicated with the solid red arrow in 1.5a, and the latter with the dashed arrow. Calculations of the momentum independent Lindhard susceptibility show that in a realistic system the former vector is preferable and results in the formation of a stripe phase at higher temperatures, and the latter vector and the formation of a chequerboard phase being preferential if the transition temperature is lower.[69]

This nesting vector however disagrees with the experimentally observed $\mathbf{q}_{CDW}$, with a difference of 20% for DyTe$_3$, indicating that this simple Peierls nesting picture may not be accurate for RTe$_3$.[70] More rigorous calculations of the nesting condition of RTe$_3$ were performed by Johannes and Mazin [43] that take into account the momentum dependence of the EPC. The results concur with their conclusions about CDW formation in general (as discussed earlier), with the FSN playing a minor role compared to the EPC. In their calculations for the electronic structure of CeTe$_3$, the peaks in the low energy limit of the imaginary part of the susceptibility (which is alternately called the nesting function, as it defines the FS nesting strength) do not correspond with the strongest peak positions in the real part of the susceptibility (which is what defines the observed CDW). They argue that because of the nature of the FS of CeTe$_3$, the strongest peaks in the imaginary part originate from levels at exactly the Fermi energy, and these quickly die off and are not observed in the real part due to the states near but not at E_F having a higher contribution due to stronger nesting. In the real system, this

perfect nesting vector is actually slightly imperfect, resulting in inhomogeneity of the gap in $\mathbf{k}$-space, and the gap not being centred at E_F.[71,72] This EPC driven picture is also supported by Raman scattering and calculations performed on $ZrTe_3$ by Hu et al. [73], as well as inelastic X-ray scattering performed on $TbTe_3$ by Maschek et al. [74].

While the first CDW has been studied fairly extensively, the secondary CDW is more mysterious. The resistivity change crossing T_{CDW} is very slight, and no phonon softening is observed for $\mathbf{q}_{CDW2}$.[62]

The competing $\mathbf{q}_{CDW}$ and $\mathbf{q}'_{CDW}$ vectors in RTe_3 have been used by Wang et al. [16] to detect the axial Higgs mode, a fundamental particle analogue. Through the careful use of angle-dependent polarised Raman scattering, they were able to visualise the constructive and destructive interference of the quantum pathways involved in the charge order formation in $LaTe_3$ and $GdTe_3$, providing evidence that the CDW order in RTe_3 is unconventional due to its nodal gap.

All of the rare earth elements (with the exception of Y and La) have local moments, and these moments order magnetically at low temperatures in all RTe_3 compounds. The magnetic properties of the system have been investigated through magnetisation, heat capacity, electrical resistivity, neutron diffraction and inelastic neutron scattering measurements.[7,8,13,64,75–80] The family show long range antiferromagnetic behaviour below the Neel temperatures, with many of the members showing multiple transition temperatures from paramagnetic to antiferromagnetic via one or more intermediate states. The primary magnetic interaction is generally considered to be direct exchange or superexchange (as opposed to RKKY) due to the physical separation of the magnetic rare earth moments and the itinerant Te sheet electrons, however resistivity measurements indicate a non-zero RKKY interaction in $CeTe_3$.[5,64]

Angle-resolved photoemission experiments performed by Brouet et al. [71] comprehensively investigated the $\mathbf{k}$-resolved electronic band structure of the RTe_3, demonstrating the gap opening and Fermi surface reconstruction associated with the CDW phase. A more recent experiment by Chikina et al. [81] takes advantage of improved momentum resolution and measures the Fermi surface of $NdTe_3$, demonstrating the unexpected result of a CDW not only removing FS elements but also adding new ones, which are also observed in quantum oscillation experiments.[13,14,63,82,83] Other ARPES studies have been carried out with different foci, such as specifically looking at the f-electrons of the rare earth, or investigating the possible occurrence of a topological nodal line in the band structure.[6,9,84–88]

Raman spectroscopy performed by Chen et al. [89] demonstrated the thickness dependence of the T_{CDW1} in $GdTe_3$, increasing from 377 K in bulk to 431 K for a 10 nm layer. This increase is attributed to the reduced chemical pressure in the out-of-plane direction. Optical spectroscopy by Hu et al. [90] indicates a possible secondary gap feature in the lighter RTe_3 elements, which are expected to have only a single gap from the CDW1 phase. They propose that this is evidence for a third CDW order which has until now not been observed by diffraction or scanning probe methods.

STM topographic investigations have demonstrated the large real space modulation of the electronic structure and revealed the nature of the surface lattice distortions. Fang et al. [91] performed measurements on $TbTe_3$ in the CDW2 phase, but due to the unknown nature of CDW phenomena in RTe_3 at the time they assigned the chequerboard modulation peaks as a unidirectional CDW plus a surface dimerisation. Tomic

et al. [92] and Ralević et al. [93] have performed STM experiments on $CeTe_3$ at 77 K and 300 K respectively, showing clearly the CDW1 stripe phase. They also demonstrate wavevector mixing effects in the Fourier transforms of the topography, as well as presenting a preliminary discussion of area averaged dI/dV spectroscopy. Fang et al. [94] used STM to investigate the disruption of the CDW phase in $ErTe_3$ caused by Pd intercalation. Xu et al. [95] grew $GdTe_3$ on a graphene/SiC substrate using molecular beam epitaxy. They demonstrated via STM the persistence of the CDW state at the monolayer limit, and showed the first images of a QPI pattern on an RTe_3 surface (however they do not discuss the origin of the QPI signals).

The non-equilibrium behaviour of the CDW phases have also been investigated by pump-probe studies, revealing a non-equilibrium CDW along the a axis in $LaTe_3$ that competes with CDW1. This non-equilibrium CDW has a different wavevector to the equilibrium low temperature CDW2, reflecting a different origin.[11] The dynamics of the relaxation of this non-equilibrium CDW indicate the presence of topological defects.[12]

RTe_3 is often taken as a prototypical CDW system due to the simplicity of the Te square net, with the coupling of the itinerant Te sheet electrons and the rare earth f-electrons assumed to be negligible. Recent ARPES, neutron diffraction, resonant x-ray scattering and magnetoresistance measurements however indicate that this is not the case and a finite coupling between them exists.[7,83,96,97] ^{125}Te NMR studies from Chudo et al. [98] show the spin polarisation of the CDW in $CeTe_3$ due to the coupling between the Ce local moment and Te conduction electrons.

Despite the large number of studies performed, it is evident that the exacting nature of the CDW in RTe_3 is still unclear. In order to further study the CDW phase and its interactions with other phases we choose to focus on $CeTe_3$.

1.3.2 Cerium Tritelluride $CeTe_3$

$CeTe_3$ a perfect candidate for the investigations that we envision due to the advantageous transition temperatures exhibited by its condensed phases. The material exhibits the unidirectional CDW stripe phase at all measured temperatures to date, with STM confirming the CDW stripe phase down to 77 K and transport measurements showing no evidence of a secondary CDW transition down to 1.8 K.[64,92] Furthermore, the material undergoes magnetic transitions from paramagnetism to an intermediate phase at 3.1 K, and from the intermediate phase to long range antiferromagnetism at 1.3 K.[78]

Investigation of fermion behaviour at low energy scales necessitates the use of low measurement temperatures due to the increased energy resolution that they provide. Ideally, these low-temperature measurements of $CeTe_3$ would be conducted in the CDW1 phase, which is comparatively simpler than the CDW2 phase; we would also like to able to perform measurements in and out of the magnetically ordered phases. At 4.2 K $CeTe_3$ exhibits CDW1 whilst in a paramagnetic phase. By lowering the temperature to 1.7 K and 0.3 K, we can perform measurements of the CDW in the intermediate and long range antiferromagnetic phases respectively. These temperatures can be readily achieved for extended periods of time using liquid helium, as detailed in methods section 2.1.3.

As well as the ability to work at these low temperatures, our experimental technique

of choice must fulfil several more criteria. Firstly, it should be able to measure the electronic structure with high resolution in both real and reciprocal space in order to investigate the periodicity of the CDW. Secondly, the ability to work in external magnetic fields is desirable in order to tune the interaction between the CDW and the magnetic phases.

The only technique that suitably satisfies these conditions is spectroscopic imaging scanning tunnelling microscopy, which has proven itself in the last 40 years as an extremely powerful technique for the study of condensed matter. We will detail the background and methods of this approach in the next chapter, before delving into our results.

Chapter 2

Methods

2.1   Scanning Tunnelling Microscopy

This subsection will briefly cover quantum tunnelling and its application in STM, instrumentation, and techniques used in STM experiments. This is intended as a short overview, as detailed explanations and full derivations for all expressions would make this section far too long, so I will mostly present only the final result with a short explanation. For a fuller understanding, the books "Introduction to Scanning Tunnelling Microscopy" by J.C. Chen and "Scanning Probe Microscopy" by B. Voightländer both present a complete overview of the subject, with Chen being more rigorous on the quantum tunnelling theory and historical background, and Voightländer being more modern and digestible (the tunnelling theory in this section follows the approximate order given in Voigtländer).[99,100]

2.1.1   Tunnelling Theoretical Framework

Scanning tunnelling microscopy (STM) is a form of scanning probe microscopy which takes advantage of quantum tunnelling between a metallic tip and a sample with a voltage bias applied between them. Introduced in 1981 and winning the Nobel prize in 1986, it allows for not only atomic resolution topography but also measurement of the local density of states (LDOS).[101,102] The basic principle behind STM relies upon quantum tunnelling of electrons through a potential barrier. As electrons have a very low mass, a considerable part of their behaviour is wavelike. This results in an ability to "tunnel" through a potential barrier. This can be reworded as the fact that if a metallic tip is bought close to a surface with a voltage bias applied between them, their electron wavefunctions can overlap, with a finite probability (given by Fermis golden rule) of electrons being able to travel through the vacuum gap and causing a current to flow. From a very first approximation, we can take the 1D example of a plane wave (our approximation for a 1D electron) that is travelling rightwards towards a square energy barrier of height V_0 and width d. By inserting the expression for a plane wave into the time-independent Schrödinger equation (and knowing that the wave function and its derivative must be continuous) we can obtain solutions for the left hand side of the barrier (the original plane wave plus its reflection), inside the barrier (an exponentially decaying function) and the right hand side of the barrier (which is also a plane wave).

Using the handy fact that wavefunctions are probability density functions, we can therefore easily find the probability that our wave (electron) has tunnelled through the barrier, which after some simplification gives us the transmission factor

$$T = \frac{16E(V_0 - E)}{V_0^2}exp - 2d\sqrt{\frac{2m}{\hbar^2}(V_0 - E)} \tag{2.1}$$

where d is the barrier width, m is the electron mass and V_0 is the barrier height. This is proportional to the electrical current detected by our STM instrumentation, as discussed below. For energies lower than the barrier height ($V_0 > E$), we can see that the T depends exponentially on the width of the barrier d, which is analogous to the tip-sample separation in an STM experiment. This is what gives us the very high positional sensitivity that we utilise to image surfaces on an atomic scale. This 1D approximation is useful to show the dependence of measured current on barrier height, however it is missing many elements of the real system, such as normalised wavefunctions, voltage difference between tip and sample and the electronic structure of the tip and sample being different.

In order to get a more realistic expression for the tunnelling current, we turn to time dependant perturbation theory, following in the footsteps of Bardeen.[103] We assume weak coupling between the tip and sample states, meaning we can take Fermis golden rule for scattering from an initial to a final state, given by

$$\omega_{init \rightarrow final} = \frac{2\pi}{\hbar} |M_{final,init}|^2 \delta(E_{final} - E_{init}) \tag{2.2}$$

with the $|M_{final,init}|$ being the tunnelling matrix element. To arrive at the current, we sum over all pairs of final and initial states, and multiply 2× the charge of an electron (to account for spin degeneracy), giving us

$$I = \frac{4\pi e}{\hbar} \sum_{init,final} |M_{final,init}|^2 \delta(E_{final} - E_{init}) \tag{2.3}$$

Currently, the matrix element is dependent on the wavefunctions of final and initial states, however we can approximate that they are instead dependent on energy. After doing so, and replacing sums of initial and final states with sample and tip densities of states ρ_{sample} and ρ_{tip}, the total current flowing between the tip and sample when integrated over all energies is given by:

$$I = \frac{4\pi e}{\hbar} \int_{-\infty}^{\infty} \rho_{tip}(\varepsilon)\rho_{sample}(\varepsilon) |M(\varepsilon)|^2 d\varepsilon \tag{2.4}$$

but there are several assumptions that we can use to simplify this. Firstly, thermal broadening of the edge of the Fermi-Dirac distribution is given by $k_B T$, and the measurements in this thesis are all at temperatures below 5 K, giving a thermal broadening of less than ≈ 0.415 meV. We can therefore make the assumption that the Fermi function is a sharp step edge (known as the low temperature approximation), which means we can integrate only over the range between the applied bias eV and the Fermi level. Secondly, we assume that we are using a tip that has a flat density of states in the range we're studying, so that term can be taken outside the integral (we achieve this

in practice by using clean tungsten tips). Thirdly, by assuming that we're in the low voltage regime ($eV << \phi$), the transmission factor $|M(\varepsilon)|^2$ is independent of energy and can also be taken outside the integral. This gives us

$$I \approx \frac{4\pi e}{\hbar}\,\rho_{tip}\,|M(\varepsilon)|^2 \int_{-eV}^{0} \rho_{sample}\,d\varepsilon \,\approx\, const. \int_{-eV}^{0} \rho_{sample}\,d\varepsilon \qquad (2.5)$$

This is the 1D approximation for the tunnelling current measured in STM, which we can see is dependent only on applied bias and sample density of states. As the matrix element containing exact wavefunctions is difficult to solve, we can use the semi-empirical WKB approximation for a square barrier to determine the value of $|M(\varepsilon)|^2$, which is given by[104]

$$|M(\varepsilon)|^2 = exp - 2\frac{d}{\hbar}\sqrt{2m\varphi} \qquad (2.6)$$

where d is the tip-sample separation, m is the electron mass and φ is the height of the barrier (some mixture of the tip and sample work functions). We can see that this approach gives us the same result as the 1D approximation given in eq. 2.1. Bardeen developed the theory in 1D for metal-insulator-metal junctions rather than for STM (due to the fact that STM hadn't been invented yet), so Tershoff and Hamann took the theory and adapted it for STM. They modelled the surface as a plane wave and the tip as a point source, and showed that the current I is proportional to only the sample local density of states (LDOS) for a given energy E_F and tip position $\mathbf{r}_t$. They further showed that this relation holds even if the tip has finite size, with the caveat that the tip wavefunction still has s-wave symmetry. This approximation is frequently used for ab-initio simulations of STM measurements, with good results.[99]

When eq. 2.5 is evaluated (taking m as the free electron mass and $\phi \approx 4.5eV$), we can see that for a 1 Å change in d, the current changes by approximately an order of magnitude. This also accounts for the high lateral resolution, as one atomic distance of $\sim$2.5 Å changes the transmission factor by a factor of 150, meaning that the majority of the current carried though the tip is carried by the "last atom" on the tip surface.

All the tips used in this thesis are made from electrochemically etched polycrystalline W wire, which is then annealed in UHV by electron bombardment before conditioning on a reconstructed Au(111) surface.

2.1.2 STM Measurements

Topography

By maintaining a constant bias between tip and sample, the only variables in Eqn. 2.5 that can change are sample LDOS ρ_s and separation d. By using a feedback circuit to keep I constant while scanning in the x and y directions, a contour map of the integrated LDOS between the applied bias and E_F is made. If we make the assumption that the LDOS is homogeneous across the entire surface (which is only true for some pure metals with a perfect surface), this constant current contour map is a pure z-height topograph. For other materials, it is an image of the LDOS variation across the surface, which allows us to directly measure the electronic structure of the

Figure 2.1: Scanning Tunnelling Microscope Diagram
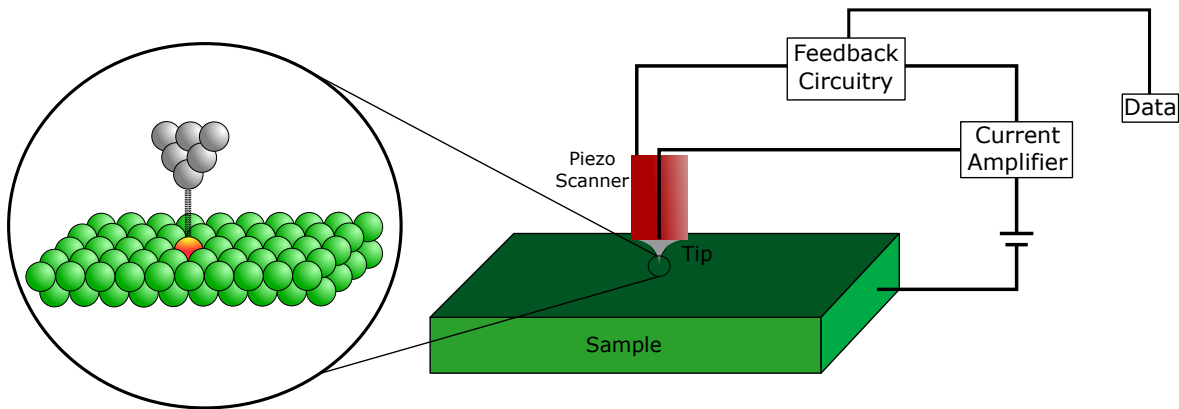
Simplified cartoon of an STM experimental setup

surface. A good example of the STM topography being inequivalent to the pure z-height topography is the imaging of a CO molecule adsorbed on a metal surface, which appears as a depression in surface due to the lower DOS.[105]

While it may be tempting to apply a high bias to achieve a strong signal and get information about the whole DOS up to some arbitrarily high level, in reality this would mean that the assumptions used to calculate the current would break down, and we would also begin to damage the sample.[104] We usually measure somewhere in the range of 1 meV to 1 eV for metallic samples, which gives us a tip-sample separation of 0.4 to 1 nm. When done properly, this measurement results in images of the surface of the sample with clear atomic resolution in real space. These topographs can also then be Fourier transformed to yield reciprocal space information about the surface of the sample, which is useful for determining averaged or repeating features such as atomic separation, surface symmetry and characterisation of density waves.

Spectroscopy

As the STM current signal is the integral of the LDOS w.r.t. bias voltage, we can recover the LDOS at a single energy by measuring the differential dI/dV. Known as Scanning Tunnelling Spectroscopy (STS), this lets us observe the LDOS with excellent real space resolution, as well as allowing us to observe both above and below the Fermi level E_F by sweeping the voltage range above and below zero bias. This is practically realised in the STM by holding the Z height constant, varying the tip-sample bias and measuring the current. While the measured I/V curve could be numerically differentiated, instead we directly measure the derivative dI/dV (or any higher order differentials if desired) using the lock-in technique. This consists of measuring I as a function of bias V with a small AC modulation reference signal added on to the DC bias. The measured current signal will then have an oscillation at the same frequency, which can be extracted using a lock-in amplifier. The amplitude of this induced oscillation is proportional to the derivative of the I/V curve. The main advantage of this technique is that the lock-in amplifier retains the signal at the same frequency as the known reference signal and discards all other frequencies, resulting in an excellent S/N ratio

even in extremely noisy backgrounds. By recording this over a range of bias values, we acquire a full dI/dV curve.

The energy resolution in STS in the low voltage limit determined by the thermal broadening of the Fermi step function and the modulation voltage V_{mod}. Assuming the thermal broadening is FWHM of a Gaussian sample DOS peak, the energy resolution is therefore given by $\Delta E \approx \sqrt{(2eV_{mod,RMS}) + ((0.28meV/K) \cdot T)^2}$

Spectroscopic Image Mapping and Quasiparticle Interference

We can also combine these two techniques by taking a spectrum at each point of a grid to produce topographic maps of the electronic structure of materials, which when analysed can show us changes in **k**-space over the course of changing bias (we can view this 3D dataset either as a grid of dI/dV curves at every x,y value or as a series of LDOS maps with varying bias voltage).[104] This mapping technique (sometimes known as Spectroscopic Imaging STM, or SI-STM) is also used with quasiparticle interference (QPI) experiments, which have been used with great success to investigate the mechanisms underlying unconventional superconductivity and topological insulator surface states.[106–111]

As a qualitative overview, electronic quasiparticles in surface states can be elastically scattered off point defects, step edges and other inhomogeneities such as magnetic vortices that provide a scattering potential (see figure 2.2).[50,112–114] Scattering from these potentials result in electron standing waves (Friedel oscillations) caused by the interference of the scattered states. This was first demonstrated by Hasegawa and Avouris [115] on Au(111) and Crommie et al. [113] on Cu(111), and is visually well demonstrated by the work of Crommie et al. [116] in confining these standing waves into a "quantum corral". The spatial period of these standing waves is given by $\frac{2\pi}{\mathbf{q}}$, and the Fourier transform of the image of these standing waves results in a direct image of the scattering vectors **q** in reciprocal space.[104,117]. As these vectors give information about the band dispersion, by analysing their distribution and tracking their changes w.r.t. energy we can measure the band dispersions of materials with our STM.

The simplest way of simulating a QPI pattern is through the Joint Density of States (JDOS) approximation, which is based on the idea that for a given constant energy contour (CEC) and assuming all scattering processes are equally likely, whichever **q**-vectors with the direction and magnitude that connect the most pairs of points of the CEC will be the dominant scattering vectors in the QPI pattern.[17,104,118,119] We start with the knowledge that a a periodic potential in a crystal produces a set of Bloch eigenstates described by $\Psi_{\mathbf{k}}(\mathbf{r}) = e^{i\mathbf{k}\cdot\mathbf{r}}u_{\mathbf{k}}(\mathbf{r})$. $u_{\mathbf{k}}$ is a periodic function commensurate with the crystal lattice. The individual eigenstates have momentum **k** and energy $\epsilon(\mathbf{k})$. The LDOS of this system is therefore given by

$$\rho(E,\mathbf{r}) = \sum_n |\Psi_n(\mathbf{r})|^2 \, \delta(E - \epsilon_n) \tag{2.7}$$

with n being the quantum numbers for eigenstates with energy ϵ_n. We can see that as the this involves the absolute square of the wavefunction, we lose any **k** information and so spectroscopic mapping STM of a perfect crystalline surface will provide us no dispersion, only the periodic function $|u_{\mathbf{k}}(\mathbf{r})|^2$.

Fortunately for those of us that would like to measure the electron dispersions, crystals are often not perfect, and contain defects/impurities (and if they don't, it can be possible to introduce them).[120] These defects can cause elastic scattering of the Bloch eigenstates, resulting in new states which are combinations of original states that have different momenta $\mathbf{k}$ but the same energy $\epsilon(\mathbf{k})$. This mixing results in a new wavefunction for the system, given by

$$
\begin{aligned}
|\Psi_n(\mathbf{r})|^2 &= \left| e^{i\mathbf{k_1}\cdot\mathbf{r}} a_1 u_{\mathbf{k1}}(\mathbf{r}) + e^{i\mathbf{k_2}\cdot\mathbf{r}} a_1 u_{\mathbf{k2}}(\mathbf{r}) \right|^2 \\
&= \left| a_1 u_{\mathbf{k1}}(\mathbf{r}) \right|^2 + \left| a_2 u_{\mathbf{k2}}(\mathbf{r}) \right|^2 + \left(a_1 u_{\mathbf{k1}}(\mathbf{r}) a_2^* u_{\mathbf{k2}}^*(\mathbf{r}) e^{i(\mathbf{k_1}-\mathbf{k_2})\cdot\mathbf{r}} + c.c \right)
\end{aligned}
\tag{2.8}
$$

As we now have $\mathbf{k}$ outside the absolute square terms, this means that our measured local density of states now has $\mathbf{k}(\mathbf{q})$ dependence. This manifests as modulations at $\mathbf{q} = \mathbf{k_1} - \mathbf{k_2}$, which corresponds to a real space wavelength of $\lambda = 2\pi/\mathbf{q}$.

Simon et al. [121] demonstrate that the energy resolved density of states can be written as

$$
\rho(E, \mathbf{r}) = \frac{1}{2\pi} \int_{\mathbf{q}} g(E, \mathbf{q}) e^{i\mathbf{q}\cdot\mathbf{r}} \, d\mathbf{q}
\tag{2.9}
$$

where $g(E, \mathbf{q})$ is the Fourier component of the LDOS at the wavevectors $\mathbf{q} = \mathbf{k_2} - \mathbf{k_1} + \mathbf{G}$ ($\mathbf{G}$ being the reciprocal lattice vector). This is given by

$$
g(E, \mathbf{q}) = \frac{1}{4\pi} \int \int_{E(\mathbf{k_1})=E(\mathbf{k_2})=E} f(\mathbf{k_1}, \mathbf{k_2}, \mathbf{G}) \delta(\mathbf{q} - \mathbf{k_1} + \mathbf{k_2} \pm \mathbf{G}) \, d^2\mathbf{k_1} d^2\mathbf{k_2}
\tag{2.10}
$$

The term $f(\mathbf{k_1}, \mathbf{k_2}, \mathbf{G})$ is a weight factor depending on matrix elements and the nature of defects, but we can assume that defects have various symmetries and that this function is slowly varying, meaning we can treat it as a constant. With this and Wiener-Kinsche theorem (the Fourier transform of spectral density is the autocorrelation function), we arrive at the result that the autocorrelation of the constant energy contour is the calculated JDOS quasiparticle interference pattern.[121]

This JDOS approximation works well for simple metals where the constant energy contour of the band dispersion is a isotropic centred around centre of the Brillouin zone. It has also been used with great success when combined with ARPES and more complex models in cuprate, pnictides, and ruthenate superconductors.[50,122–128]. In addition, it has been used in the investigation of heavy fermion systems, unconventional 2D systems, semiconducting nanowires and topological materials.[109,110,129] The main disadvantage of using the JDOS approximation is that it is a phenomenological model and disregards the spin texture of the system, so it fails to reproduce details of systems where the spin texture is an essential feature of the Fermi surface.

Whilst angle-resolved photoemission spectroscopy (ARPES) is a more direct measure of electron band dispersions, SI-STM has a few distinct advantages. Firstly, ARPES is inherently incompatible with external magnetic fields due to the fact it is measuring the momentum and direction of electrons that are photoemitted from the material, meaning any external field would modify their path and render the measurement impossible. Secondly, due to the fact that there must be an optical window from the photon source to the sample being measured and fact that the sample is constantly

being irradiated by the photons used for measurement, there is a practical lower limit on measurement temperatures (usually on the order of a few kelvin). Thirdly, ARPES cannot measure unoccupied states as there are no electrons to be photoemitted, which is trivial for an STM to measure by using a bias voltage above the Fermi level.[110] Fourthly, ARPES generally has limited spatial resolution, meaning it cannot investigate real-space inhomogeneity the electronic properties of a sample.

Figure 2.2: Quasiparticle Interference on the Au(111) Surface
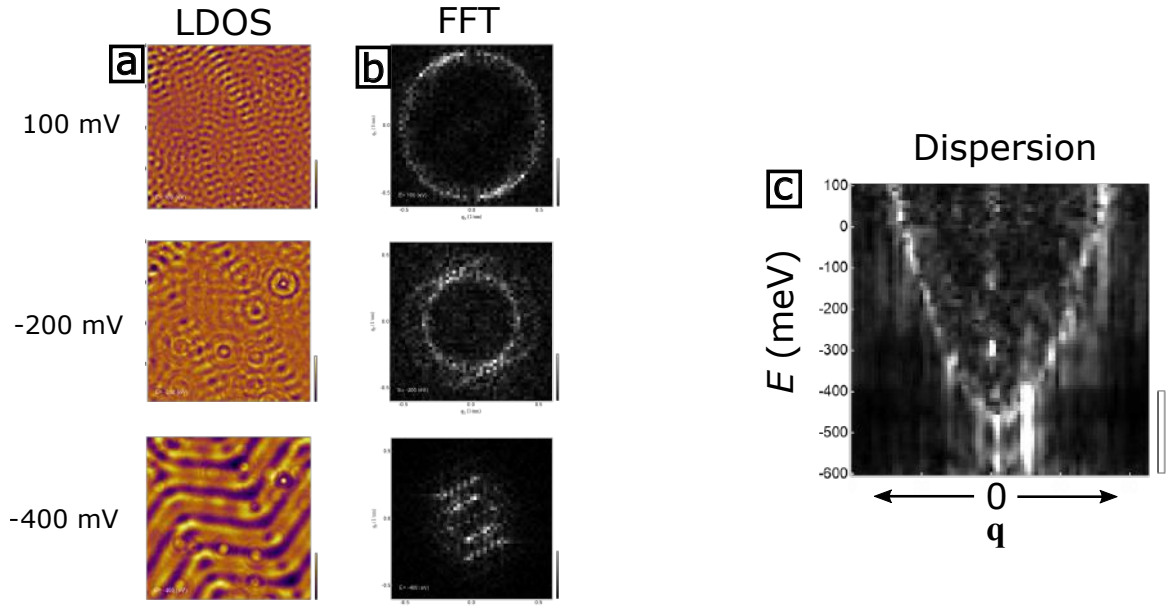
Images produced during QPI measurement of a gold reference sample. (**a**) LDOS maps of a reconstructed Au(111) surface at various energies. (**b**) **q**-space maps (Fourier transforms of LDOS maps) at various energies, showing slices of the dispersing parabolic band. (**c**) Energy against **q** band dispersion, where **q**=2k.

Figure 2.2 shows the images produced during QPI measurement of a gold reference sample. The Freidel oscillations (standing waves) produced by scattering from impurity potentials are clearly visible in the LDOS (dI/dV) maps shown in (a). The LDOS maps at various energies are Fourier transformed to produce the **q**-space dispersions shown in (b). The diagonal features seen in these images are artefacts caused by the herringbone structure and are not from the band structure, as evidenced by the lack of energy dependence. The parabolic dispersion plotted in (c) has its base at approximately -425 mV, matching photoemission measurements which give an E_0 of -408 mV.[130]

2.1.3 STM Practical Considerations

Whilst the theory presented above is robust, in practice a high performance STM is a very sensitive beast, and much consideration needs to be put into its design and installation to ensure that it can operate effectively. The following section details a few

of the main design solutions taken to mitigate the obstacles faced when taking such precise measurements.

Ultra High Vacuum

STM is an extremely surface sensitive technique; we need surfaces that are both well defined and clean. Well defined surfaces are normally determined during the sample selection/preparation phase by having materials with one or more charge neutral cleave planes. Cleanliness however is more tricky, as it requires both good sample preparation and the use of Ultra-High Vacuum (UHV). A surface must have no adsorbed gas molecules on its surface to be defined as atomically clean. In a regular atmospheric environment there is always a layer of water vapour and gas molecules on any surface. We therefore perform all experiments in UHV, defined as pressure below 1×10^{-8} Torr. At atmospheric pressure, the number of molecules that impact a given square centimetre of surface is about 3×10^{23} per second, creating a monolayer in 3×10^{-9} seconds. At 10^{-10} Torr (our usual operating pressure), the number of incident molecules becomes 3×10^{10}, giving us several days before a monolayer forms to perform experiments. This can also be extended in the case of small enclosed systems such as an STM head, as in the high vacuum regime molecules have a much longer mean free path (on the order of kilometres for UHV) and effectively move independently in a straight line, so if there is not a direct "line of sight" to the surface it is less likely that molecules will impinge upon it.

Achieving this vacuum requires multiple stages of pumps, with a rough pump used to take the pressure down to their operating limit of approximately 10^{-3} Torr. A turbomolecular pump is then used to bring the pressure down even lower, to around 10^{-7} Torr. Ion pumps and titanium sublimation pumps can also be used to maintain vacuum once the pressure is low enough. Due to the chamber walls having adsorbed water molecules, the chambers must be baked at 100-150 °C for a few days to desorb the molecules, after which the pressure should be 10^{-10} Torr and experiments can commence.

STM Head Design

If we want to take measurements with sub-angstrom precision, we obviously need to be able to position the sample and tip relative to each other with this level of precision. This is done in practice using piezoelectric motors, whose precision is extremely high (assuming the voltage source is close enough to ideal). Modern STMs usually have the resolution determined by the precision of digital to analogue converters used to produce the piezo driving signals, which can control the tip position within a few picometres accuracy. In practice the exact nature of the STM tip is a larger limitation, but resolutions of tens of picometres are achievable.

There are two stages of piezo motors, one set for coarse motion to position the sample and tip, and another stage for scanning motion. The tip is set into the top of the scanning tube piezo motor, which operates via the variable extension and bending of multiple piezo stacks attached to a tube. By extending all the piezos on the tube equally, the tip is extended. By extending one side more than the other, a bending

motion of the tube occurs and the tip moves laterally. It is of note that this causes the tip to move laterally in a sweep rather than linearly, which needs to be accounted for when taking large area scans. The scanning tube piezo in our system has a maximum x,y range of approximately 1.2 μm and z range of 350 nm at 4 K.

Low Temperature Operation

As discussed above, low temperature operation allows much greater energy resolution in STS measurements, as well as allowing access to the lower energy phases that we are interested in. In usual operation, we can have stable measurements at 4.2, 1.7 and 0.3 K, and intermediate/higher temperatures can be attained through the use of a heating element attached to the head that is connected to a feedback circuit to maintain equilibrium. For 4.2 K, we simply seal the exhaust of the dewar, which means as the helium bath boils it forms a positive pressure head relative to atmosphere. This forces liquid helium through the sipper tubes into the 1 K pot and charcoal pump cooling line, with a fully opened needle valve to allow unimpeded flow. In this operation mode the 1 K pot is full of liquid helium at close to atmospheric pressure, resulting in a stable temperature of 4.2 K.

For lower temperatures, we take advantage of the fact that the boiling temperature of a liquid is dependent on the pressure of the system, with lower pressures resulting in lower boiling temperatures. By closing the needle valve and pumping the exhaust line of the 1 K pot with a powerful vacuum pump, we can reduce the boiling temperature of ^{4}He to 1.6 K. In practice we actually have the needle valve opened very slightly to replenish the ^{4}He that vaporises, but not fully open so that the 1 K pot is completely flooded with "hot" ^{4}He at 4.2 K. This gives an operating temperature of 1.75 K.

The 300 mK mode operates using the same principle of pumping a liquid to reduce its boiling point, and all we have done is switched the liquid from ^{4}He to ^{3}He. ^{3}He has a boiling point of 3.2 K at atm. pressure, and once we pump on it we get stable temperatures of 300 mK. Due to the rarity and expense of ^{3}He, we have a completely closed system to avoid any losses, with the charcoal pump being the active pumping element. At low temperatures, the extremely high surface area of the activated charcoal within the pump "wants" to adsorb all the ^{3}He atoms, giving a strong pumping effect. When all the liquid has evaporated and adsorbed onto the pump (on the timescale of 5 days), the temperature of the system again rises. In order to release the atoms from the charcoal pump again, all we have to do is heat the pump to 50 K to desorb into gas and then re-condense into liquid, and then we can continue low temperature experiments.

The design of the cooling system (fig 2.3) is set up in such a way that the STM head is thermally coupled to the ^{3}He pot, which through the use of the heat switch can be either decoupled from the 1 K pot (in 300 mK operation) or coupled (in 1.7 K or 4.2 K operation, and also when recondensing ^{3}He).

A detailed description of the design of the pumping station used to control the temperature of the system is given in appendix 5.2.

Figure 2.3: ^{3}He Refrigerator Diagram
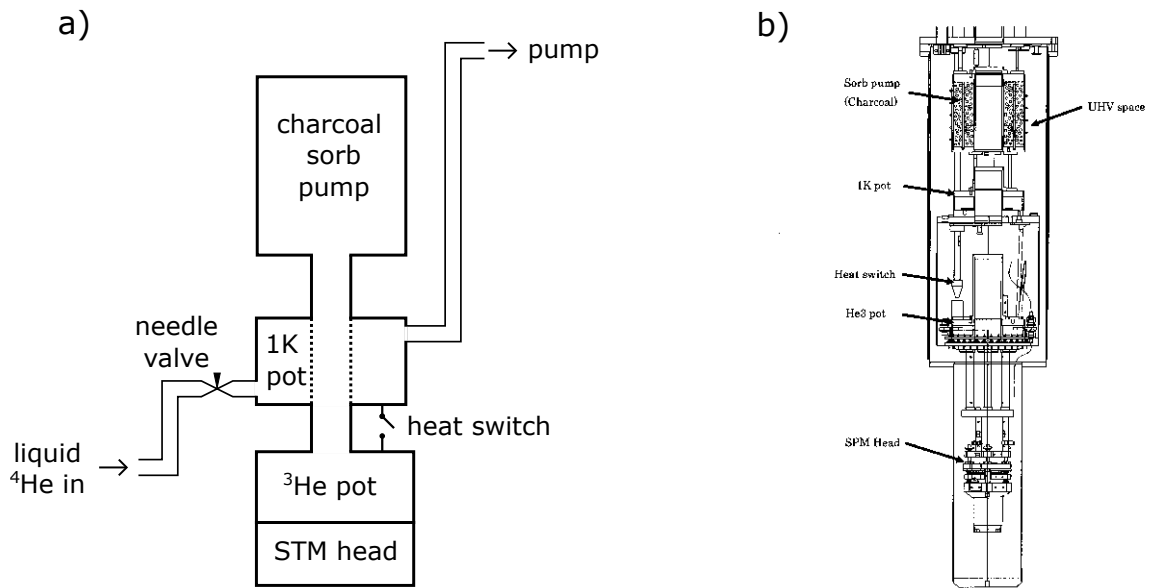
(a) Cartoon showing the basic layout of the ^{3}He sorbtion pump cooling system (not to scale). (b) Schematic of the Janis/Unisoku system used for the measurements in this thesis. Reproduced with permission.

Vibration Isolation

Due to the very small length scales involved in the measurement, the tip and sample need to be held in as close to a vibration-free environment as possible. We first design the STM head to be as rigid as possible to prevent any internal vibration from occurring, which also means we have reasonable positional repeatability when withdrawing and re-extending the tip. This is basically considered as a spring with a very high (>10 kHz) harmonic frequency. We then surround the STM head in various nested stages of vibration isolation (figure 2.4), with each stage designed to disallow the passage of vibrations of differing frequencies. From the inside out, the first layer of isolation is the fact that the STM head is suspended on springs, which blocks high frequency vibrations from passing to the head. The next stage is the pneumatic air cushions that the entire STM apparatus floats on. This air cushion sits atop a large (approx $2 \times 2 \times 4$ m) concrete block, which itself is separated from the floor by commercial pneumatic active dampers. The floor is connected directly to bedrock (luckily our geographic area is seismically inactive and has no trains or other heavy industry nearby). This entire arrangement sits inside its own sound isolation room, with all pumps and other sources of vibration either turned off during measurement or situated outside the room via the use of feedthroughs.

The suppressing of harmonic oscillations in the mechanical beams, pneumatics, springs etc. of the instrumental setup is an arduous but necessary step that must be undertaken during the initial setup of an instrument. This can be done using sandbags or tactically placed weights, using rubber sheets/blocks or glass fibre as mechanical

Figure 2.4: Vibration Isolation for STM Instruments

sound isolation room/Faraday cage

pneumatic
floating table

LHe dewar

insert

concrete blocks

springs

STM
head

pneumatic
active dampers

concrete floor directly on bedrock
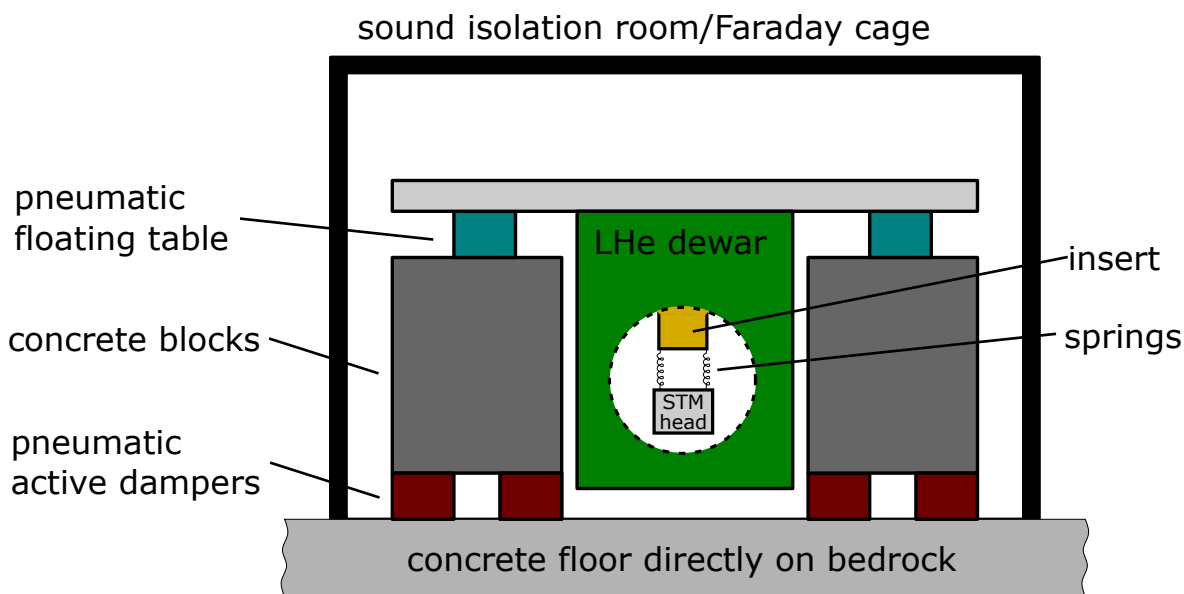
Schematic of the vibration isolation setup for the STM head

dampers, by tuning the length/spring constant of springs, adjusting pneumatic air pressure, firmly clamping all cables and gas tubes to heavy weights, as well as more specific solutions to individual problems. The general idea is that if there is a harmonic at some stage, it should be suppressed as much as possible, and then the vibration transfer function of a later stage should allow no/minimal passage of that frequency.

Electronics

The input and output signals to an STM measurement are all electronic, and so the correct design of the electronic circuitry is critical to an effective measurement.

In normal operation, the bias is usually fixed at either a set value or a predetermined sweep. The input signal to the feedback circuit is the current, which is converted to a voltage by a pre-amplifier. The output is the tip position (via the scanning piezo tube voltages). This feedback operates via a proportional/integral loop design which is integrated into the commercial Nanonis Mimea SPM controller that we use for control of our STM. The hardware also incorporates analogue to digital and digital to analogue converters to allow us to use a computer to record and control the analogue input/output signals from the tunnel junction. Due to the high voltage required to drive the piezo stacks (up to 200 V), there is also a high voltage amplifier. The lock-in amplifier used to record dI/dV curves is also incorporated.

A common source of noise in measurements is 50/60 Hz electronic noise (depending on where in the world you are), caused by the AC modulation of the electrical grid. This can be caused directly by the voltage supply to the instruments, but this is easily mitigated by using a voltage regulator/cleaner between the mains voltage and the instrument. A more insidious way that this noise can get into the measurements is via inductive coupling to conductive loops in the experimental setup. This is more

Figure 2.5: STM Electronics Signal Flow Diagram
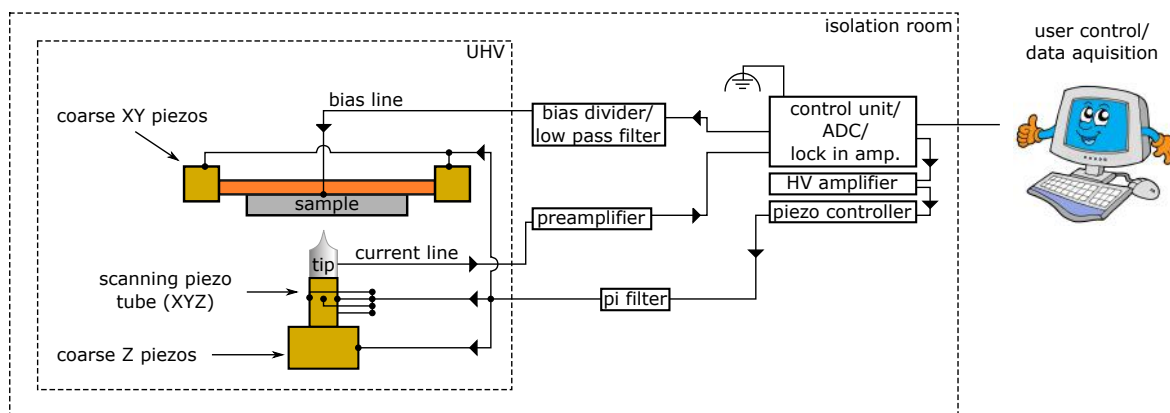
Signal flow graph of the electronics used in STM measurements

tricky to combat but it can be eliminated by containing the instrumental setup within a Faraday cage, turning off all unnecessary electronics within the Faraday cage when performing measurements, and by eliminating ground loops. All circuitry going to the STM head also incorporates low pass filters/pi filters to filter out high frequency RF noise.

In addition to the above steps, it is important that all wires that go from outside the instrument (at room temp) to the STM head (at low temp) are correctly thermalised to prevent heat leakage to the measurement.

2.2   Crystal Growth and Sample Preparation

In order to most accurately measure the physics of a surface, we require a surface which has been either prepared or cleaned in ultra-high vacuum to ensure that we have no adsorbed gas molecules or dust on the surface, and that the surface has not been oxidised or reacted with the insidious moisture that is present in ambient conditions. This is achievable in two main ways, namely by cleaving or by thin film methods. The first involves taking a crystal with a charge neutral cleave plane and mounting it on the sample holder with a conductive paste. While the sample is still in atmosphere a solid pin or a piece of sticky tape is then attached to the surface, and the sample is then placed in the UHV chamber (via the use of a small load-lock chamber, with the same concept as an airlock). After pumping down the system, a mechanical feedthrough is used to "flick" the pin or pull off the tape, which results in cleavage of the sample and the exposure of a clean surface. It is important to cleave the crystal a few times before attaching the pin, as this hopefully eliminates any cleave planes that are slightly cleaved already in atmosphere which may not be visible but will have intercalated gas molecules between the layers.

With thin film methods, the sample to be measured can either grown on a substrate in-situ or grown and then transferred to the measurement chamber via a vacuum suitcase. Alternately, a capping layer of an element or compound can be grown over the

top of the sample that can either be removed via annealing or sputtering in the measurement system, or in some cases if the capping layer does not affect the measurement it can be left on.[131,132]

Figure 2.6: Sample Mounting for STM
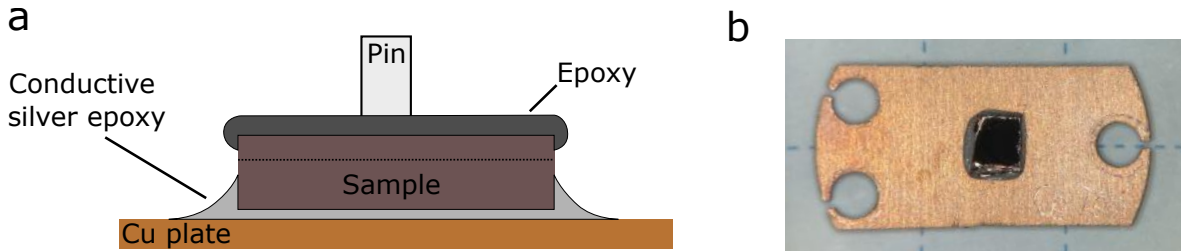
(**a**) schematic of mounting samples for STM measurements. (**b**) image of typical mounted single crystal after cleaving, showing flat shiny surface.

In the case of RTe$_3$, the most favourable method to grow crystals suitable for STM is via the self-flux method. The initial study that reported the growth of RTe$_3$ was Dimasi et al., who grew SmTe$_3$ using LiCl and RbCl as flux.[61] While this method successfully produces crystals, it leaves flux contamination even with the use of several washing steps after growth. To avoid this problem, Ru et. al demonstrated the use of self-flux growth, wherein tellurium is both a constituent of the crystal and the solvent that the crystal grows from.[64]. This is an effective method for all members of the RTe$_3$ family.

The method that we have found most effective for growing high quality single crystals of CeTe$_3$ (and other RTe$_3$ compounds) is as follows. We first prepare chunks of elemental Ce by removing the storage oil and surface oxidation inevitably present on commercial Ce. We then weigh out a 1:30 ratio of Ce:Te and seal them under vacuum in pre-cleaned quartz tubes with quartz wool that acts as a filter (see fig 2.7). The tubes are then placed metal side down in a furnace, heated to 950 °C for 24 hr to liquefy all elements and then cooled to 500 °C over the course of 7 days. During this cooling process, RTe$_3$ crystals form as solids in the liquid Te solvent/flux. We then quickly remove the tube from the furnace, flip the tube and put it in a centrifuge while the Te is still in liquid form. This forces the liquid Te through the filter to the other end of the tube whilst the CeTe$_3$ crystals are blocked. Upon opening the tubes, we are (normally) greeted by large, high quality single crystals sat atop the quartz wool filter. There is a very thin layer of Te flux which remains on the crystals which needs to be removed to prevent contamination of the STM and unpredictable sample cleavage. We do this either with a razorblade (taking care not to apply pressure or shear force to the crystal) or via the use of a post-growth annealing step.

The samples are then mounted on copper plates ready to be put in the STM preparation chamber.

Figure 2.7: Flux Growth Catch Filter Method

Cartoon illustrating flux growth using quartz wool as a catch filter.
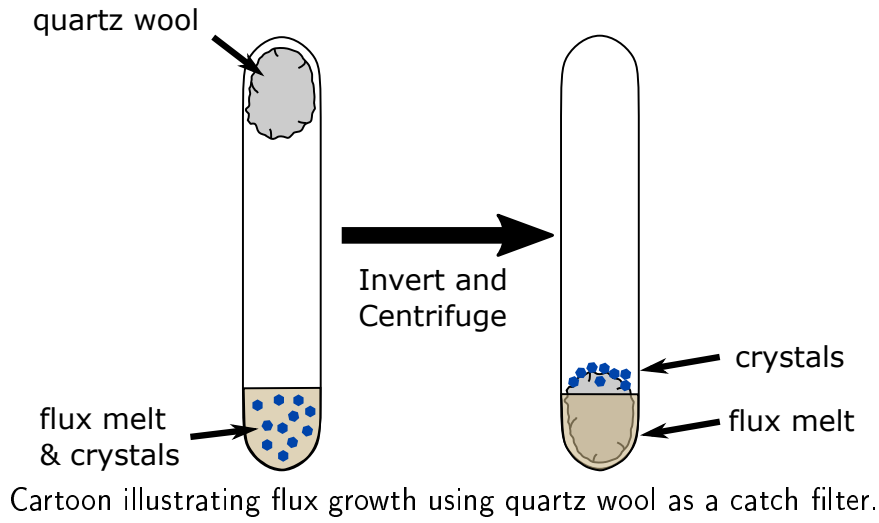
2.3   ARPES Measurements

Whilst ARPES measurements are not the main focus of this thesis, because we worked with collaborators to refine our tight binding band structure model I will briefly overview the working principle behind ARPES.

Figure 2.8: Key Concepts in ARPES
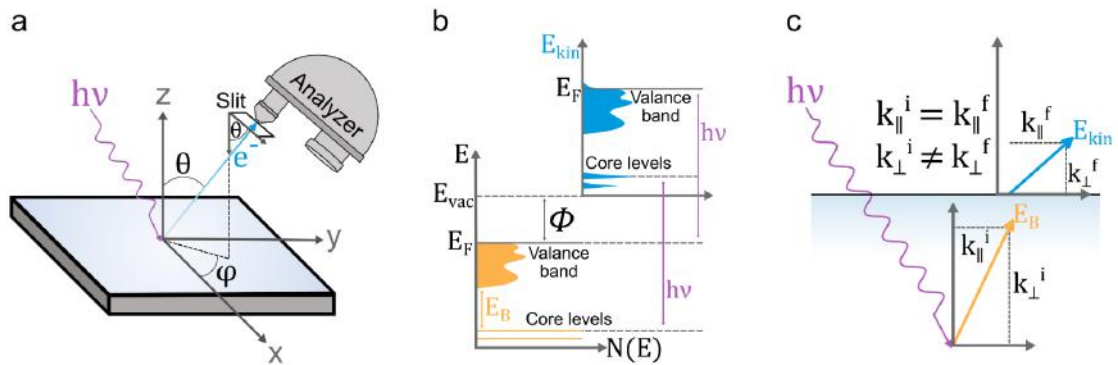
Illustration of key concepts in ARPES. (**a**) depicts the relevant geometries of the incoming photon, solid angles of the ejected photoelectron and analyser. (**b**) shows the conservation of energy in the photoemission process, where $E_{kin} = h\nu - \Phi - E_B$. (**c**) shows the conservation of momentum in the photoemission process, where momentum parallel to the surface is conserved but perpendicular momentum is not. Adapted with permission from Atwa [133].

Angle Resolved Photoemission Spectroscopy (ARPES) derives its core working principle from the photoelectric effect. When a photon of light impinges on a surface, it transfers energy to the electrons in the material and excites them. When the energy

transferred is greater than the work function of the material, these electrons are ejected from the surface of the material and are known as photoelectrons.[134,135]

The energy of the electrons are conserved such that

$$E_{kin} = h\nu - \Phi - E_B \tag{2.11}$$

where Φ is the work function of the material (the minimum energy required to remove an electron from the material) and E_B is the binding energy of the electron. Electron momentum parallel to the surface is also conserved such that

$$\hbar k_{||}^f = \hbar k_{||}^i = \sqrt{2mE_{kin}}(sin\theta\ cos\psi\ \boldsymbol{k}_x\ +\ sin\theta\ cos\psi\ \boldsymbol{k}_y) \tag{2.12}$$

where $\hbar k_{||}^f$ and $\hbar k_{||}^i$ are the parallel momentum components of the final (ejected photoelectron) and initial (bound electron in the material) states respectively.[136] $\hbar$ is the reduced Planck constant, m is the rest mass of an electron and (θ, ψ) are the solid emission angles of the photoelectron. It is noteworthy that momentum perpendicular to the surface is not conserved, however as we are measuring a material that is 2D in nature we can assume that this is unimportant. This limitation can be overcome by estimating the perpendicular momentum using advanced photon sources, however this is outside the scope of this thesis.

Therefore if we use a monochromatic photon source of a known energy and measure the kinetic energy and emission angle of the photoelectrons, we can map the energy **E** vs **k** relation of the electrons within the material. Using this we can directly map the band structure, which has been used extremely effectively to understand materials such as high temperature superconductors, topological insulators, semimetals, 2D materials, heterostructures, and more.[136].

2.4 Tight Binding Band Structure Calculations

The tight binding band structure calculations for CeTe$_3$ (and all RTe$_3$ compounds) are relatively simple, as the Fermi level E_F lies within the Te p orbital manifold. Only the p_x and p_z orbitals are partially filled and contribute to the density of states near the Fermi level. The Te p_y and s orbitals are completely filled and the rare earth d orbitals are completely empty, and are therefore located away from E_F and not considered in the model.[137,138] The dispersions of the p_x and p_z orbitals can be modelled as 1D chains, given by the equations:

$$\begin{aligned} E_{px} = -2t\ cos[k_x + k_z] + 2t'\ cos[k_x - k_z] - E_F \\ E_{pz} = -2t\ cos[k_x - k_z] + 2t'\ cos[k_x + k_z] - E_F \end{aligned} \tag{2.13}$$

where the t is the term for hopping along a chain and t' is the term for hopping perpendicular to the chain.[71,85] The Fermi level E_F is set to $-2\ t\ sin(\frac{\pi}{8})$ on the assumption that Ce is trivalent and donates two electrons in to the Te atoms in the CeTe slab and 0.5 electrons to each of the flanking Te planes. As the p_y is completely filled, this leaves 1.25 electrons in each of the remaining p orbitals.[71] The slope of the bands as they cross E_f is the Fermi velocity, which is primarily determined by t,

and the Fermi surface curvature is determined by t/t'.[87] The resulting Fermi surface consisting of perpendicular distorted chains is shown in figure 2.9a. In this first basic approximation the bands are totally non-interacting, however at band crossings this contradicts the Pauli exclusion principle (as the bands would have the same quantum numbers). We therefore use basic perturbation theory to solve for the interacting band dispersions. The dispersion relations are given by the solutions of the Hamiltonian matrix

$$E(k) = \begin{bmatrix} E_{px} & V \\ V & E_{pz} \end{bmatrix} \qquad (2.14)$$

where E_{px} and E_{px} are the bare dispersions and V is the term defining the strength of the interaction. With V set at zero, the eigenvalues of this matrix are simply the original non-interacting (unperturbed) band dispersions. When V has a finite value, the eigenvalues are the new interacting band dispersions. This interaction results in a gap opening due to the disallowed crossing, with an hole-like inner square pocket centred at Γ and an electron-like outer pocket centred at the K point of the 2D BZ (shown in figure 2.9b).

Now we must account for the additional periodicity of the lattice caused by the superlattice(s) that are formed. In a periodic system, if a distortion or modification that creates a superlattice occurs in real space there will be a corresponding shrinkage of the Brillouin zone and change in symmetry in reciprocal space.[139,140] The new band dispersions within the first BZ can be determined by using the fact that when the new symmetry of the lattice causes the first, second and higher order BZs to be inequivalent, the bands are backfolded into the new BZ. Translation of the bands by the lattice vector of the superstructure is symmetrically equivalent. Therefore to account for the periodicity of the CDW, we must translate the bands by the CDW nesting vector $\mathbf{q}_{CDW}$ to determine the positions of the shadow bands within the first BZ, as illustrated in 2.9c. These CDW shadow bands have a high degree of overlap with the original bands within the indicated grey region, which due to avoided crossings opens the CDW energy gap in this region of $\mathbf{k}$-space.

An extra complication arises from the fact that the Te sheets have a different symmetry to the overall lattice due to the inequivalence between the two Te sheets making up the Te bilayer. This means the 3D crystal structure has a different Brillouin zone to the 2D sheet. To obtain a more realistic Fermi surface, we must take the bands calculated for the 2D FS and fold them (or equivalently, translate them by 1 3D BZ) to obtain a new FS that contains both the original and the folded bands. This is the same effect as caused by the CDW, however the CDW causes translation in the k_x direction by a vector incommensurate with the lattice, whereas the 2D to 3D BZ folding causes a translation in both k_x and k_y by a vector commensurate with the lattice. The Fermi surface obtained after taking into account this 2D→3D BZ folding is illustrated in fig. 2.9d.

For clarity, from this point onwards we will refer to the non-translated p_x and p_y derived bands (as shown in 2.9b) as "original bands". We will refer to the translated bands caused by the CDW (green in 2.9c) as "CDW shadow bands". We will refer to the translated bands caused by the inequivalence of the 2D Te net BZ and the

Figure 2.9: Cartoon Fermi Surface

CDW shadow   BZ band folding
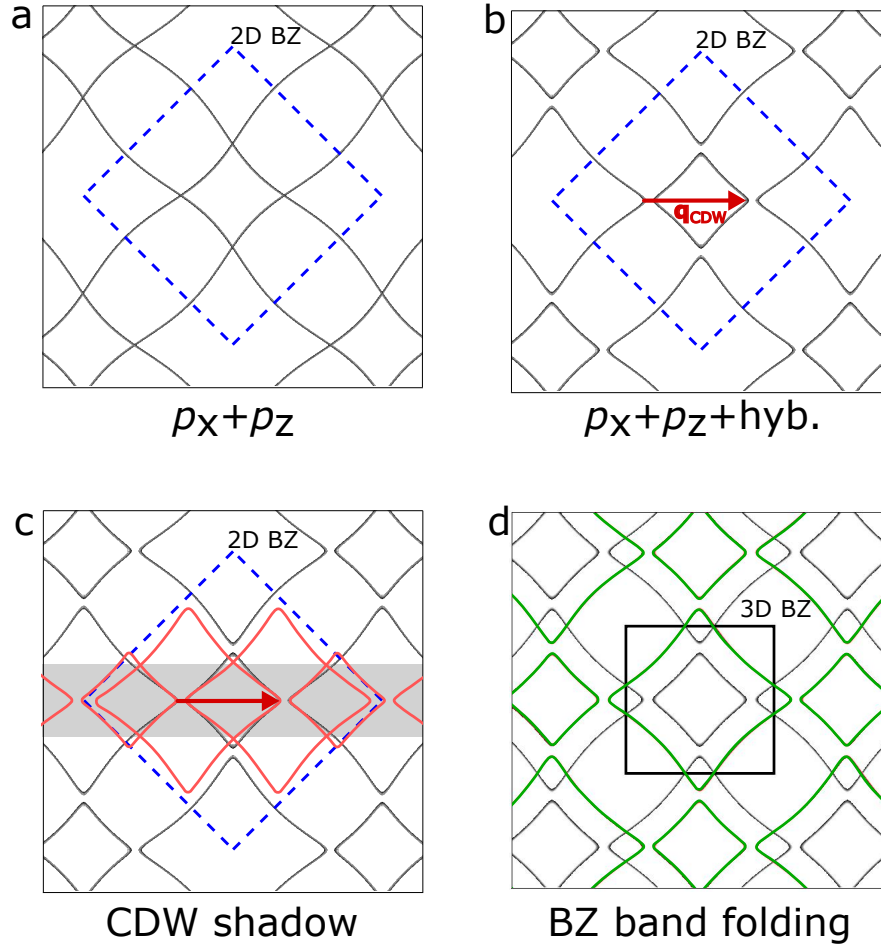
Cartoon illustrating the Fermi surface derived from the simple tight binding model. Blue dotted square indicates the 2D Brillouin zone, black square indicates the 3D Brillouin zone. (**a**) shows the original non-interacting p_x and p_z bands. (**b**) The same bands after an interaction term is included, causing a forbidden crossing and a gap to open. The primary CDW nesting vector $\mathbf{q}_{CDW}$ is indicated with the green arrow. (**c**) Original bands shown in black and the CDW shadow bands are shown in green. Grey region indicates the regions where overlap of the original and shadow bands is high, meaning the avoided crossings will open the CDW gap in this region. Only the CDW FS pockets/bands with their centres at $k_y = 0$ are shown for clarity. (**d**) Fermi with the effects of 2D to 3D band folding, with the original bands in black and the folded bands in red.

underlying 3D structures BZ (red in 2.9d) as "BZ folded bands". When referring to both sets of translated bands we will use the terms "shadow bands" and "replica bands" interchangeably.

This Fermi surface gives a good approximation as to the shape, size and location of the Fermi surface features in CeTe$_3$ (and other RTe$_3$ members). It is however missing the important effect of interactions between the replica bands and the original bands, which cause the Fermi surface reconstructions such as energy gaps and hybrid pock-

ets observed experimentally.[13,14,71,81,83,86] Treating these bands as non-interacting is clearly not an appropriate approximation for this system due to the substantial momentum dependant gaps caused by the broken translational symmetry.

We rectify this shortcoming by introducing a larger interacting model. Using the same pertubative approach as above, we construct a 12×12 Hamiltonian matrix for the system, given below. The non-interacting initial 12 bands consist of the 2 original p_x and p_z bands (given by E_{px} and E_{pz}, equation 2.13) and their BZ folded replicas ($E_{px\ 3D}$ and $E_{pz\ 3D}$). The remaining 8 bands consist of the previous 4 bands translated either forward or backward by $\mathbf{q}_{CDW}$. Only the first order interactions caused by a single $\mathbf{q}_{CDW}$ translation are accounted for, as it is assumed that while higher order interactions will exist due to the incommensurate nature of the CDW, they will be weak enough to be negligible.[141] The interaction term V_P accounts for the interaction strength among the original and the BZ folded bands, V_{CDW} accounts for the interaction strength of the CDW shadow bands. Our results are comparable to those for a similar model presented by Moore et al. [87], however details on the parameters and implementation of their model are sparse and so it cannot be determined how our models differ in detail and execution. A similar model is also presented by Chikina et al. [81], with a few key differences. Their model takes into account bilayer splitting, whereas ours does not. Our model takes into account BZ folded bands that are also translated by $\mathbf{q}_{CDW}$, which theirs does not. They use their model to fit ARPES data of NdTe$_3$, and successfully reproduce the hybridisation of the bands that leads the the observed pockets.

We adjusted the parameters of our model by first defining a reasonable guess for the initial values based on literature and rough estimations, and then adjusting the parameters until our calculated Fermi surface was a very close match to the SX-ARPES measured FS. The results of this fitting are provided and discussed in chapter 3, section 3.3.

$$\begin{bmatrix}
E_{px} & V_P & V_P & V_P & V_{CDW} & V_{CDW} & V_{CDW} & V_{CDW} & V_{CDW} & V_{CDW} & V_{CDW} & V_{CDW} \\
V_P & E_{pz} & V_P & V_P & V_{CDW} & V_{CDW} & V_{CDW} & V_{CDW} & V_{CDW} & V_{CDW} & V_{CDW} & V_{CDW} \\
V_P & V_P & E_{px\ 3D} & V_P & V_{CDW} & V_{CDW} & V_{CDW} & V_{CDW} & V_{CDW} & V_{CDW} & V_{CDW} & V_{CDW} \\
V_P & V_P & V_P & E_{pz\ 3D} & V_{CDW} & V_{CDW} & V_{CDW} & V_{CDW} & V_{CDW} & V_{CDW} & V_{CDW} & V_{CDW} \\
V_{CDW} & V_{CDW} & V_{CDW} & V_{CDW} & E_{px+\mathbf{q}} & 0 & 0 & 0 & 0 & 0 & 0 & 0 \\
V_{CDW} & V_{CDW} & V_{CDW} & V_{CDW} & 0 & E_{pz+\mathbf{q}} & 0 & 0 & 0 & 0 & 0 & 0 \\
V_{CDW} & V_{CDW} & V_{CDW} & V_{CDW} & 0 & 0 & E_{px\text{-}\mathbf{q}} & 0 & 0 & 0 & 0 & 0 \\
V_{CDW} & V_{CDW} & V_{CDW} & V_{CDW} & 0 & 0 & 0 & E_{pz\text{-}\mathbf{q}} & 0 & 0 & 0 & 0 \\
V_{CDW} & V_{CDW} & V_{CDW} & V_{CDW} & 0 & 0 & 0 & 0 & E_{px\ 3D+\mathbf{q}} & 0 & 0 & 0 \\
V_{CDW} & V_{CDW} & V_{CDW} & V_{CDW} & 0 & 0 & 0 & 0 & 0 & E_{pz\ 3D+\mathbf{q}} & 0 & 0 \\
V_{CDW} & V_{CDW} & V_{CDW} & V_{CDW} & 0 & 0 & 0 & 0 & 0 & 0 & E_{px\ 3D\text{-}\mathbf{q}} & 0 \\
V_{CDW} & V_{CDW} & V_{CDW} & V_{CDW} & 0 & 0 & 0 & 0 & 0 & 0 & 0 & E_{pz\ 3D\text{-}\mathbf{q}}
\end{bmatrix}$$

Eq. (2.15) - Hamiltonian matrix used for the calculation of the interacting tight binding model

Chapter 3

Synthesis, ARPES and Tight Binding fit for CeTe$_3$

3.1 Sample Growth and Characterisation

For the growth of CeTe$_3$ single crystal samples, we used the self-flux method reported by Ru and Fisher [64]. Details of the self-flux method are described in the methods section. We optimised the parameters, finding that using a flux ratio of 1 : 30 Ce:Te gave the highest quality large crystals. We used the temperature profile given in fig. 3.1, with a 24 hour soak at 900 °C before a 7 day slow cooling to 500 °C, before centrifuging the tubes as soon after furnace removal as possible to avoid early solidification of the Te flux. Results given in this thesis were performed on crystals that were cleaned of residual flux using a scalpel.

Figure 3.1: Self-flux Growth Temperature Profile
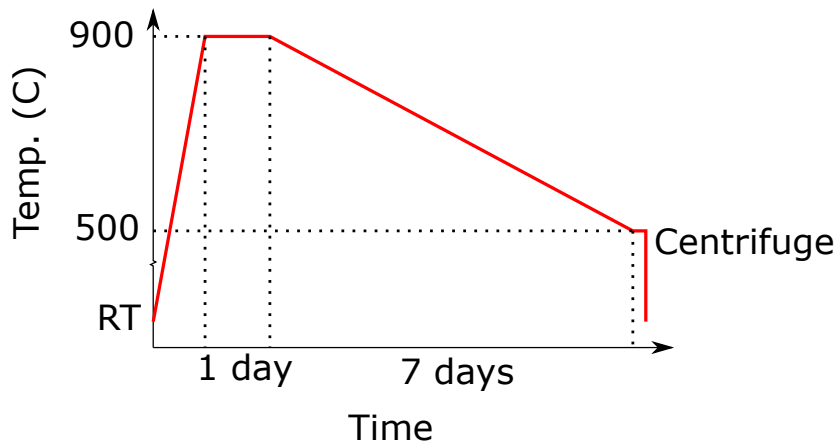
Temperature profile used for the self-flux binary melt growth of CeTe$_3$.

Whilst excess flux can be removed manually, the crystals are fragile and can easily be damaged by manual handling. In order to minimising handling, we trialled using a post-growth annealing step that consisted of gently packing the grown crystals in quartz wool, sealing them in an evacuated quartz tube and annealing in a furnace

at 500 °C for a few hours before letting the furnace cool passively. This successfully removed excess flux without causing damage to the crystals. Interestingly, we found that also resulted in a dramatic reduction in defects within the crystal as measured by STM topography. While usually we found a defect density of approximately 5-6 intrinsic defects per 100 nm with non-annealed crystals, we found this number was an order of magnitude lower in annealed samples. In fact, the defect density was so low in the annealed crystals that we were unable to perform QPI measurements due to the lack of scattering centres, meaning we reverted to using manually cleaned crystals for SI-STM experiments. This step may be useful to incorporate for future experiments where an extremely high crystal quality is desired such as transport, magnetisation or diffraction.

To determine the absence of coexisting phases we performed *(0k0)* X-ray diffraction scans using a Bruker D8 discover with using a 0.2 mm nickel foil $k\beta$ filter and a collimator. To mount the samples for XRD analysis, we either mount them on a glass slide using low adhesion double sided tape, or mount them on the sample plates used for STM before performing the scans. A typical scan is shown in figure 3.2, showing the appearance of the expected peaks from CeTe$_3$. There is also a very small unknown peak occurring at $2\theta \approx 44°$, which does not originate from CeTe, CeTe$_2$ or Te impurity phases. We suspect it may be the signature of the (111) plane of austentitic stainless steel which is found somewhere in the beamline of the diffractometer.

Figure 3.2: *(0k0)* X-Ray Diffraction Scan of CeTe$_3$
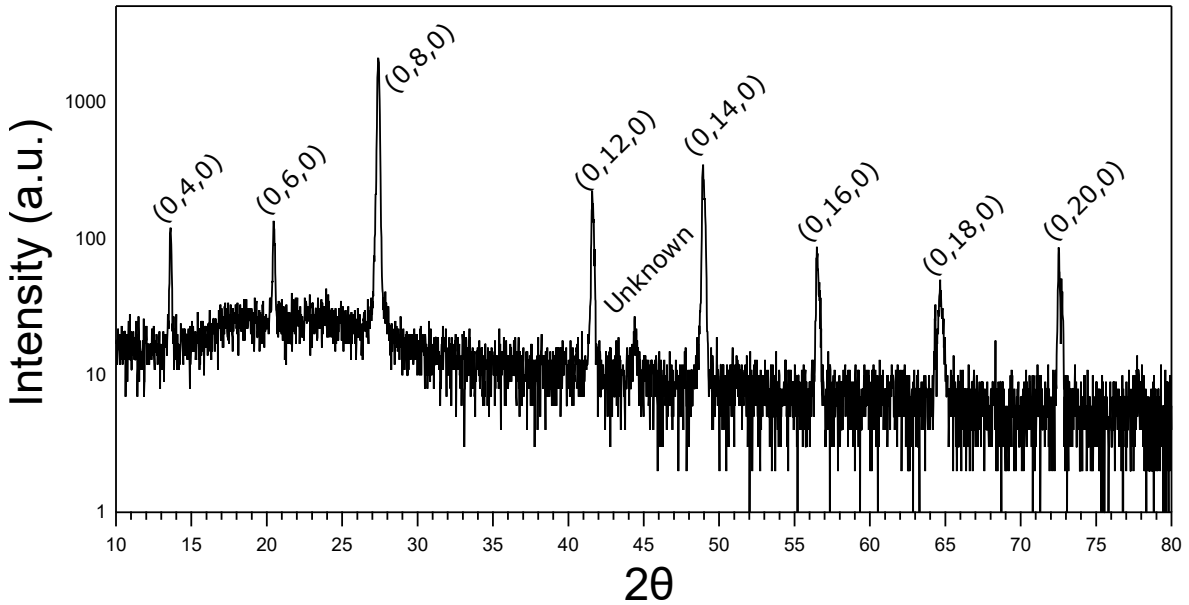
(0k0) X-ray diffraction scan of CeTe$_3$ with assigned peaks.

We also performed SC-XRD on a representative sample using a Bruker D8 Venture and obtained the lattice parameters given in table 3.1, which correspond with values given in literature for CeTe$_3$.[142,143]

From these X-ray diffraction results we can confidently say that we have successfully obtained high quality single crystals of CeTe$_3$. Our next characterisation step

Table 3.1: CeTe$_3$ Lattice Parameters from SC-XRD

a	b	c	α	β	γ
4.37390 Å	26.00400 Å	4.38670 Å	90°	90°	90°

Table of lattice parameters obtained from SC-XRD

was to measure magnetisation and heat capacity for our samples to correlate them with literature results. DC Magnetisation results were carried out using a Magnetic Properties Measurement System (Quantum Design) with a ^{3}He insert[144] and heat capacity measurements were carried out using a Physical Properties Measurement System (Quantum Design). The resulting curves are shown in figure 3.3

Figure 3.3: Magnetisation vs Temperature curves for CeTe$_3$
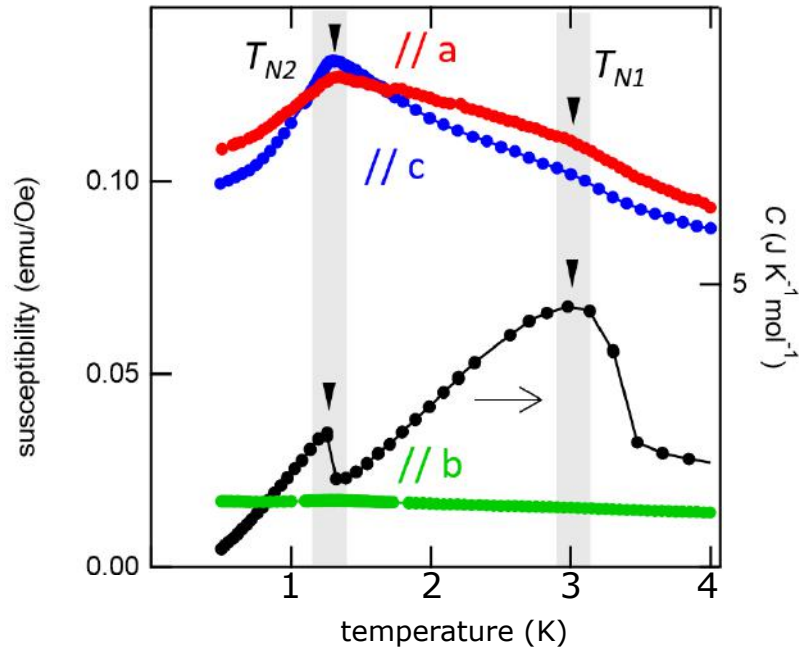
Temperature dependence of the magnetic susceptibility (left axis) and heat capacity (right axis) for CeTe$_3$. The three magnetisation curves are labelled with their corresponding crystal axis (note that b-axis is out-of-plane in this system). These results were published in Okuma et al. [8]

From these M-T and heat capacity curves we can see that there are two Neel transition temperatures, assigned as T_{N1} and T_{N2}. This compares very well to the work of Deguchi et al. [78], who showed that above T_{N1} (at 3.1 K), the material is paramagnetic. In between T_{N1} and T_{N2} (1.3 K to 3.1 K) an intermediate state forms, and below T_{N2} the material is a long range antiferromagnet.

3.2   ARPES Measurements

In this section we discuss the ARPES results which we used to refine our tight binding model parameters. The experiment was performed at the beamline BL25SU at the SPring-8 facility.[145] For the results presented in this thesis, the total experimental energy resolution was approximately 60 meV for a photon energy ($h\nu$) of 600 eV. All samples were cleaved at a pressure of 5×10^8 Pa at approximately 20 K, exposing shiny surfaces. The sample temperature was kept at 16 K during the measurement.

Figure 3.4 is a map of the measured spectral weight near the Fermi level of CeTe$_3$ integrated over a range of 80 meV. The main features in this map show the difference in the FS of the 1st and 2nd BZ, with a small inner square centred at (0,0) in the BZ coordinates and a larger outer square centred at (2,0) and (0,2). These main inner and outer pockets are exactly as expected from the simple tight binding structure, as depicted in fig. 2.9b. Additional to these main pockets, we also observe the weaker intensity replica bands, especially evident outside the 1st BZ where they are not over-shadowed by the much stronger intensity of the original non-replica bands. The reason that these replica bands are less intense is due to the fact that the intensity of a folded FS in ARPES is proportional to the strength of the coupling that is responsible for the folding, and in the case of CeTe$_3$ this is the weak coupling between the Te layer and the CeTe slab.[85,141] This map also shows clearly the twofold symmetry that is common to all RTe$_3$ compounds in the CDW1 state, with the CDW gap opening along the k_x direction. These results agree very closely with previous ARPES studies on RTe$_3$ compounds.[9,71,81,84–88]

Figure 3.4: ARPES Fermi Surface
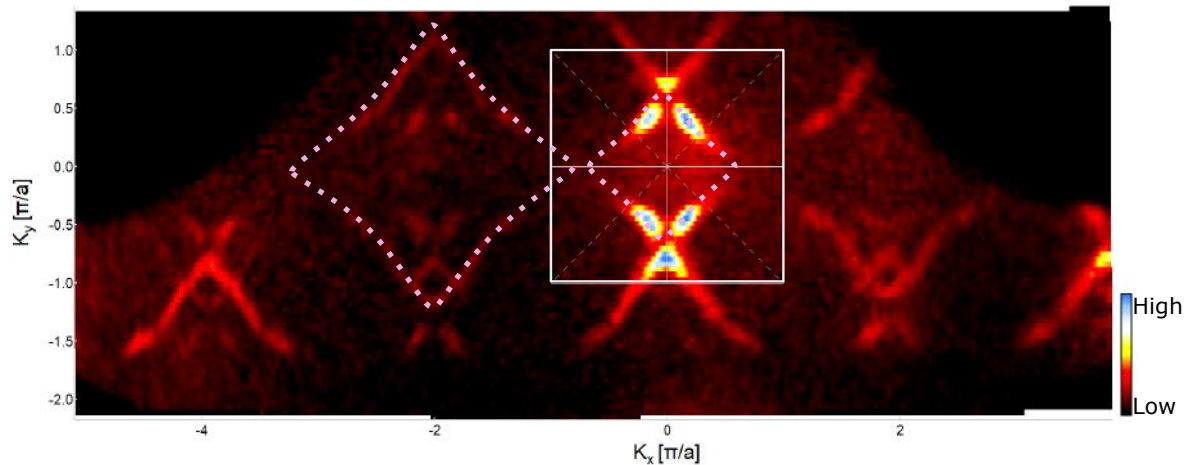
Fermi Surface of CeTe$_3$ as measured by ARPES. Measurement was carried out at 16 K with a photon energy of 600 eV. White box indicates the 1BZ, dotted markers indicate the inner and outer square pockets as predicted from the TB model, as in figure 2.9b.

A dispersion linecut is shown in figure 3.5b, taken along the red line indicated in 3.5a. The most intense signals are the main p_x and p_z derived bands, marked in blue. These bands hybridise to form the hole-like pockets that are observed in the Fermi

surface. We show the partially gapped nature of the Fermi surface in figure 3.5 c, d and e, which show the contours of constant energy of the main hole-like pocket inside the CDW gap (c,d) and outside the gap (e). The momentum position of the gap occurs along the k_x direction (coincident with the CDW nesting vector $\mathbf{q}_{CDW}$) and causes the the square pocket to split into upper and lower chevrons. This changes the symmetry of the Fermi surface from fourfold symmetry outside the CDW energy gap to twofold symmetry inside the gap.

Figure 3.5: Band Dispersions from ARPES
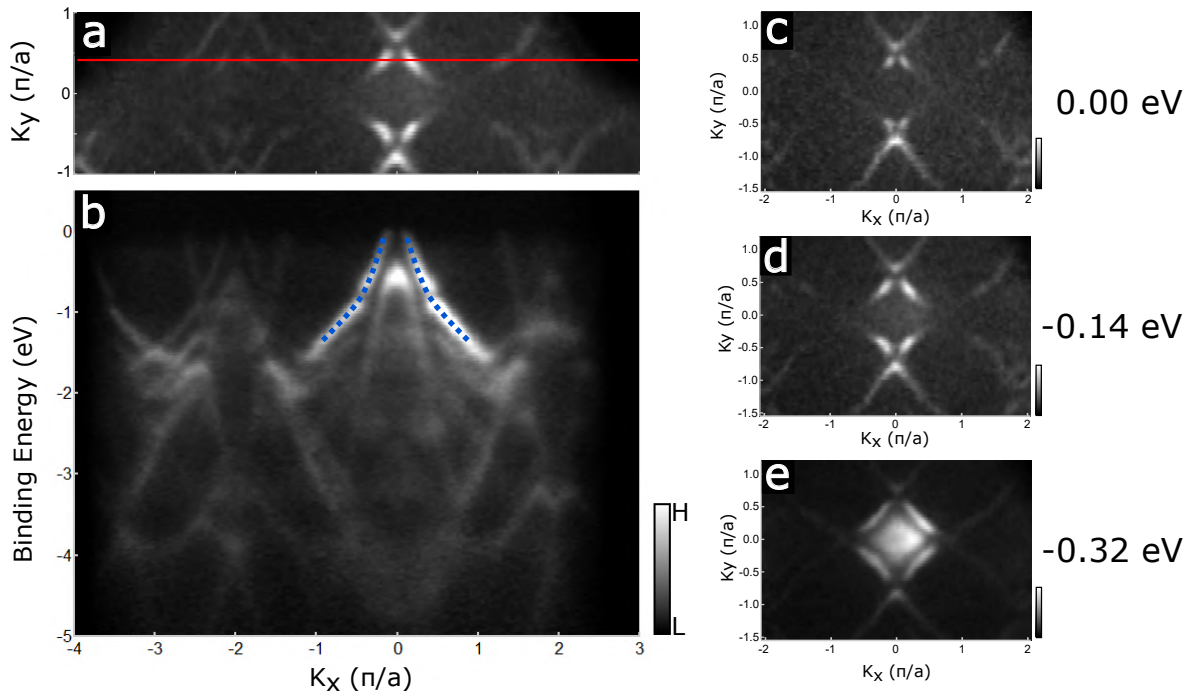
Experimental band dispersion of CeTe$_3$. (**a**) is the Fermi surface as shown in fig. 3.4, with a red line indicating the cut taken to show the band dispersion in (**b**). Dotted blue lines are a guide to the eye indicating the main p_x and p_z derived bands. (**c,d,e**) are contours of constant energy of the inner pocket centred around Γ of the 1st BZ ((0,0) in BZ coordinates) at E_F, at -0.14 eV (inside CDW gap) and at -0.32 eV (outside CDW gap), showing the evolution of the gap in the k_x direction.

3.3   Tight Binding Fit

We use this measured ARPES Fermi surface to empirically fit the parameters of our tight binding model. By adjusting the parameters t (hopping along a chain), t' (hopping perpendicular to the chain), V_p (hybridisation between the p orbitals, including those folded from the 2D BZ) and V_{CDW} (hybridisation between the CDW shadow bands and the other bands) we can achieve a close match between the theoretical and measured Fermi surface. The parameters used are given in table 3.2 (n.b. the atomic Te spacing is not necessarily indicative of the actual Te spacing, and was adjusted to account for a slight distortion of the collected ARPES data)

Table 3.2: Table of Tight Binding Model Parameters

Parameter	Value
a (Te lattice parameter, Å)	3.19
t	-1.9
t'	0.35
V_p	0.47
V_{CDW}	0.39
CDW periodicity (units of a)	2.1

Empirically derived parameters used for the tight binding model simulation.

In figure 3.6a we present the original 12 bands as described earlier. These consist of the 2 original p_x and p_z bands (in dark and light blue respectively) and their BZ folded replicas (in green). The four red bands are the p_x and p_z bands translated forwards or backwards in k_x by $\mathbf{q}_{\mathrm{CDW}}$, and the four grey bands BZ folded replicas translated forwards or backwards in k_x by $\mathbf{q}_{\mathrm{CDW}}$. All bands are therefore defined by the same relationship with energy, with only their momentum relation being different between the bands.

In figure 3.6b we show the Fermi surface after introducing the interaction terms between the bands. Hybridisation of the bands occurs, resulting in gaps appearing and the formation of new pockets on the FS. It can be seen that different regions of the pockets can be directly traced to the initial non-interacting band that they derive from, which becomes important later for scattering analysis. Also evident is the prominent CDW gap in the k_x direction, as is expected due to our inclusion of the $\mathbf{q}_{\mathrm{CDW}}$ periodicity in the interacting Hamiltonian.

As discussed above, the bands with the most obvious spectral weight in ARPES are the original, non-folded p_x and p_z bands. In 3.6c we overlay the TB calculated p_x and p_z bands onto the SX-ARPES FS and see an excellent agreement between our simulation and experiment. Our model is also fully consistent with literature ARPES and simulation results.[71,84,85,87]

Figure 3.6: TB model Fermi Surface and Comparison to ARPES FS
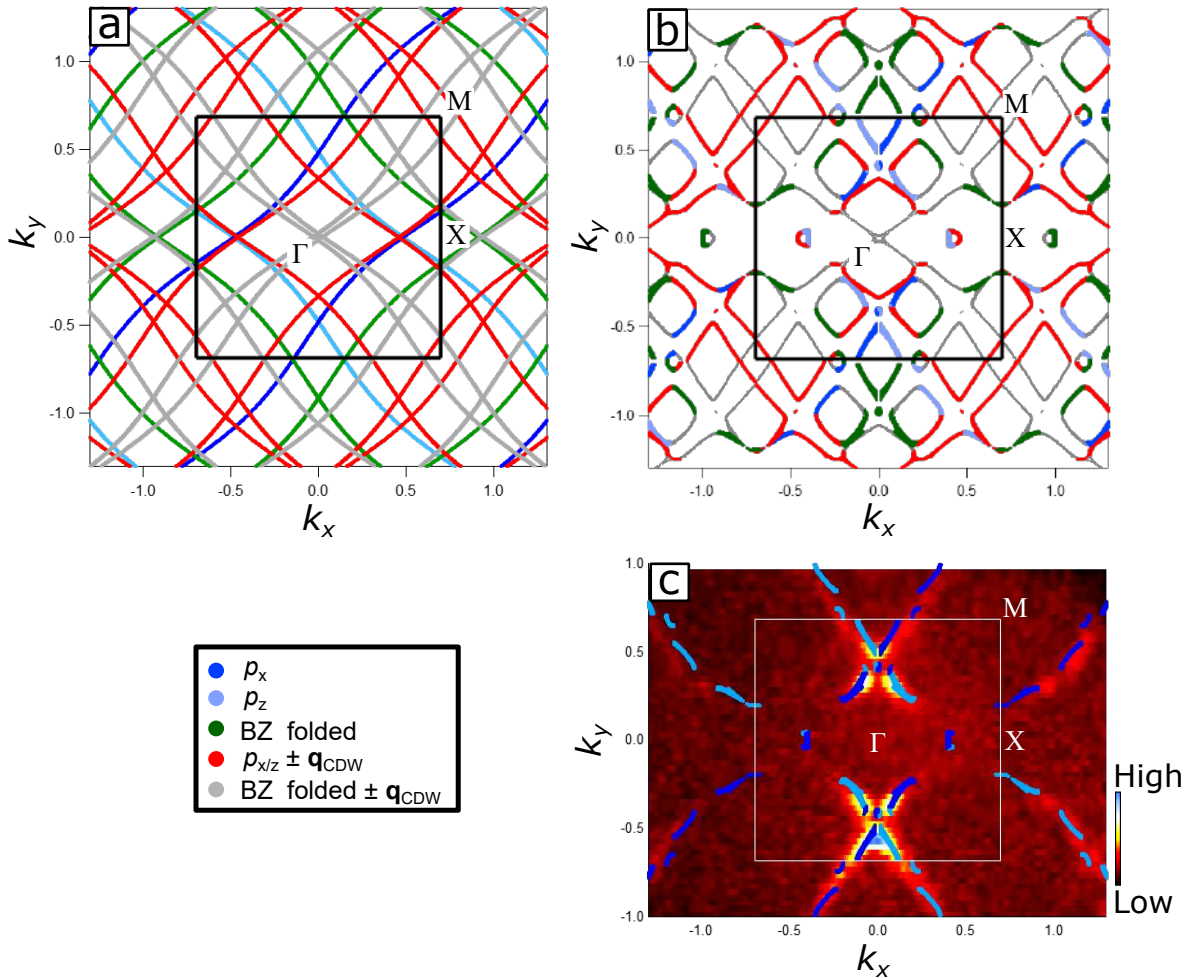
(a) Fermi surface of the 12 non-interacting bands taken as the starting point of the TB model. Colours indicate the origin of the bands, described in the legend. (b) Interacting tight binding model Fermi Surface. Colours indicate which region of the new pockets originates from which initial bands, corresponding with (a). (c) p_x and p_z derived interacting bands overlaid on the SX-ARPES FS (fig 3.4). Black/white inner boxes indicate the 1st BZ.

Chapter 4

Scanning Tunnelling Microscopy and Quasiparticle Interference of CeTe$_3$

4.1 Topography and Charge Density Wave Measurements

4.1.1 Topography

Figure 4.1 shows the topographic surface of the CeTe$_3$ crystal as measured by STM at 4.2 K. This top surface consists of the Te square net with the CeTe slab being below the surface, as expected from the crystal structure's facile cleave plane between the Te bilayer. This cleavage is highly repeatable; in dozens of measurements, we never observed a different surface termination. Clearly observable in the topography is the square net with unidirectional charge density wave modulations in the vertical axis. Also visible are the scattering centres which are required for QPI measurement, appearing as X-shaped modulations in the topographic height.

4.1.2 Fourier Analysis of Topography

In order to carefully analyse the periodicity of the sample surface, we take the Fast Fourier Transform (FFT) of the topograph, shown in figure 4.2a. The Bragg peaks originating from the Te square net are demarcated by a red square; the lattice constant of said net as calculated from these Bragg peaks is 3.1 Å, in agreement with literature and our XRD results. The alternate Bragg peaks that are a result of the subsurface Ce structure causing modulations of the Te net are demarcated in blue. From here onwards it will be convenient to consider the results in the reference frame of this larger real space (smaller reciprocal space) 3D net in the same manner as the earlier chapters; unless otherwise specified, BZ will refer to the 3D Brillouin zone. We label the vectors at the Bragg peaks as $\mathbf{a}^*$ and $\mathbf{c}^*$.

In addition to the Bragg peaks, we also observe multiple peaks related to the CDW. A linecut of these peaks along the Γ-X direction of these peaks is shown in fig. 4.2. The folded band structure means that there are two equivalent CDW nesting vectors at $2/7\mathbf{c}^*$ and $5/7\mathbf{c}^*$, labelled as $\mathbf{q'}_{CDW}$ and $\mathbf{q}_{CDW}$ respectively. We also observe additional

Figure 4.1: Topography of the CeTe₃ Surface
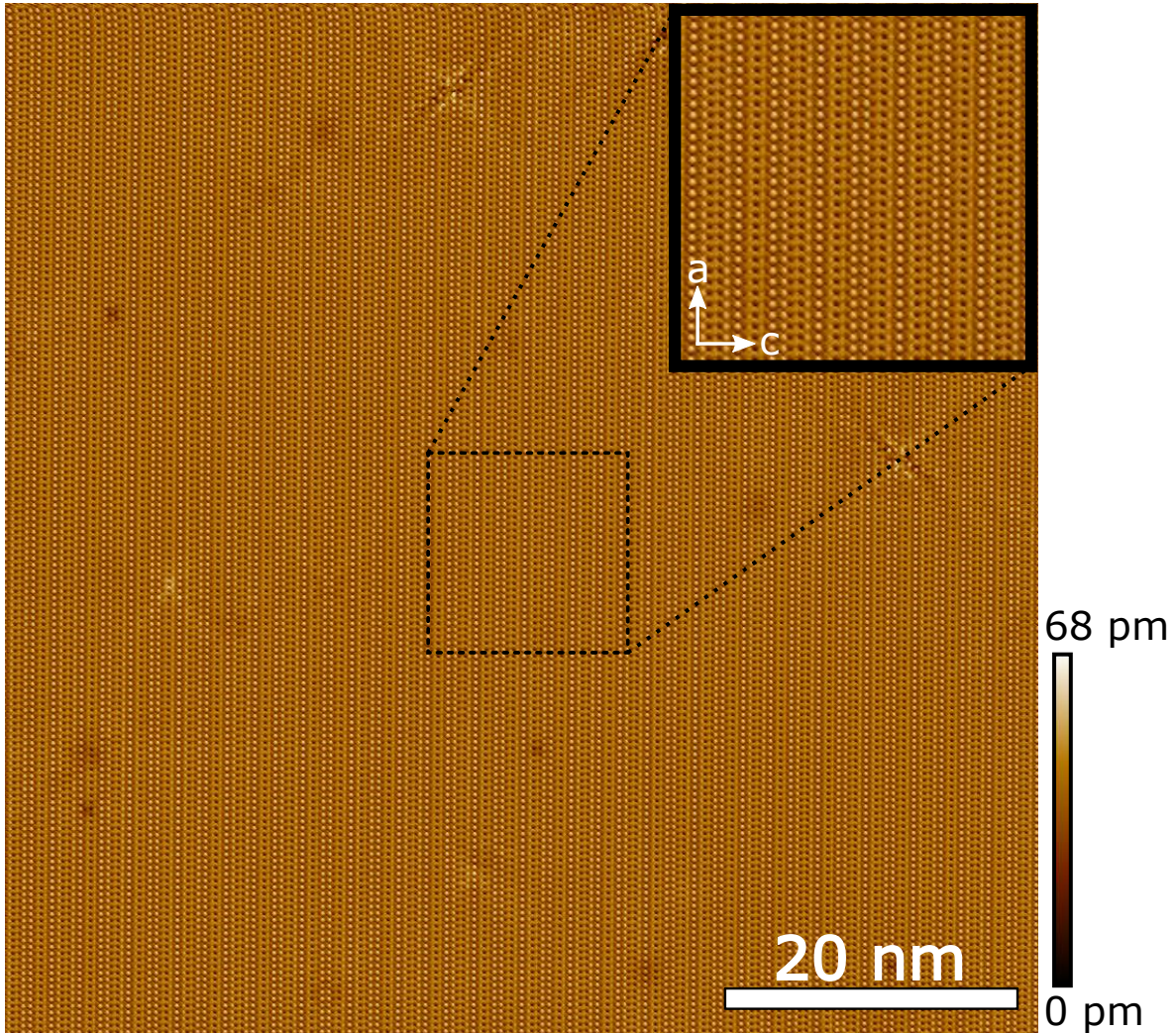
Topography of the CeTe₃ surface. Inset is a closeup of the region indicated. $V_b = -60$ mV, $I_{set} = 500$ pA, $T = 4.2$ K

peaks which are linear combinations of $\mathbf{q}\text{'}_{CDW}$ and $\mathbf{c}^*$ which occur due to wavevector mixing. A simple assumption is that when we observe the convolution of two sine waves (CDW and atomic in our case) with STM, the signal will be proportional to the sum of the two waves. If however there is an asymmetry in the way the CDW couples to the peaks and troughs of the atomic corrugation, we instead see that the signal has a component proportional to the product of the waves. As succinctly stated by Tomic et al. [92], "the signal will exhibit a contribution similar to the product of the two waves if the CDW signal is stronger at the atomic lattice sites and weaker at the locations between atoms, or vice versa". As the product of two sine waves can be expressed by a sum and a difference

$$sin(\mathbf{q}\text{'}_{CDW})sin(\mathbf{c}^*) = \frac{1}{2}cos(\mathbf{q}\text{'}_{CDW} - \mathbf{c}^*) - \frac{1}{2}cos(\mathbf{q}\text{'}_{CDW} + \mathbf{c}^*) \qquad (4.1)$$

Figure 4.2: Fourier Transform Analysis of CeTe$_3$ Topography Data
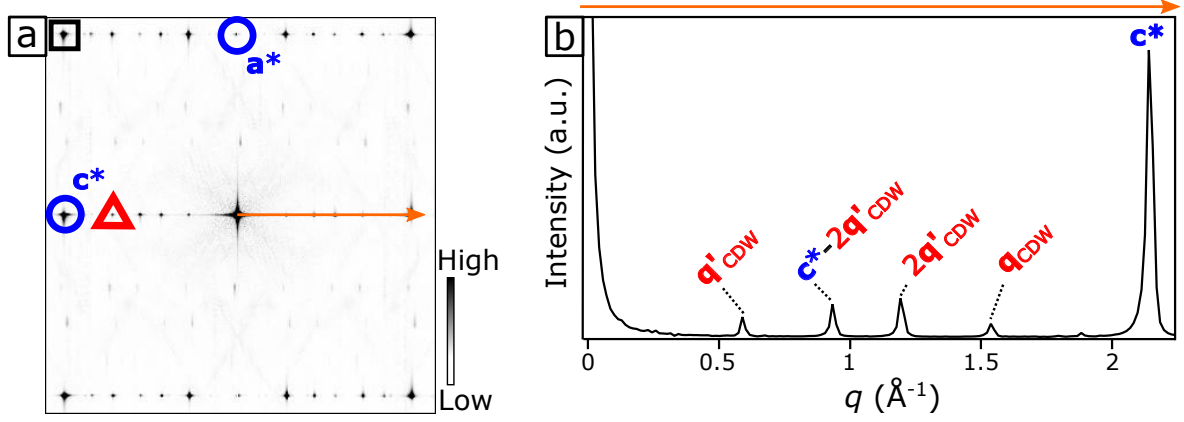
(**a**) 2D Fast Fourier Transform of the topography shown in fig.4.1. (**b**) Linecut of the topo taken along the Γ-X direction, as indicated by the orange arrow in 4.2a.

we can expect to see peaks at $\mathbf{q'}_{CDW} + \mathbf{c}^*$ and $\mathbf{q'}_{CDW} - \mathbf{c}^*$. As indicated by the label markers in fig. 4.2b, we do indeed see these peaks, in addition to higher order harmonics. Tomic et al. [92] propose that the peak/trough asymmetry that causes this effect results from the fact that the CDW modulates the amplitude of the surface Te electron density, and these Te atoms lie at the troughs of the subsurface lattice. The weak effect of the CDW upon the subsurface lattice results in the asymmetry and hence the wavevector mixing.

We also note that we see a replica of the CDW peaks along the top and bottom of the FFT image, connecting the Te Bragg peaks along the edge of the third 3D Brillouin zone. These peaks arise from a combination of carrier density modulation and structural modulation of the Te net, further breaking the translational symmetry and causing these additional peaks to appear. The intensity of the peaks is given by a combination of the strength of the tunnelling signal from the modulation component with the corresponding periodicity (in the case of carrier density modulation) and the magnitude of the atom displacements (in the case of the structural modulation).[93]

4.1.3 dI/dV Spectroscopy

We now move on to discuss our dI/dV spectroscopy of the surface of CeTe$_3$. Figure 4.3 shows the obtained spectrum when averaged from $186,624$ individual spectra taken over an area of 90 by 90 nm.

As discussed in the introduction chapter, the formation of a CDW state results in an energy gap opening in the nested regions of the Fermi surface, leading to a gap in the measured LDOS (dI/dV). In CeTe$_3$, Ralević et al. [93] showed the presence of the expected energy gap in the dI/dV spectrum at room temperature. Our results are broadly similar, showing the appearance of a gap within which is remaining DOS due to a partially gapped FS. The inherent asymmetry of the dI/dV curve arises from the fact that with STM we can probe the DOS at energies other than E_F, meaning

we are not only probing the p_x and p_z orbitals but also the p_y orbital.[91] Due to the p_y orbital being completely filled, it is more energetically favourable to remove electrons from it at negative bias voltages compared to adding electrons at positive bias voltages. This results in energies below E_F having a higher DOS, and therefore an asymmetric dI/dV curve.[93] This type of asymmetry observed for other RTe$_3$ compounds; it is also frequently seen in other CDW systems such as transition metal dichalcogenides.[36,91–93,146,147]

Figure 4.3: Wide Energy Range dI/dV Spectroscopy of the CeTe$_3$ Surface
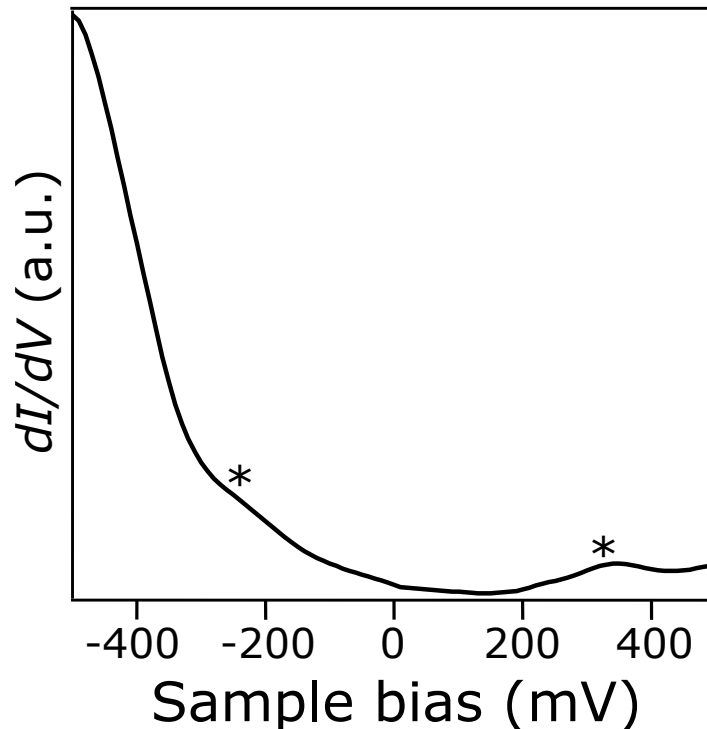
dI/dV spectroscopy of CeTe$_3$ in the range $\pm$ 500 mV. Asterisks mark peak positions. V_{mod} 20 mV, 961 Hz

Figure 4.3 shows two weak peak features marked with asterisks at -230 meV and 330 meV. Whilst our first instinct would be to assign these peaks as the edges of the CDW gap, they give a CDW gap value of $\Delta_{\mathrm{CDW}}^{\mathrm{STM}} = 300$ meV, which is smaller than the ≈ 400 meV gap measured by other STM and ARPES studies.[85,93] Additionally, the density of states between these peaks is not significantly depressed. Ralević et al. [93] propose that the true CDW gap edges exist at -340 meV and 405 meV, however we do not observe any peaks at these values. It is possible that the features we observe are due to gap formation involving the shadow bands, however it is not possible to confirm this with our experimental data. As discussed by Spera et al. [148], the conclusive determination of CDW gaps via STS is problematic due to a lack of momentum resolution and the difficulty of disentangling DOS features arising from the CDW gap and from other origins. Regardless of the exact position of the gap edges, it can be seen from our spectroscopy that there is a v-shaped finite DOS within the gap, as is expected from the partially gapped band structure present in CeTe$_3$.

Figure 4.4: dI/dV Spectroscopy of the CeTe$_3$ Surface near E_F
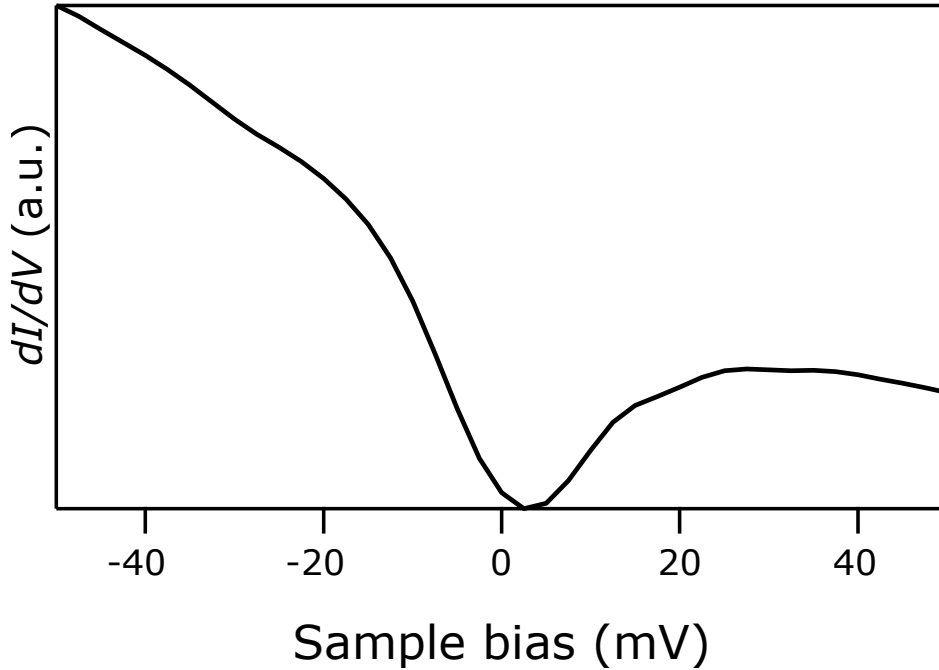
dI/dV spectroscopy of CeTe$_3$ in the range $\pm$ 50 mV. V_{mod} 5 mV, 961 Hz

In figure 4.4 we show the area averaged dI/dV spectra collected in the range $\pm$ 50 mV. We observe the appearance of an obvious gap feature in the range $\approx$ $\pm$15 mV. This could be caused by a coupling to the 3 THz (12 meV) out-of-plane A1g phonon mode, or it could arise from a more exotic interaction involving the axial Higgs mode, which would be expected to occur in the same energy range.[16,149]

4.2 Quasiparticle Interference Measurements

4.2.1 Experimental Results

Observation of QPI

We now discuss our observation of the QPI pattern near E_F in the range $\pm$40 meV. The dI/dV maps at $V_b = -40$, 0, and $+40$ meV are shown in figure 4.5a, c, and e, where $V_b = 0$ corresponds to E_F. These maps are taken from a 70×70 nm area of the same surface shown in figure 4.1. The wave-like conductance corrugations indicative of QPI are clearly observed in the real-space images. To extract the characteristic wave vectors, the FFT images of the conductance maps are shown in 4.5b, d, and f. Visible in these Fourier transform images are the same Bragg peaks and CDW peaks observed for the topographic image, and additionally we see streak-like patterns arising from quasiparticle interference. These streak patterns are present in all three energies -40, 0, and $+40$ meV. These FFT maps are symmetrised around $k_y = 0$ and $k_x = 0$ to increase S/N ratio; a comparison between the symmetrised and the raw data to verify

the the validity of the symmetrisation is given in appendix 5.2.

The characteristics of the QPI signal are essentially similar between the three energies, which is expected given the narrow energy range of the spectroscopic imaging. We also note the appearance of non-dispersive artefact peaks along the line $k_y = \pm 0.2$ Å^{-1}, indicated with green arrows in 4.5d. These peaks arise from long-cycle periodic noise that occurred during the measurement, visible as horizontal streaks in the real-space images. These peaks are notably absent in other partial QPI datasets taken under similar conditions (shown in appendix 5.2), proving their origin as periodic noise.

Figure 4.5: Quasiparticle Interference Maps of CeTe₃ at Different Energies
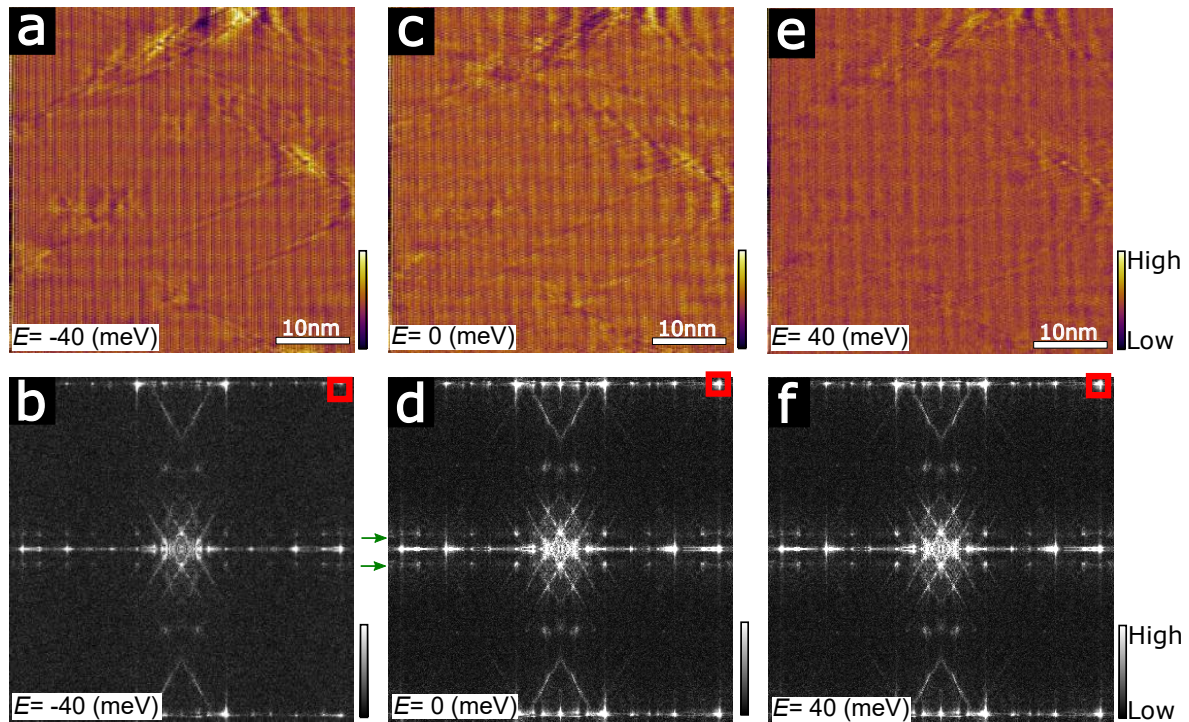
dI/dV maps with their Fourier transforms at -40 meV (**a**,**b**), 0 meV (**c**,**d**), and 40 meV (**e**,**f**), showing the wave-like corrugations caused by quasiparticle interference. Red square in (b,d,f) indicates the Bragg peak of the Te square net. Maps taken on a 70 nm by 70 nm area of the topo shown in fig. 4.1 with V_{mod} 5 meV, 961 Hz, setpoint -15 meV/500 pA

In figure 4.6a we show an enlarged image of the Fourier map at the Fermi energy shown in figure 4.5d. The main motif of the QPI signals is streaky patterns that are diagonal with respect to q_x/q_y. The appearance of streaks gives us clues as to the origin of the signal; scattering between points/small regions of DOS localised in **k**-space would result in dispersive points in the **q**-space QPI signal (c.f. the octet model in cuprates), whereas scattering between longer parallel sections will result in streaks. The appearance of streaks is therefore consistent with the Fermi surface of CeTe₃, which consists of long, nearly parallel chains diagonal to k_x/k_y.

In figure 4.6b, it is demonstrated that the features present in the QPI map outside the first Brillouin zone are reflections/translations of the features inside. This occurs with the same periodicity and symmetry as the replication of the CDW vectors for the

Figure 4.6: Quasiparticle Interference at E_F and Dispersions of QPI channels
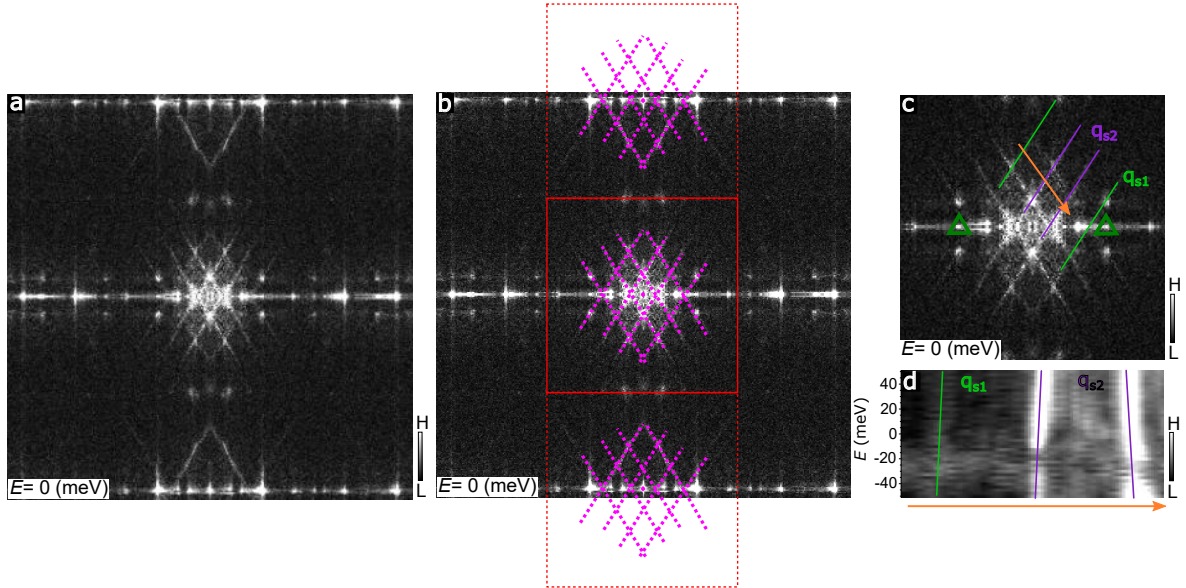
(a) Fourier transform of *dI/dV* mapping at the Fermi energy, as shown in fig 4.5d. (b) shows the same as (a), with an overlay illustrating how the features contained in the second BZ in the k_y direction are reflections/translations of the first BZ (c) closeup of the first BZ, with the two main QPI channels marked and labelled q_{s1} and q_{s2}. Green triangles indicate the $\mathbf{q'}_{CDW}$ wavevector. (d) energy vs **k** linecut taken along the line indicated by the orange arrow in b), showing the energy dispersive nature of the channels, confirming their origin as quasiparticle interference.

topographic FFT, showing that the high $|\mathbf{q}|$ QPI signals (i.e. far from Γ) are in fact low $|\mathbf{q}|$ signals that have been replicated at the Bragg peaks due to the broken translational symmetry of the surface (as discussed above in section 4.1.2). This broken symmetry means that the Γ and S high symmetry points of the 2D Brillouin zone (or equivalently the Γ and Y points of the third 3D Brillouin zone) are no longer inequivalent[a]. Due to all of the information in the QPI patterns therefore being contained within the 1st BZ, we therefore focus our attention to understanding the signals here (which will automatically allow us to understand all the other signals).

We note however the appearance of dispersive point-like signals at the upper and lower boundaries of the 1st Brillouin zone. Due to the Fermi surface having an obvious symmetry relation with this position, this scattering vector is well nested, with many possible **k**-space origins contributing to this signal. Due to the manifold nature of this QPI channel, we are unable to determine which vectors in **k**-space contribute more or less to the signal in **q**-space.

Figure 4.6c shows the first Brillouin zone of the FFT image in 4.6a, with the main observed QPI channels designated as q_{s1} and q_{s2}. An E vs **k** linecut taken normal to these channels (marked with an orange arrow) is shown in figure 4.6d with the channels

---

[a](n.b. high symmetry point notation is for the primitive orthorhombic lattice, see doi.org/10.1016/j.commatsci.2010.05.010 fig. 7 for reference)[150]

q$_{s1}$ and q$_{s2}$ marked with guides to the eye. The slope of the energy dispersion of these channels is steep, as is expected from the wide bandwidth and consequently high group velocity of CeTe$_3$, however the channels are clearly dispersive with respect to energy. This confirms their origin as scattering signals from quasiparticle interference.

q Relation between QPI and CDW Wavevectors

We briefly compare the **q**-space positions of the QPI signals and the CDW nesting vector **q**$_{\text{CDW}}$. As shown in figure 4.7, the signals are distinct from each other with no overlap. There is no observed QPI signal close to the **q**$_{\text{CDW}}$ vector, and the close up in panel 4.7 makes clear the separation between the scattering channel q$_{s1}$ and the **q'**$_{\text{CDW}}$. They remain separate over the full range of our measurement (± 50 meV), and a simple extrapolation indicates that the QPI signals will intersect the CDW wavevector far below E_F, however a quantitative determination of the value is challenging from the available data.

Figure 4.7: Comparison between CDW and QPI Wavevectors
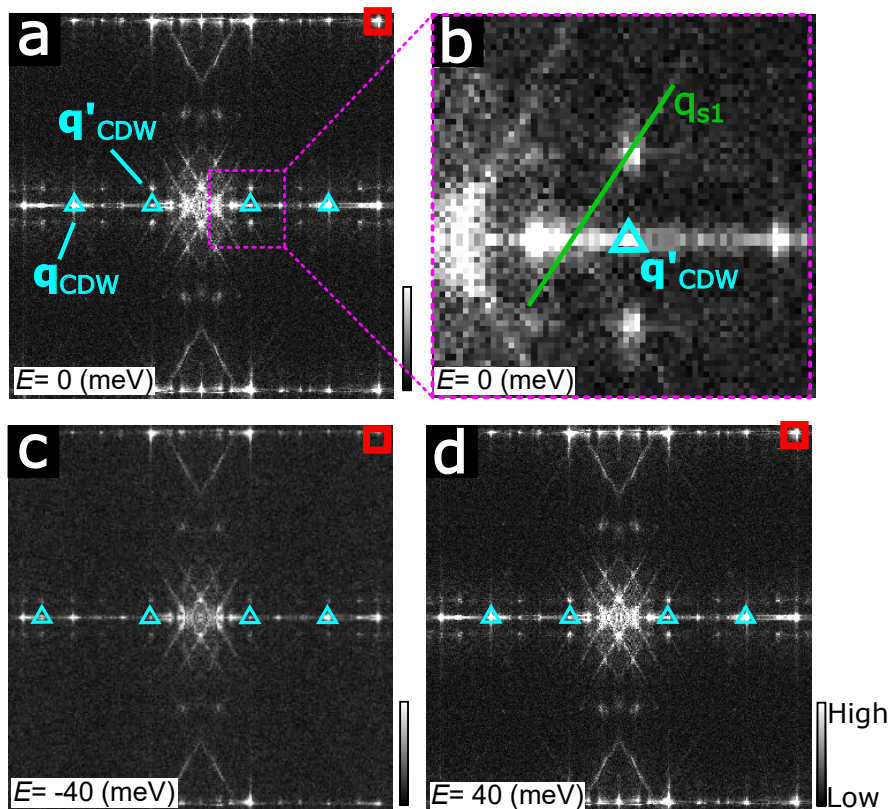
(a) QPI pattern at E_F, with Te square net Bragg peak indicated by the red square, and the **q**$_{\text{CDW}}$ and **q'**$_{\text{CDW}}$ peaks indicated with light blue triangles. (b) close up of the region indicated in (a), illustrating the difference in q_x/q_y position for the QPI and CDW peaks near Γ. (c,d) the same as (a) but for $V_b = -40$ and $+40$ mV respectively.

This observation bears mentioning as it indicates to us that the QPI channels observed near E_F have a different periodicity to the CDW, meaning that the FS nesting

giving rise to the QPI and the CDW differ. This is of course expected within the CDW energy gap, as the CDW vector gaps out the Fermi surface at momenta where the nesting is strong, meaning there are no states remaining for quasiparticle scattering to occur. A close analysis of the QPI occurring outside the CDW gap and its relation to the nesting vectors may allow us to draw conclusions about the driving force behind the CDW by giving insights into the nesting condition of the Fermi surface. Arguello et al. [120] argue that the dissimilarity of $\mathbf{q}_{CDW}$ and $\mathbf{q}_{QPI}$ is indicative of EPC being the driving force of CDW formation in 2H-NbSe$_2$, however it is by no means conclusive proof by itself. Due to the narrow energy window of the results presented in this thesis, we cannot use the relationship between the relative positions of the QPI and CDW wavevectors to draw a definitive conclusion regarding the FSN/EPC debate in RTe$_3$ and we reserve such analysis for future work.

Origin of QPI signals

To understand and explain the origin of the QPI signals, we first discuss a very basic qualitative prediction of scattering in a system with linear chains. Considering the highest spectral weight/measured DOS at E_F is from the p_x and p_z chains, it is reasonable to consider the scattering behaviour of only linear chains to begin with before moving onto the consideration of folded bands. The inter-band scattering between the p_x and p_z derived chains, while allowed, gives many possible $\mathbf{q}$ vectors with few vectors having the same direction and magnitude due to the diagonal nature of the chains. This would result in a smeared distribution across all of $\mathbf{q}$-space, being nearly indistinguishable from slightly increased background noise. Intra-band scattering however (i.e. p_x to p_x and p_z to p_z) results in many overlapping vectors of the same direction (along the chain), and many of the same magnitude (due to the same magnitude vector being able to be translated along the chain to different $\mathbf{k}_{inital}$ positions and still having a valid $\mathbf{k}_{final}$ state). These scattering vectors would result in a strong streaky channel in the QPI signal, however this basic qualitative prediction would have the streaky channel originating at $|\mathbf{q}| = 0$, which is clearly not observed in our experimental data. In fact, streaky signals that do not cross $|\mathbf{q}| = 0$ imply scattering between regions of the FS that are parallel but non-collinear. In CeTe$_3$, this corresponds to scattering between the original p orbital bands and their replicas caused by BZ folding and CDW periodicity.

4.2.2 Simulation Results

Main Band Scattering

To confirm this hypothesis, we performed joint density of states (JDOS) simulations on our calculated TB band structure. We take our CEC as a window around a certain energy, meaning that we take into account the states near E_F which have been shown to be important for the nesting condition in CeTe$_3$.[43] From this semi-constant energy contour, we then perform autocorrelation to simulate the QPI signal whilst controlling the bands that contribute to the overall result. We first simulate between only the original p orbitals, either allowing only intra-band scattering (i.e. p_x to p_x and p_z to

Figure 4.8: QPI Simulation of Scattering Between the Original *p*-orbital Derived Bands
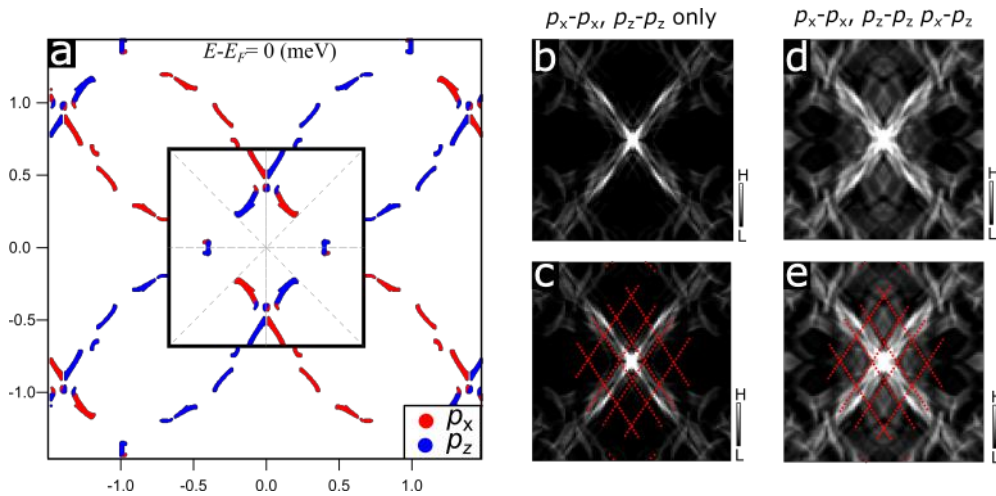
(**a**) TB simulated Fermi surface consisting of the p-orbital derived p_x and p_z chains. Black square marks the 1st 3DBZ (**b**) Simulated QPI pattern allowing only intra-band scattering from each band to itself. (**c**) The same as b), with red markers overlaid indicating the positions of the experimentally observed QPI signals. d,e) show the simulated QPI when any scattering is allowed, including the effect of inter-band scattering.

p_z) or allowing both intra-band and inter-band (i.e. p_x to p_z). The Fermi surface used for the simulations and the resulting QPI patterns are shown in figure 4.8.

From figure 4.8b and c, it is clear that the intra-band scattering causes the strong signal crossing $|\mathbf{q}| = 0$ as discussed above, and fails to replicate the experimental results. When we simulate the pattern allowing inter-band scattering (4.8d and e), we observe a higher background signal distributed throughout $\mathbf{q}$-space. We note however that both the outer q_{s1} and the inner q_{s2} experimental channel are not reproduced in the simulation. The main scattering intensity predicted is still the $|\mathbf{q}| = 0$ channel, leading us to conclude that this simulation fits the experimental data poorly, and so we expand our scattering model to include the shadow bands in order to explain our experimental observation. The potential causes for this unexpected intensity are discussed later.

Shadow Band Scattering

Figure 4.9 shows similar simulations as figure 4.8, but now with the addition of the replica/shadow bands caused by BZ folding and the CDW shadow bands, as described in methods section 2.4. The calculated Fermi surface used for these simulations is shown in figure 4.9a. Following the results of the simulation in fig. 4.8, the scattering was confined to that occurring between original and replica bands of the same orbital character.

In fig. 4.9b and c, we show the QPI pattern predicted for allowed intra-band and inter-band scattering. In this case, we see the appearance of inner and outer square features that align closely with the k_x/k_y positions of q_{s2} and q_{s1} channels, however as expected the main contribution to the predicted $\mathbf{q}$-space intensity is still derived from the intra-band scattering, with high intensity crossing $|\mathbf{q}| = 0$ and near the

Figure 4.9: QPI Simulation of Scattering Involving the Shadow Bands
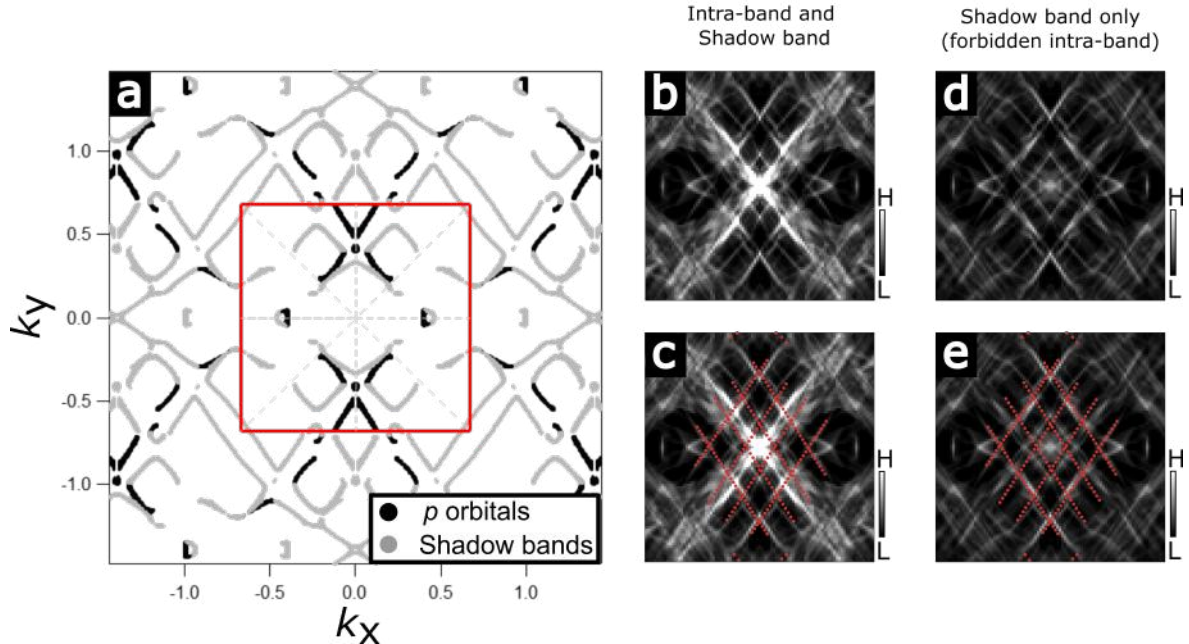
(a) Partial Fermi surface showing *p*-orbital chains in black and and their folded replica bands in grey. Red square indicates 1st BZ. (b) Simulated QPI pattern allowing intra-band scattering and scattering to/from the original bands to the shadow replica bands. (c) The same as (b), with red markers overlaid indicating the positions of the experimentally observed QPI signals. (d,e) show the simulated QPI pattern when intra-band scattering is forbidden, and only scattering to/from the original bands to the shadow bands is permitted.

corners of the 1BZ. We therefore take the reasonable next step of disallowing intra-band scattering, and simulate the QPI pattern if only scattering between the original and shadow band is allowed. This simulation is shown in 4.9d and e. We can see that this produces very close fascimilie of our experimental results. A side by side comparison between simulation and experiment to show the close correspondence is shown in figure 4.10.

Summarising the combination of these experimental and simulation results, it can be reasonably concluded that the observed quasiparticle interference in $CeTe_3$ arises from scattering between the main *p*-orbital original bands and their folded replicas, and the intra-band scattering is relatively suppressed. We will now discuss the cause of this observation.

4.2.3 Discussion of the Origin of Quasiparticle Interference Pattern

Scattering Channel Assignment

We begin our discussion through a specific assignment of the scattering vectors that give rise to each channel. By analysing the magnitude and direction of the scattering vectors

Figure 4.10: Side by Side Comparison of Simulated and Experimental QPI Pattern
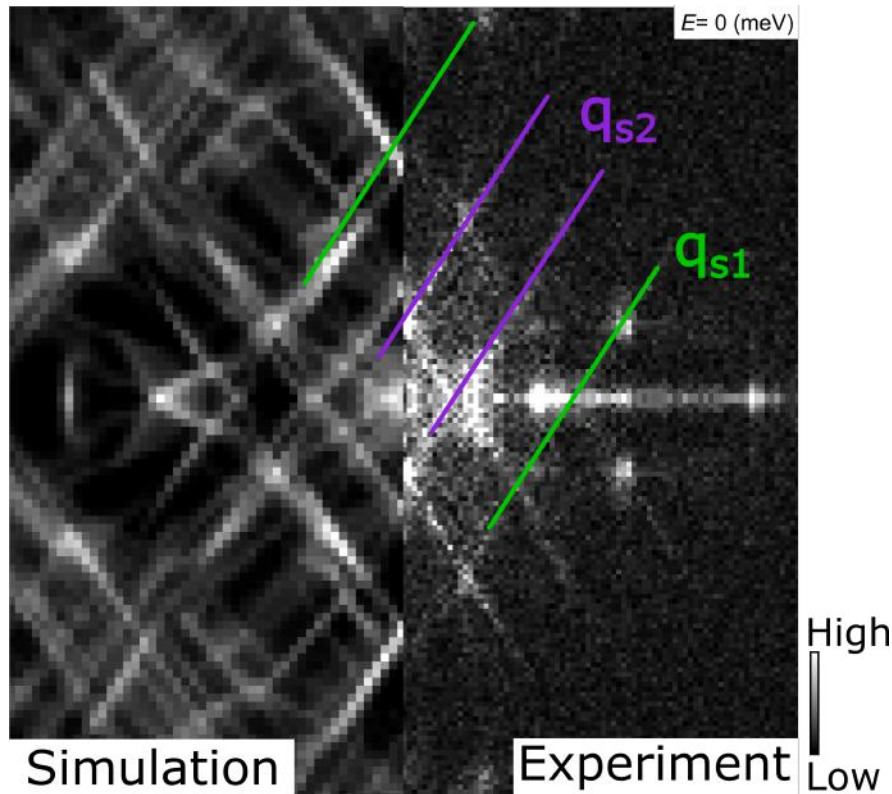
Left is the simulated QPI pattern when forbidding intra-band scattering and allowing only scattering between the original and the replica bands, right is the experimentally observed QPI pattern with overlaid markers denoting the q_{s1} and q_{s2} channels

between regions of high DOS in the FS, we can determine which scattering causes which observed QPI channel. This qualitative approach allows us to understand the origin of each channel, and importantly to interpret the cause of our non-intuitive observation. Figure 4.11 shows these vectors on the partial Fermi surface with a cartoon version of the resulting QPI pattern. The intra-band scattering (self-scattering) results in a cross centred at $\mathbf{q} = 0$, as discussed above. The scattering between the main p-orbital bands and the CDW shadow bands gives a scattering pattern resembling an x, with 4 distinct streaks crossing each other. This is the q_{s2} channel observed experimentally. Likewise, the scattering between the main p-orbital bands and the BZ folded bands consist of 4 distinct channels crossing each other, but further away from the origin. This is the q_{s1} channel observed experimentally.

These assignments are confirmed by performing JDOS simulations allowing only the scattering between the specified bands (shown in figure4.11g,h,i), which closely match the cartoon versions shown above.

Angle Dependence of QPI Scattering

As discussed above, the low $|\mathbf{q}|$ intra-band (self) scattering shown in 4.11a and b is not observed in experiment, which we can rationalise by considering the group velocity

Figure 4.11: Assignment of Scattering Vectors to QPI Channels
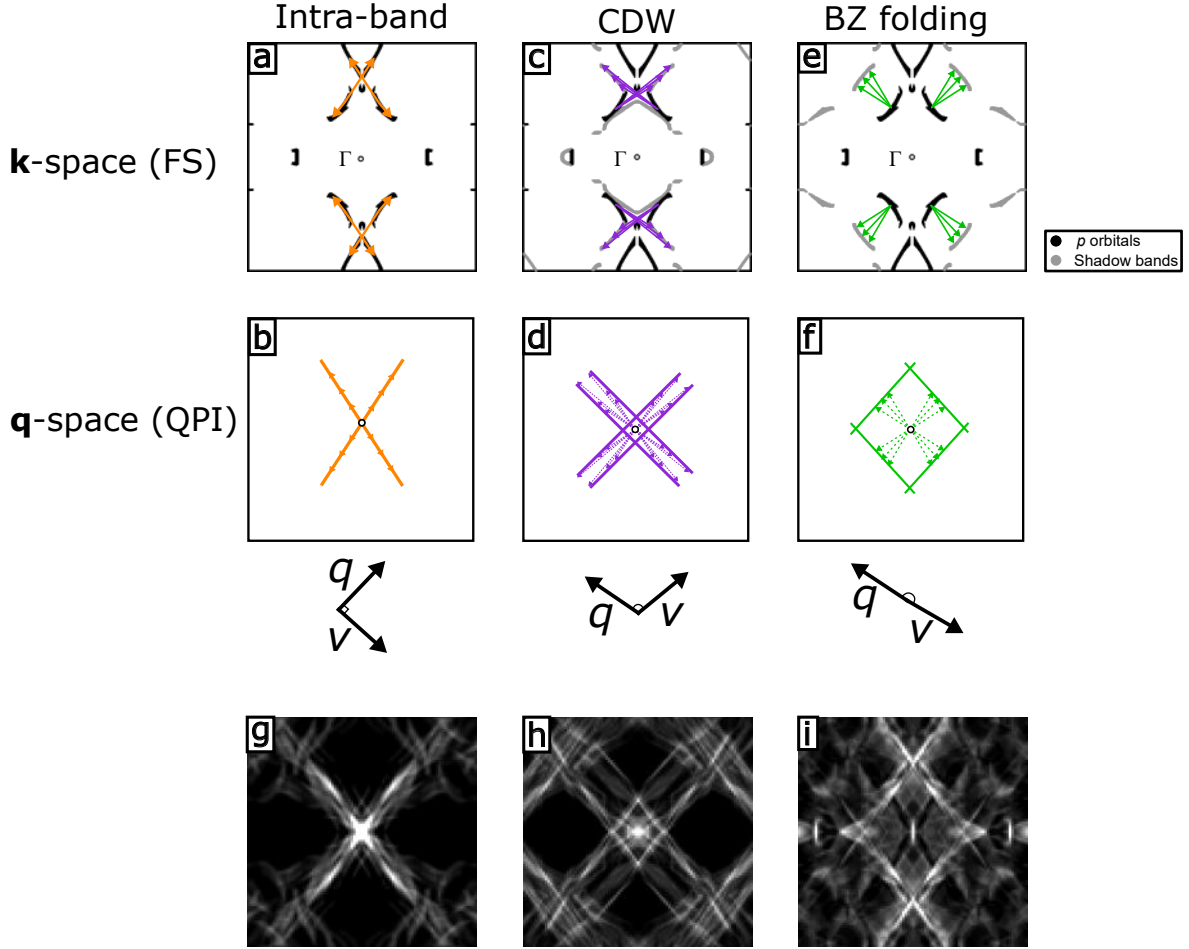
(a) Calculated partial Fermi surface for the original *p*-orbital bands with arrows marking the scattering vector direction and magnitude between these bands. (b) Scattering vectors shown in (a) mapped onto **q**-space, showing the resulting QPI pattern that would be observed. (c,d) show the scattering vectors in **k**- and **q**-space for scattering between the CDW shadow band and the original band, and (e,f) for the BZ folded replica band and the original band. (g,h,i) are the JDOS simulations allowing only the scattering in the corresponding upper panels. All image boundaries are the 1st BZ.

ν_g (or ν_F at the Fermi level) and the scattering vector **q**. It is known from analysis of the Greens function scattering matrix overlaps that the QPI scattering is relatively weaker when the scattering vector **q** and the group velocity ν_F are orthogonal to each other, and stronger when they are aligned.[151] The angular relation between **q** and ν_F for each scattering channel is shown by the arrows underneath the panels of 4.11.

Intra-band scattering (self-scattering) from one portion to another of the linear bands in $CeTe_3$ has **q** and ν_F at right angles to each other, which results in the relatively weaker scattering and absence of QPI signal near Γ. As the magnitude of $|\mathbf{q}|$ for intra-band scattering increases, the effect of the distortion of the chains will become

more pronounced and we can expect a small parallel component of ν_F and $\mathbf{q}$. This would however be a small overlap, resulting in weak scattering; combining this with the fact that scattering strength reduces monotonically with increasing $|\mathbf{q}|$, this QPI channel would be extremely weak and we cannot observe it in our measured signal. For both the q_{s1} and q_{s2} channels there is a finite overlap between $\mathbf{q}$ and ν_F, and $|\mathbf{q}|$ is relatively small. This results in higher scattering and a more intense QPI signal. The combination of both of the q_{s1} and q_{s2} scattering channels gives rise to the observed pattern.

Suppressed Backscattering

While the observed QPI pattern is possible to explain from first principles without introducing an extra physical effect, there remains a mystery to solve. Backscattering, i.e. scattering that changes the sign of the momentum of the electron, is expected to be observed between the original p-orbital bands due to their parallel nature (illustrated in figure 4.12a) and the fact that $\mathbf{q}$ and ν_F are almost totally parallel and should therefore have strong scattering. We can predict the $\mathbf{q}$-space position of the QPI signal that would arise in the same manner as before, and the positions of these expected signals are shown in fig. 4.12b and c. These expected signals are also clearly observed in the simulations that include intra-band scattering (fig. 4.8). When we compare these to the observed QPI patterns in figure 4.12c, these signals are undeniably absent, demonstrating that the backscattering of electrons in the CDW state is suppressed.

Figure 4.12: Detail of Backscattering Vectors
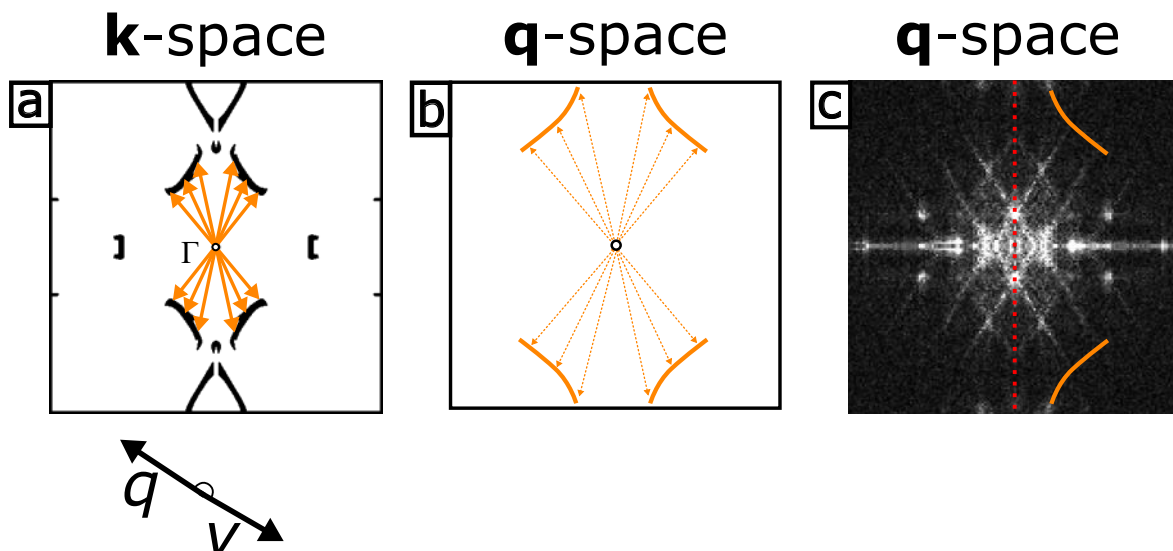
(a) Calculated partial Fermi surface for the original p-orbital bands with arrows marking the scattering vector direction and magnitude for the expected backscattering. (b) Vectors shown in (a) mapped onto $\mathbf{q}$-space, showing the resulting QPI pattern that would be observed. (c) Image is the experimental QPI pattern observed, with the predicted backscattering QPI pattern overlaid on the right hand side. All image boundaries are the 1st 3DBZ.

This suppression of backscattering explains the anomalous resistivity change when crossing T_{CDW}. As discussed in the introduction, when passing into the CDW phase a large increase of resistivity is expected, either a full metal-insulator transition for a fully gapped Fermi surface or a partial increase for a partially gapped Fermi surface. In the rare earth tritellurides, the increase in resistivity is far smaller than expected.[152] For example, a 20% increase in resistivity is observed when crossing T_{CDW1} in the material TbTe$_3$, when momentum dependant mean-field calculations predict an increase an order of magnitude higher. Kesharpu and Grigoriev [153] performed calculations using the Boltzmann transport equation and the mean-field description of the CDW state to answer this puzzle; they demonstrated that the decrease in DOS at E_F is partially compensated by a decrease in the scattering rate of the itinerant electrons. The microscopic cause of this suppressed backscattering remains unknown and requires further experimental and theoretical study.

Chapter 5

Summary and Outlook

5.1 Summary

In this thesis, we began by surveying the literature related to the rare earth tritellurides and discussed particularly their status as a model system for the study of charge density waves. We then discussed the experimental methods used to perform these investigations, with a focus on spectroscopic-imaging scanning tunnelling microscopy.

Moving on to our results, in chapter 3 we showed the optimisation of growth parameters for $CeTe_3$ and characterised the resulting single crystal samples. We measured the electronic band structure using SX-ARPES, to which we fit an interacting tight binding model. We were successfully able to reproduce the complex Fermi surface caused by the interactions of the replica/shadow bands that arise from the multiply broken translational symmetry at the surface of $CeTe_3$.

In chapter 4, we demonstrated high resolution STM/STS measurements of $CeTe_3$ at 4.2 K, evidencing the existence of the unidirectional CDW state known at higher temperatures. We also discuss spectroscopy of the surface. We then describe in detail (including simulations) the quasiparticle interference observed near E_F. We show that the QPI patterns arise not from the expected scattering between the original p_x and p_y derived bands that have the highest spectral weight, but instead are the result of scattering occurring between the original bands and the shadow/replica bands. We discuss the origins of this unexpected relative enhancement/reduction of scattering intensity, and demonstrate that backscattering in this system is suppressed in line with theoretical predictions. To our knowledge, this is the first detailed discussion of quasiparticle interference in the RTe_3 system and the first direct experimental demonstration of the suppressed backscattering.

5.2 Outlook

As has been demonstrated with the cuprates and pnictides, quasiparticle interference is an enormously powerful technique for the investigation of correlated electron physics. We hope that our pioneering work can be utilised as a stepping stone for the further investigation of charge density wave phenomena in rare earth tritellurides. The highly nested Fermi surface of these materials provides a multiplicity of nesting vectors, which

is what gives rise to the rich CDW behaviour. This multiplicity results in the possibility of the competition of electronic phases, with the resultant gap opening causing cascades of further phase changes and interactions. Combining this with the added periodicity of the exotic antiferromagnetism observed provides a particularly intriguing possibility investigate the interaction between the magnetic phases and the conduction electrons in RTe_3 by utilising lower measurement temperatures and external magnetic fields.

The work contained in this thesis is a step towards a fuller understanding of charge density waves and their interaction with other electronic phenomena, which can hopefully provide new opportunities for practical devices.

It is clear that despite much work being done to try and understand the behaviour of correlated electrons, there is much work remaining to be done.

Bibliography

[1] George Gruner. *Density waves in solids.* CRC press, 2018.

[2] John M Tranquada, Mark PM Dean, and Qiang Li. Superconductivity from charge order in cuprates. *Journal of the Physical Society of Japan*, 90(11):111002, 2021.

[3] Eduardo H da Silva Neto, Pegor Aynajian, Alex Frano, Riccardo Comin, Enrico Schierle, Eugen Weschke, András Gyenis, Jinsheng Wen, John Schneeloch, Zhijun Xu, et al. Ubiquitous interplay between charge ordering and high-temperature superconductivity in cuprates. *Science*, 343(6169):393–396, 2014.

[4] Elbio Dagotto. *Nanoscale phase separation and colossal magnetoresistance: the physics of manganites and related compounds.* Springer Science & Business Media, 2003.

[5] Kentaro Yumigeta, Ying Qin, Han Li, Mark Blei, Yashika Attarde, Cameron Kopas, and Sefaattin Tongay. Advances in rare-earth tritelluride quantum materials: Structure, properties, and synthesis. *Advanced Science*, 8(12):2004762, 2021.

[6] Shuvam Sarkar, Joydipto Bhattacharya, Pampa Sadhukhan, Davide Curcio, Rajeev Dutt, Vipin Kumar Singh, Marco Bianchi, Arnab Pariari, Shubhankar Roy, Prabhat Mandal, et al. Charge density wave induced nodal lines in $LaTe_3$. *arXiv preprint arXiv:2212.01181*, 2022.

[7] Daichi Ueta, Riki Kobayashi, Hiroki Sawada, Yuki Iwata, Shin-ichiro Yano, Shingo Kuniyoshi, Yuita Fujisawa, Takatsugu Masuda, Yoshinori Okada, and Shinichi Itoh. Anomalous magnetic moment direction under magnetic anisotropy originated from crystalline electric field in van der waals compounds $CeTe_3$ and $CeTe_2Se$. *Journal of the Physical Society of Japan*, 91(9):094706, 2022.

[8] R Okuma, D Ueta, S Kuniyoshi, Y Fujisawa, B Smith, CH Hsu, Y Inagaki, W Si, T Kawae, H Lin, et al. Fermionic order by disorder in a van der waals antiferromagnet. *Scientific Reports*, 10(1):15311, 2020.

[9] Felix Schmitt, Patrick S Kirchmann, Uwe Bovensiepen, Rob G Moore, Laurenz Rettig, Marcel Krenz, J-H Chu, Nancy Ru, Luca Perfetti, DH Lu, et al. Transient electronic structure and melting of a charge density wave in $TbTe_3$. *Science*, 321 (5896):1649–1652, 2008.

[10] L Rettig, R Cortés, J-H Chu, IR Fisher, F Schmitt, RG Moore, Z-X Shen, PS Kirchmann, Martin Wolf, and Uwe Bovensiepen. Persistent order due to transiently enhanced nesting in an electronically excited charge density wave. *Nature Communications*, 7(1):10459, 2016.

[11] Anshul Kogar, Alfred Zong, Pavel E Dolgirev, Xiaozhe Shen, Joshua Straquadine, Ya-Qing Bie, Xirui Wang, Timm Rohwer, I-Cheng Tung, Yafang Yang, et al. Light-induced charge density wave in $LaTe_3$. *Nature Physics*, 16(2):159–163, 2020.

[12] Alfred Zong, Anshul Kogar, Ya-Qing Bie, Timm Rohwer, Changmin Lee, Edoardo Baldini, Emre Ergeçen, Mehmet B Yilmaz, Byron Freelon, Edbert J Sie, et al. Evidence for topological defects in a photoinduced phase transition. *Nature Physics*, 15(1):27–31, 2019.

[13] P Walmsley, S Aeschlimann, JAW Straquadine, P Giraldo-Gallo, SC Riggs, MK Chan, RD McDonald, and IR Fisher. Magnetic breakdown and charge density wave formation: A quantum oscillation study of the rare-earth tritellurides. *Physical Review B*, 102(4):045150, 2020.

[14] Kirstine J Dalgaard, Shiming Lei, Steffen Wiedmann, Martin Bremholm, and Leslie M Schoop. Anomalous shubnikov-de haas quantum oscillations in rare-earth tritelluride $NdTe_3$. *Physical Review B*, 102(24):245109, 2020.

[15] JAW Straquadine, MS Ikeda, and IR Fisher. Evidence for realignment of the charge density wave state in $ErTe_3$ and $TmTe_3$ under uniaxial stress via elastocaloric and elastoresistivity measurements. *Physical Review X*, 12(2):021046, 2022.

[16] Yiping Wang, Ioannis Petrides, Grant McNamara, Md Mofazzel Hosen, Shiming Lei, Yueh-Chun Wu, James L Hart, Hongyan Lv, Jun Yan, Di Xiao, et al. Axial Higgs mode detected by quantum pathway interference in RTe_3. *Nature*, 606 (7916):896–901, 2022.

[17] Mohammad H Hamidian. *Imaging the Realm of the Strongly Correlated: Visualizing Heavy Fermion Formation and the Impact of Kondo Holes in URu_2Si_2*. PhD thesis, Cornell University, 2011.

[18] Stefan Kirchner, Silke Paschen, Qiuyun Chen, Steffen Wirth, Donglai Feng, Joe D Thompson, and Qimiao Si. Colloquium: Heavy-electron quantum criticality and single-particle spectroscopy. *Reviews of Modern Physics*, 92(1):011002, 2020.

[19] Christian E Matt, Harris Pirie, Anjan Soumyanarayanan, Yang He, Michael M Yee, Pengcheng Chen, Yu Liu, Daniel T Larson, Wendel S Paz, JJ Palacios, et al. Consistency between arpes and stm measurements on SmB_6. *Physical Review B*, 101(8):085142, 2020.

[20] I Battisti, WO Tromp, Sara Riccò, RS Perry, AP Mackenzie, Anna Tamai, Felix Baumberger, and MP Allan. Direct comparison of arpes, stm, and quantum

oscillation data for band structure determination in Sr_2RhO_4. *npj Quantum Materials*, 5(1):91, 2020.

[21] Chih-Wei Chen, Jesse Choe, and E Morosan. Charge density waves in strongly correlated electron systems. *Reports on Progress in Physics*, 79(8):084505, 2016.

[22] R Peierls. Zur theorie der elektrischen und thermischen leitfähigkeit von metallen. *Annalen der Physik*, 396(2):121–148, 1930.

[23] Jens Lindhard. On the properties of a gas of charged particles. *Kgl. Danske Videnskab. Selskab Mat.-Fys. Medd.*, 28, 1954.

[24] Xuetao Zhu, Jiandong Guo, Jiandi Zhang, and EW Plummer. Misconceptions associated with the origin of charge density waves. *Advances in Physics: X*, 2 (3):622–640, 2017.

[25] W Kohn. Image of the Fermi surface in the vibration spectrum of a metal. *Physical Review Letters*, 2(9):393, 1959.

[26] CW Chu, JME Harper, TH Geballe, and RL Greene. Pressure dependence of the metal-insulator transition in tetrathiofulvalinium tetracyanoquinodimethane (TTF-TCNQ). *Physical Review Letters*, 31(25):1491, 1973.

[27] LB Coleman, MJ Cohen, Do J Sandman, FG Yamagishi, Ao F Garito, and AJ Heeger. Superconducting fluctuations and the Peierls instability in an organic solid. *Solid State Communications*, 12(11):1125–1132, 1973.

[28] R Comes, SM Shapiro, G Shirane, AF Garito, and AJ Heeger. Neutron-scattering study of the 38-and 54-K phase transitions in deuterated tetrathiafulvalene-tetracyanoquinodimethane (TTF-TCNQ). *Physical Review Letters*, 35(22):1518, 1975.

[29] HA Mook and Charles R Watson Jr. Neutron inelastic scattering study of tetrathiafulvalene tetracyanoquinodimethane (TTF-TCNQ). *Physical Review Letters*, 36(14):801, 1976.

[30] Kenji Koizumi, Kyoko Ishizaka, Takayuki Kiss, Mario Okawa, Reizo Kato, and Shik Shin. Bulk-sensitive angle-resolved photoemission spectroscopy on TTF-TCNQ. *Journal of the Physical Society of Japan*, 82(2):025004, 2013.

[31] Matteo Calandra, II Mazin, and Francesco Mauri. Effect of dimensionality on the charge-density wave in few-layer 2H-NbSe$_2$. *Physical Review B*, 80(24):241108, 2009.

[32] MD Johannes, II Mazin, and CA Howells. Fermi-surface nesting and the origin of the charge-density wave in NbSe$_2$. *Physical Review B*, 73(20):205102, 2006.

[33] F Weber, S Rosenkranz, J-P Castellan, R Osborn, R Hott, R Heid, K-P Bohnen, T Egami, AH Said, and D Reznik. Extended phonon collapse and the origin of the charge-density wave in 2H-NbSe$_2$. *Physical Review Letters*, 107(10):107403, 2011.

[34] CH Du, WJ Lin, Y Su, BK Tanner, PD Hatton, D Casa, B Keimer, JP Hill, CS Oglesby, and H Hohl. X-ray scattering studies of 2H-NbSe$_2$, a superconductor and charge density wave material, under high external magnetic fields. *Journal of Physics: Condensed Matter*, 12(25):5361, 2000.

[35] DE Moncton, JD Axe, and FJ DiSalvo. Study of superlattice formation in 2H-NbSe$_2$ and 2H-TaSe$_2$ by neutron scattering. *Physical Review Letters*, 34(12):734, 1975.

[36] Anjan Soumyanarayanan, Michael M Yee, Yang He, Jasper Van Wezel, Dirk J Rahn, Kai Rossnagel, EW Hudson, Michael R Norman, and Jennifer E Hoffman. Quantum phase transition from triangular to stripe charge order in NbSe$_2$. *Proceedings of the National Academy of Sciences*, 110(5):1623–1627, 2013.

[37] Carlos J Arguello, Sreekumar P Chockalingam, Ethan P Rosenthal, Liuyan Zhao, Christopher Gutiérrez, JH Kang, WC Chung, Rafael M Fernandes, Shuang Jia, Andrew J Millis, et al. Visualizing the charge density wave transition in 2H-NbSe$_2$ in real space. *Physical Review B*, 89(23):235115, 2014.

[38] Michio Naito and Shoji Tanaka. Electrical transport properties in 2H-NbS$_2$,-NbSe$_2$,-TaS$_2$ and -TaSe$_2$. *Journal of the Physical Society of Japan*, 51(1):219–227, 1982.

[39] Joseph M Carpinelli, Hanno H Weitering, E Ward Plummer, and Roland Stumpf. Direct observation of a surface charge density wave. *Nature*, 381(6581):398–400, 1996.

[40] JM Carpinelli, HH Weitering, M Bartkowiak, R Stumpf, and EW Plummer. Surface charge ordering transition: α phase of Sn/Ge (111). *Physical Review Letters*, 79(15):2859, 1997.

[41] Rubén Pérez, José Ortega, and Fernando Flores. Surface soft phonon and the $\sqrt{3} \times \sqrt{3}$ to 3×3 phase transition in Sn/Ge (111) and Sn/Si (111). *Physical Review Letters*, 86(21):4891, 2001.

[42] D Farías, W Kamiński, J Lobo, J Ortega, E Hulpke, R Pérez, F Flores, and EG Michel. Phonon softening, chaotic motion, and order-disorder transition in Sn/Ge (111). *Physical Review Letters*, 91(1):016103, 2003.

[43] MD Johannes and II Mazin. Fermi surface nesting and the origin of charge density waves in metals. *Physical Review B*, 77(16):165135, 2008.

[44] F Weber, R Hott, R Heid, K-P Bohnen, S Rosenkranz, J-P Castellan, R Osborn, AH Said, BM Leu, and D Reznik. Optical phonons and the soft mode in 2H-NbSe$_2$. *Physical Review B*, 87(24):245111, 2013.

[45] Xuetao Zhu, Yanwei Cao, Jiandi Zhang, EW Plummer, and Jiandong Guo. Classification of charge density waves based on their nature. *Proceedings of the National Academy of Sciences*, 112(8):2367–2371, 2015.

[46] Donald W Murphy, S Sunshine, Robert B Van Dover, Robert J Cava, Bertram Batlogg, SM Zahurak, and LF Schneemeyer. New superconducting cuprate perovskites. *Physical Review Letters*, 58(18):1888, 1987.

[47] Andrea Damascelli, Zahid Hussain, and Zhi-Xun Shen. Angle-resolved photoemission studies of the cuprate superconductors. *Reviews of Modern Physics*, 75 (2):473, 2003.

[48] JM Tranquada, BJ Sternlieb, JD Axe, Y Nakamura, and Shin-ichi Uchida. Evidence for stripe correlations of spins and holes in copper oxide superconductors. *Nature*, 375(6532):561–563, 1995.

[49] Steven A Kivelson, Ian P Bindloss, Eduardo Fradkin, Vadim Oganesyan, JM Tranquada, Aharon Kapitulnik, and Craig Howald. How to detect fluctuating stripes in the high-temperature superconductors. *Reviews of Modern Physics*, 75 (4):1201, 2003.

[50] JE Hoffman, K McElroy, D-H Lee, KM Lang, H Eisaki, S Uchida, and JC Davis. Imaging quasiparticle interference in $Bi_2Sr_2CaCu_2O_{8+\delta}$. *Science*, 297(5584):1148–1151, 2002.

[51] WD Wise, MC Boyer, Kamalesh Chatterjee, Takeshi Kondo, T Takeuchi, H Ikuta, Yayu Wang, and EW Hudson. Charge-density-wave origin of cuprate checkerboard visualized by scanning tunnelling microscopy. *Nature Physics*, 4 (9):696–699, 2008.

[52] M Hashimoto, G Ghiringhelli, W-S Lee, GRETA Dellea, A Amorese, CLAUDIO Mazzoli, K Kummer, NB Brookes, B Moritz, Y Yoshida, et al. Direct observation of bulk charge modulations in optimally doped $Bi_{1.5}Pb_{0.6}Sr_{1.54}CaCu_2\ O_{8+\delta}$. *Physical Review B*, 89(22):220511, 2014.

[53] G Ghiringhelli, M Le Tacon, Matteo Minola, S Blanco-Canosa, Claudio Mazzoli, NB Brookes, GM De Luca, A Frano, DG Hawthorn, F He, et al. Long-range incommensurate charge fluctuations in $(Y,Nd)Ba_2Cu_3O_{6+X}$. *Science*, 337(6096): 821–825, 2012.

[54] J Chang, Elizabeth Blackburn, AT Holmes, Niels B Christensen, Jacob Larsen, J Mesot, Ruixing Liang, DA Bonn, WN Hardy, A Watenphul, et al. Direct observation of competition between superconductivity and charge density wave order in $YBa_2Cu_3O_{6.67}$. *Nature Physics*, 8(12):871–876, 2012.

[55] E Blackburn, J Chang, M Hücker, AT Holmes, Niels Bech Christensen, Ruixing Liang, DA Bonn, WN Hardy, U Rütt, Olof Gutowski, et al. X-ray diffraction observations of a charge-density-wave order in superconducting ortho-II $YBa_2Cu_3O_{6.54}$ single crystals in zero magnetic field. *Physical Review Letters*, 110(13):137004, 2013.

[56] R Comin, A Frano, Michael Manchun Yee, Y Yoshida, H Eisaki, E Schierle, E Weschke, R Sutarto, F He, Anjan Soumyanarayanan, et al. Charge order

driven by fermi-arc instability in $Bi_2Sr_{2-X}La_XCuO_{6+\delta}$. *Science*, 343(6169):390–392, 2014.

[57] Kazuhiro Fujita, Mohammad H Hamidian, Stephen D Edkins, Chung Koo Kim, Yuhki Kohsaka, Masaki Azuma, Mikio Takano, Hidenori Takagi, Hiroshi Eisaki, Shin-ichi Uchida, et al. Direct phase-sensitive identification of ad-form factor density wave in underdoped cuprates. *Proceedings of the National Academy of Sciences*, 111(30):E3026–E3032, 2014.

[58] KA Zinchenko, NP Luzhnaya, EI Yarembash, and AA Eliseev. Phase diagram of the Nd-Te system and phase properties. Technical report, Inst. of General and Inorganic Chemistry, Moscow, 1966.

[59] BK Norling and H Steinfink. The crystal structure of neodymium tritelluride. *Inorganic Chemistry*, 5(9):1488–1491, 1966.

[60] E Bucher, K Andres, FJ Di Salvo, JP Maita, AC Gossard, AS Cooper, and GW Hull Jr. Magnetic and some thermal properties of chalcogenides of Pr and Tm and a few other rare earths. *Physical Review B*, 11(1):500, 1975.

[61] E DiMasi, B Foran, MC Aronson, and S Lee. Quasi-two-dimensional metallic character of Sm_2Te_5 and $SmTe_3$. *Chemistry of Materials*, 6(10):1867–1874, 1994.

[62] Joshua Alan Wolfe Straquadine. *Evolution of the Charge Density Wave State in the Rare-Earth Tritellurides under Uniaxial Stress and Disorder*. PhD thesis, Stanford University, 2020.

[63] N Ru, RA Borzi, A Rost, AP Mackenzie, J Laverock, SB Dugdale, and IR Fisher. de haas–van alphen oscillations in the charge density wave compound lanthanum tritelluride $LaTe_3$. *Physical Review B*, 78(4):045123, 2008.

[64] N Ru and IR Fisher. Thermodynamic and transport properties of YTe_3, $LaTe_3$, and $CeTe_3$. *Physical Review B*, 73(3):033101, 2006.

[65] Koichi Momma and Fujio Izumi. Vesta 3 for three-dimensional visualization of crystal, volumetric and morphology data. *Journal of Applied Crystallography*, 44 (6):1272–1276, 2011.

[66] Christos D Malliakas and Mercouri G Kanatzidis. Divergence in the behavior of the charge density wave in $RETe_3$ (re= rare-earth element) with temperature and RE element. *Journal of the American Chemical Society*, 128(39):12612–12613, 2006.

[67] A Sacchetti, CL Condron, SN Gvasaliya, F Pfuner, M Lavagnini, M Baldini, MF Toney, M Merlini, M Hanfland, J Mesot, et al. Pressure-induced quenching of the charge-density-wave state in rare-earth tritellurides observed by x-ray diffraction. *Physical Review B*, 79(20):201101, 2009.

[68] J Laverock, SB Dugdale, Zs Major, MA Alam, N Ru, IR Fisher, G Santi, and E Bruno. Fermi surface nesting and charge-density wave formation in rare-earth tritellurides. *Physical Review B*, 71(8):085114, 2005.

[69] Hong Yao, John A Robertson, Eun-Ah Kim, and Steven A Kivelson. Theory of stripes in quasi-two-dimensional rare-earth tellurides. *Physical Review B*, 74(24): 245126, 2006.

[70] M Maschek, DA Zocco, S Rosenkranz, R Heid, Ayman H Said, A Alatas, P Walmsley, IR Fisher, and F Weber. Competing soft phonon modes at the charge-density-wave transitions in DyTe$_3$. *Physical Review B*, 98(9):094304, 2018.

[71] Veronique Brouet, WL Yang, XJ Zhou, Zahid Hussain, RG Moore, R He, DH Lu, ZX Shen, J Laverock, SB Dugdale, et al. Angle-resolved photoemission study of the evolution of band structure and charge density wave properties in RTe$_3$ (R= Y, La, Ce, Sm, Gd, Tb, and Dy). *Physical Review B*, 77(23):235104, 2008.

[72] G-H Gweon, JD Denlinger, JA Clack, JW Allen, CG Olson, E DiMasi, MC Aronson, B Foran, and S Lee. Direct observation of complete fermi surface, imperfect nesting, and gap anisotropy in the high-temperature incommensurate charge-density-wave compound SmTe$_3$. *Physical Review Letters*, 81(4):886, 1998.

[73] Yuwen Hu, Feipeng Zheng, Xiao Ren, Ji Feng, and Yuan Li. Charge density waves and phonon-electron coupling in ZrTe$_3$. *Physical Review B*, 91(14):144502, 2015.

[74] M Maschek, S Rosenkranz, R Heid, AH Said, P Giraldo-Gallo, IR Fisher, and F Weber. Wave-vector-dependent electron-phonon coupling and the charge-density-wave transition in TbTe$_3$. *Physical Review B*, 91(23):235146, 2015.

[75] N Ru, J-H Chu, and IR Fisher. Magnetic properties of the charge density wave compounds RTe$_3$(R= Y, La, Ce, Pr, Nd, Sm, Gd, Tb, Dy, Ho, Er, and Tm). *Physical Review B*, 78(1):012410, 2008.

[76] Nancy Ru. *Charge Density Wave Formation in Rare Earth Tellurides*. PhD thesis, Stanford University, 2008.

[77] Yuji Iyeiri, Teppei Okumura, Chishiro Michioka, and Kazuya Suzuki. Magnetic properties of rare-earth metal tritellurides RTe$_3$ (R= Ce, Pr, Nd, Gd, Dy). *Physical Review B*, 67(14):144417, 2003.

[78] K Deguchi, T Okada, GF Chen, S Ban, N Aso, and NK Sato. Magnetic order of rare-earth tritelluride CeTe$_3$ at low temperature. In *Journal of Physics: Conference Series*, volume 150, page 042023. IOP Publishing, 2009.

[79] F Pfuner, SN Gvasaliya, Oksana Zaharko, L Keller, J Mesot, V Pomjakushin, JH Chu, IR Fisher, and L Degiorgi. Incommensurate magnetic order in TbTe$_3$. *Journal of Physics: Condensed Matter*, 24(3):036001, 2011.

[80] Q Guo, D Bao, LJ Zhao, and S Ebisu. Novel magnetic behavior of antiferromagnetic GdTe$_3$ induced by magnetic field. *Physica B: Condensed Matter*, 617: 413153, 2021.

[81] Alla Chikina, Henriette Lund, Marco Bianchi, Davide Curcio, Kirstine J Dalgaard, Martin Bremholm, Shiming Lei, Ratnadwip Singha, Leslie M Schoop, and Philip Hofmann. Charge density wave generated fermi surfaces in NdTe$_3$. *Physical Review B*, 107(16):L161103, 2023.

[82] AA Sinchenko, PD Grigoriev, P Monceau, P Lejay, and VN Zverev. Slow oscillations of in-plane magnetoresistance in strongly anisotropic quasi-two-dimensional rare-earth tritellurides. *Journal of Low Temperature Physics*, 185(5-6):657–664, 2016.

[83] Mori Watanabe, Sanghyun Lee, Takuya Asano, Takashi Ibe, Masashi Tokuda, Hiroki Taniguchi, Daichi Ueta, Yoshinori Okada, Kensuke Kobayashi, and Yasuhiro Niimi. Quantum oscillations with magnetic hysteresis observed in CeTe$_3$ thin films. *Applied Physics Letters*, 117(7):072403, 2020.

[84] Bo Wang, Rui Zhou, Xuebing Luo, Yun Zhang, and Qiuyun Chen. Electronic structure study of the charge-density-wave kondo lattice CeTe$_3$. *Chinese Physics B*, 2023.

[85] V Brouet, WL Yang, XJ Zhou, Z Hussain, N Ru, KY Shin, IR Fisher, and ZX Shen. Fermi surface reconstruction in the CDW state of CeTe$_3$ observed by photoemission. *Physical Review Letters*, 93(12):126405, 2004.

[86] H Komoda, T Sato, S Souma, T Takahashi, Y Ito, and K Suzuki. High-resolution angle-resolved photoemission study of incommensurate charge-density-wave compound CeTe$_3$. *Physical Review B*, 70(19):195101, 2004.

[87] RG Moore, V Brouet, R He, DH Lu, N Ru, J-H Chu, IR Fisher, and Z-X Shen. Fermi surface evolution across multiple charge density wave transitions in ErTe$_3$. *Physical Review B*, 81(7):073102, 2010.

[88] Seungho Seong, Eunsook Lee, Yong Seung Kwon, BI Min, JD Denlinger, Byeong-Gyu Park, and JS Kang. Angle-resolved photoemission spectroscopy study of rare-earth tritelluride charge density wave compounds: RTe$_3$ (R= Pr, Er). *Electronic Structure*, 3(2):024003, 2021.

[89] Yani Chen, Peipei Wang, Minghui Wu, Jinlong Ma, Shihao Wen, Xuefeng Wu, Gaomin Li, Yue Zhao, Kedong Wang, Liyuan Zhang, et al. Raman spectra and dimensional effect on the charge density wave transition in GdTe$_3$. *Applied Physics Letters*, 115(15):151905, 2019.

[90] BF Hu, B Cheng, RH Yuan, T Dong, and NL Wang. Coexistence and competition of multiple charge-density-wave orders in rare-earth tritellurides. *Physical Review B*, 90(8):085105, 2014.

[91] A Fang, N Ru, IR Fisher, and A Kapitulnik. Stm studies of TbTe$_3$: evidence for a fully incommensurate charge density wave. *Physical Review Letters*, 99(4): 046401, 2007.

[92] A Tomic, Zs Rak, JP Veazey, CD Malliakas, SD Mahanti, MG Kanatzidis, and SH Tessmer. Scanning tunneling microscopy study of the CeTe$_3$ charge density wave. *Physical Review B*, 79(8):085422, 2009.

[93] U Ralević, N Lazarević, Andreas Baum, H-M Eiter, Rudi Hackl, Paula Giraldo-Gallo, Ian R Fisher, Cedomir Petrovic, R Gajić, and ZV Popović. Charge density wave modulation and gap measurements in CeTe$_3$. *Physical Review B*, 94(16): 165132, 2016.

[94] Alan Fang, Joshua AW Straquadine, Ian R Fisher, Steven A Kivelson, and Aharon Kapitulnik. Disorder-induced suppression of charge density wave order: Stm study of pd-intercalated erte 3. *Physical Review B*, 100(23):235446, 2019.

[95] Zhilin Xu, Shuai-Hua Ji, Lin Tang, Jian Wu, Na Li, Xinqiang Cai, and Xi Chen. Molecular beam epitaxy growth and electronic structures of monolayer GdTe$_3$. *Chinese Physics Letters*, 38(7):077102, 2021.

[96] Eunsook Lee, DH Kim, Hyun Woo Kim, JD Denlinger, Heejung Kim, Junwon Kim, Kyoo Kim, BI Min, BH Min, YS Kwon, et al. The 7× 1 fermi surface reconstruction in a two-dimensional f-electron charge density wave system: PrTe$_3$. *Scientific Reports*, 6(1):1–11, 2016.

[97] S Chillal, E Schierle, E Weschke, F Yokaichiya, J-U Hoffmann, OS Volkova, AN Vasiliev, AA Sinchenko, P Lejay, A Hadj-Azzem, et al. Strongly coupled charge, orbital, and spin order in TbTe$_3$. *Physical Review B*, 102(24):241110, 2020.

[98] H Chudo, C Michioka, Y Itoh, and K Yoshimura. Te 125 nmr studies of single-crystal CeTe$_3$. *Physical Review B*, 75(4):045113, 2007.

[99] Bert Voigtländer. *Scanning probe microscopy: Atomic force microscopy and scanning tunneling microscopy*. Springer, 2015.

[100] Julian Chen. *Introduction to Scanning Tunneling Microscopy Third Edition*, volume 69. Oxford University Press, USA, 2021.

[101] Gerd Binnig, Heinrich Rohrer, Ch Gerber, and Edmund Weibel. Surface studies by scanning tunneling microscopy. *Physical Review Letters*, 49(1):57, 1982.

[102] Davis Baird and Ashley Shew. Probing the history of scanning tunneling microscopy. *Discovering the nanoscale*, 2:145–156, 2004.

[103] John Bardeen. Tunnelling from a many-particle point of view. *Physical Review Letters*, 6(2):57, 1961.

[104] Jennifer E Hoffman. *A Search for Alternative Electronic Order in the High Temperature Superconductor BSCCO by Scanning Tunneling Microscopy.* PhD thesis, University of California at Berkeley, 2003.

[105] L Bartels, G Meyer, and K-H Rieder. Controlled vertical manipulation of single CO molecules with the scanning tunneling microscope: A route to chemical contrast. *Applied Physics Letters*, 71(2):213–215, 1997.

[106] T Hanaguri, S Niitaka, K Kuroki, and H Takagi. Unconventional s-wave superconductivity in Fe(Se,Te). *Science*, 328(5977):474–476, 2010.

[107] Pedram Roushan, Jungpil Seo, Colin V Parker, Yew San Hor, David Hsieh, Dong Qian, Anthony Richardella, M Zahid Hasan, Robert Joseph Cava, and Ali Yazdani. Topological surface states protected from backscattering by chiral spin texture. *Nature*, 460(7259):1106–1109, 2009.

[108] Hao Zheng and M Zahid Hasan. Quasiparticle interference on type-I and type-II Weyl semimetal surfaces: a review. *Advances in Physics: X*, 3(1):1466661, 2018.

[109] Nurit Avraham, Jonathan Reiner, Abhay Kumar-Nayak, Noam Morali, Rajib Batabyal, Binghai Yan, and Haim Beidenkopf. Quasiparticle interference studies of quantum materials. *Advanced Materials*, 30(41):1707628, 2018.

[110] Lan Chen, Peng Cheng, and Kehui Wu. Quasiparticle interference in unconventional 2D systems. *Journal of Physics: Condensed Matter*, 29(10):103001, 2017.

[111] A Akbari, J Knolle, I Eremin, and R Moessner. Quasiparticle interference in iron-based superconductors. *Physical Review B*, 82(22):224506, 2010.

[112] Christopher J Butler, Yu-Mi Wu, Cheng-Rong Hsing, Yi Tseng, Raman Sankar, Ching-Ming Wei, Fang-Cheng Chou, and Minn-Tsong Lin. Quasiparticle interference in ZrSiS: Strongly band-selective scattering depending on impurity lattice site. *Physical Review B*, 96(19):195125, 2017.

[113] MF Crommie, Ch P Lutz, and DM Eigler. Imaging standing waves in a two-dimensional electron gas. *Nature*, 363(6429):524–527, 1993.

[114] Ilya K Drozdov, Aris Alexandradinata, Sangjun Jeon, Stevan Nadj-Perge, Huiwen Ji, RJ Cava, B Andrei Bernevig, and Ali Yazdani. One-dimensional topological edge states of bismuth bilayers. *Nature Physics*, 10(9):664–669, 2014.

[115] Y Hasegawa and Ph Avouris. Direct observation of standing wave formation at surface steps using scanning tunneling spectroscopy. *Physical Review Letters*, 71 (7):1071, 1993.

[116] Michael F Crommie, Christopher P Lutz, and Donald M Eigler. Confinement of electrons to quantum corrals on a metal surface. *Science*, 262(5131):218–220, 1993.

[117] Tong Zhang, Peng Cheng, Xi Chen, Jin-Feng Jia, Xucun Ma, Ke He, Lili Wang, Haijun Zhang, Xi Dai, Zhong Fang, et al. Experimental demonstration of topological surface states protected by time-reversal symmetry. *Physical Review Letters*, 103(26):266803, 2009.

[118] Rahul Sharma. *Advanced Quasiparticle Interference Imaging for Complex Superconductors*. PhD thesis, Cornell University, 2020.

[119] Laurent Simon, Cristina Bena, Francois Vonau, Marion Cranney, and Dominique Aubel. Fourier-transform scanning tunnelling spectroscopy: the possibility to obtain constant-energy maps and band dispersion using a local measurement. *Journal of Physics D: Applied Physics*, 44(46):464010, 2011.

[120] Carlos J Arguello, Ethan P Rosenthal, Erick F Andrade, Wencan Jin, PC Yeh, Nader Zaki, Shuang Jia, Robert Joseph Cava, Rafael M Fernandes, Andrew J Millis, et al. Quasiparticle interference, quasiparticle interactions, and the origin of the charge density wave in 2H-NbSe$_2$. *Physical Review Letters*, 114(3):037001, 2015.

[121] Laurent Simon, François Vonau, and Dominique Aubel. A phenomenological approach of joint density of states for the determination of band structure in the case of a semi-metal studied by FT-STS. *Journal of Physics: Condensed Matter*, 19(35):355009, 2007.

[122] Andrey Kostin. *STM Imaging of Strong Orbital-Selective Correlations in FeSe*. PhD thesis, Cornell University, 2018.

[123] Kyle M Shen and JC Seamus Davis. Cuprate high-tc superconductors. *Materials Today*, 11(9):14–21, 2008.

[124] K McElroy, G-H Gweon, SY Zhou, J Graf, S Uchida, H Eisaki, H Takagi, T Sasagawa, D-H Lee, and A Lanzara. Elastic scattering susceptibility of the high temperature superconductor Bi$_2$Sr$_2$CaCu$_2$O$_{8+\delta}$: a comparison between real and momentum space photoemission spectroscopies. *Physical Review Letters*, 96 (6):067005, 2006.

[125] Michael Vershinin, Shashank Misra, S Ono, Y Abe, Yoichi Ando, and Ali Yazdani. Local ordering in the pseudogap state of the high-t c superconductor Bi$_2$Sr$_2$CaCu$_2$O$_{8+\delta}$. *Science*, 303(5666):1995–1998, 2004.

[126] Torben Hänke, Steffen Sykora, Ronny Schlegel, Danny Baumann, Luminita Harnagea, Sabine Wurmehl, Maria Daghofer, Bernd Büchner, Jeroen van den Brink, and Christian Hess. Probing the unconventional superconducting state of LiFeAs by quasiparticle interference. *Physical Review Letters*, 108(12):127001, 2012.

[127] Sangjun Lee, John Collini, Stella X-L Sun, Matteo Mitrano, Xuefei Guo, Chris Eckberg, Johnpierre Paglione, Eduardo Fradkin, and Peter Abbamonte. Multiple charge density waves and superconductivity nucleation at antiphase domain walls in the nematic pnictide Ba$_{1-X}$Sr$_X$Ni$_2$As$_2$. *Physical Review Letters*, 127(2):027602, 2021.

[128] Jinho Lee, Milan P Allan, MA Wang, J Farrell, Santiago Andrés Grigera, Félix Baumberger, JC Davis, and Andrew P Mackenzie. Heavy d-electron quasiparticle interference and real-space electronic structure of $Sr_3Ru_2O_7$. *Nature Physics*, 5 (11):800–804, 2009.

[129] Andrew R Schmidt, Mohammad H Hamidian, Peter Wahl, Focko Meier, Alexander V Balatsky, JD Garrett, Travis J Williams, Graeme M Luke, and JC Davis. Imaging the fano lattice to 'hidden order'transition in URu_2Si_2. *Nature*, 465 (7298):570–576, 2010.

[130] SD Kevan and RH Gaylord. High-resolution photoemission study of the electronic structure of the noble-metal (111) surfaces. *Physical Review B*, 36(11):5809, 1987.

[131] CI Fornari, PHO Rappl, SL Morelhão, TRF Peixoto, H Bentmann, F Reinert, and E Abramof. Preservation of pristine Bi_2Te_3 thin film topological insulator surface after ex situ mechanical removal of te capping layer. *APL Materials*, 4 (10):106107, 2016.

[132] Chun-Yeol You and Sung-Chul Shin. First-order approximations of the general magneto-optical kerr effects for an optically thin capping layer. *Thin Solid Films*, 493(1-2):226–229, 2005.

[133] Mohamed M. Atwa. *Doping Evolution of Magneto-Transport Properties in the Layered Magnetic Semimetal $Cr_{1+\delta}Te_2$*. PhD thesis, Okinawa Institute of Science and Technology Graduate University, 2022.

[134] Heinrich Hertz. Ueber sehr schnelle electrische schwingungen. *Annalen der Physik*, 267(7):421–448, 1887.

[135] Albert Einstein. Über einen die erzeugung und verwandlung des lichtes betreffenden heuristischen gesichtspunkt, 1905.

[136] Hongyun Zhang, Tommaso Pincelli, Chris Jozwiak, Takeshi Kondo, Ralph Ernstorfer, Takafumi Sato, and Shuyun Zhou. Angle-resolved photoemission spectroscopy. *Nature Reviews Methods Primers*, 2(1):54, 2022.

[137] E DiMasi, MC Aronson, JF Mansfield, B Foran, and S Lee. Chemical pressure and charge-density waves in rare-earth tritellurides. *Physical Review B*, 52(20): 14516, 1995.

[138] Akihito Kikuchi. Electronic structure of lanthan ditellurides. *Journal of the Physical Society of Japan*, 67(4):1308–1312, 1998.

[139] BI Min and Y-R Jang. Band folding and fermi surface in antiferromagnetic NdB_6. *Physical Review B*, 44(24):13270, 1991.

[140] E Kasper. Superlattices of group iv elements, a new possibility to produce direct band gap material. *Physica Scripta*, 1991(T35):232, 1991.

[141] J Voit, L Perfetti, F Zwick, H Berger, G Margaritondo, G Gruner, H Hochst, and M Grioni. Electronic structure of solids with competing periodic potentials. *Science*, 290(5491):501–503, 2000.

[142] Christos Malliakas, Simon JL Billinge, Hyun Jeong Kim, and Mercouri G Kanatzidis. Square nets of tellurium: rare-earth dependent variation in the charge-density wave of rete3 (re= rare-earth element). *Journal of the American Chemical Society*, 127(18):6510–6511, 2005.

[143] BF Hu, P Zheng, RH Yuan, T Dong, B Cheng, ZG Chen, and NL Wang. Optical spectroscopy study on cete 3: Evidence for multiple charge-density-wave orders. *Physical Review B*, 83(15):155113, 2011.

[144] Yoshiaki Sato, Shun Makiyama, Yasutaka Sakamoto, Tadahiko Hasuo, Yuji Inagaki, Tetsuya Fujiwara, Hiroyuki S Suzuki, Kazuyuki Matsubayashi, Yoshiya Uwatoko, and Tatsuya Kawae. Development of a low-temperature insert for precise magnetization measurement below T=2 K with a superconducting quantum interference device magnetometer. *Japanese Journal of Applied Physics*, 52(10R): 106702, 2013.

[145] Takayuki Muro, Yasunori Senba, Haruhiko Ohashi, Takuo Ohkochi, Tomohiro Matsushita, Toyohiko Kinoshita, and Shik Shin. Soft X-ray ARPES for three-dimensional crystals in the micrometre region. *Journal of Synchrotron Radiation*, 28(5):1631–1638, 2021.

[146] T Machida, Y Fujisawa, K Igarashi, A Kaneko, S Ooi, T Mochiku, M Tachiki, K Komori, K Hirata, and H Sakata. Visualizing the effect of structural super-modulation on electronic structure of $IrTe_2$ by scanning tunneling spectroscopy. *Physical Review B*, 88(24):245125, 2013.

[147] Felix Flicker and Jasper Van Wezel. Charge order from orbital-dependent coupling evidenced by nbse2. *Nature Communications*, 6(1):7034, 2015.

[148] Marcello Spera, Alessandro Scarfato, Árpad Pásztor, Enrico Giannini, David R Bowler, and Ch Renner. Insight into the charge density wave gap from contrast inversion in topographic STM images. *Physical Review Letters*, 125(26):267603, 2020.

[149] D Leuenberger, JA Sobota, S-L Yang, AF Kemper, P Giraldo-Gallo, RG Moore, IR Fisher, PS Kirchmann, TP Devereaux, and Z-X Shen. Classification of collective modes in a charge density wave by momentum-dependent modulation of the electronic band structure. *Physical Review B*, 91(20):201106, 2015.

[150] Wahyu Setyawan and Stefano Curtarolo. High-throughput electronic band structure calculations: Challenges and tools. *Computational Materials Science*, 49(2): 299–312, 2010.

[151] Y Kohsaka, T Machida, K Iwaya, M Kanou, T Hanaguri, and T Sasagawa. Spin-orbit scattering visualized in quasiparticle interference. *Physical Review B*, 95 (11):115307, 2017.

[152] AA Sinchenko, PD Grigoriev, Pascal Lejay, and Pierre Monceau. Spontaneous breaking of isotropy observed in the electronic transport of rare-earth tritellurides. *Physical Review Letters*, 112(3):036601, 2014.

[153] Kaushal Kumar Kesharpu and Pavel Dmitrievich Grigoriev. Temperature dependence of resistivity at the transition to a charge density wave state in rare-earth tritellurides. In *Journal of Physics: Conference Series*, volume 1238, page 012019. IOP Publishing, 2019.

Appendix A

Pump Station Design

This appendix deals with the design of the pumping station used to perform low temperature measurements with a ^{3}He fridge. Whilst this design or some variant of it undoubtedly exists in many labs around the world, documentation for the design and layout is sparse. Our homemade version has been through multiple design iterations to improve upon the performance and usability, in addition to solving unexpected and non-intuitive problems. During the set-up of our lab, the experience and knowledge used to design and make this pumping station was all based on word of mouth and grey literature. This appendix serves to rectify this lack of documentation and hopefully can serve as a guide to anyone setting up a similar system.

This simple diagram shows the valve layout for the pumping station. The system is very flexible, allowing the user to evacuate or backfill basically any part of the system desired by opening or closing different valves. The system can be vaguely considered as having an inlet manifold (inlet from dewar, 1K pot or He gas line) on the bottom half, and an outlet manifold (to either the He recovery system or to atmosphere) on the top half. The pump should be as powerful as is reasonably possible; we use a ULVAC VD40C rotary oil pump. With oil pumps, care should be taken to prevent oil suckback into the system in the event that there is a power blackout and the pump stops running but the system is still in vacuum.

The system is reasonably intuitive to use and therefore I will not explain all configurations, but I will describe the regular operation for 4 K and 1.7 K operation modes.

4 K mode

This mode involves sealing the dewar exhaust via V1 and utilises a spring loaded check valve to build a consistent small positive pressure head at the top of the dewar. This forces LHe through the 1K pot while avoiding the vibrational noise and possible temperature fluctuations associated with pumps.

Open: V1, V3, V7, V6, V9. All other valves closed. Pump switched off.

1.7 K mode

This mode uses the pump to create a vacuum head in the 1K pot, reducing the temperature to 1.7 K as described in the methods section. The dewar has a positive pressure head just as for 4 K mode.

Open: V1, V3, V9, V8, V2, V13. All other valves closed. Pump switched on.

71

Figure 1: Pumping Station Valve Diagram
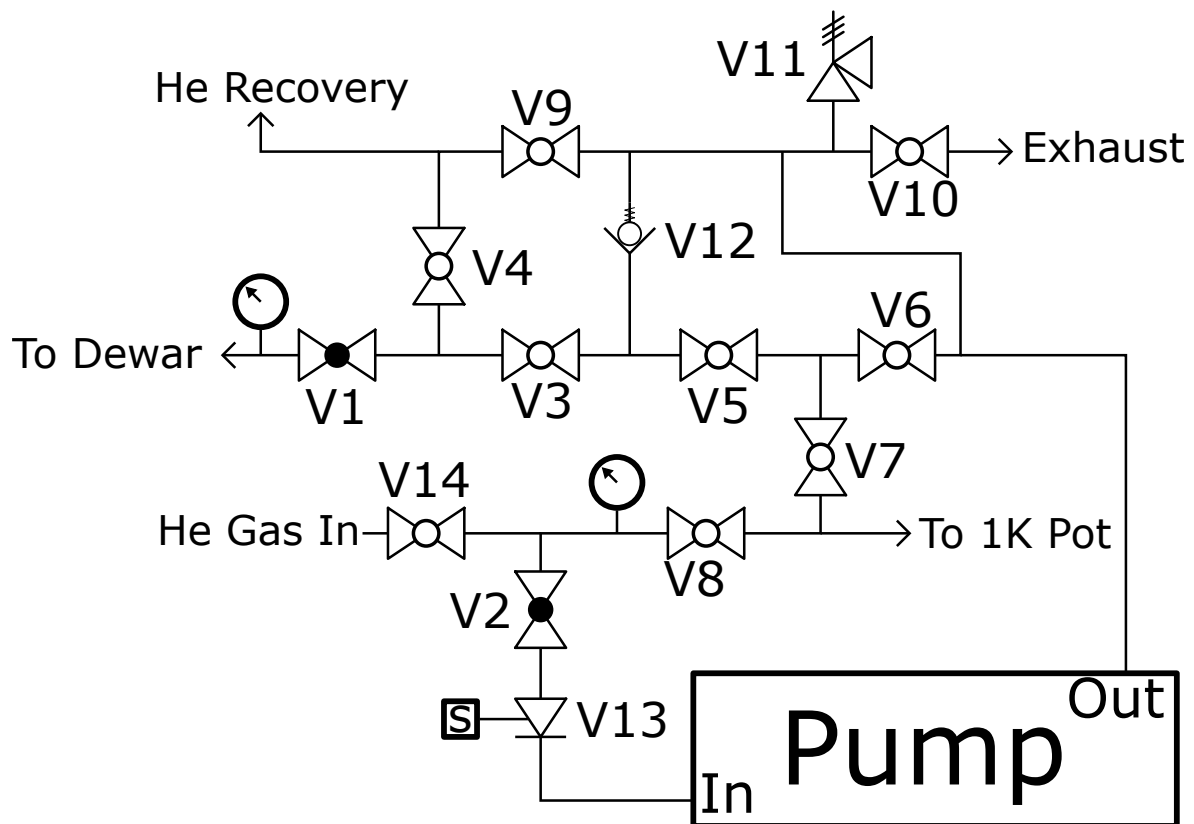
Valve diagram of pumping station. V11 is an overpressure safety valve, V12 is a 1/3 PSI Spring check valve to allow a consistent positive pressure in the dewar, V13 is a solenoid powered check valve that closes in the event of power outage to prevent oil backstreaming into the system.

Our systems use a mixture of globe, ball and diaphragm valves. As long as the valves are reasonably high quality, the choice should not be a critical one.

Figure 2: Photograph of Pumping Station

Photograph of one of the pumping stations in our lab. Note the pump and V13 are contained within the box at the bottom of the image.

Appendix B

Alternate QPI Dataset Comparison

This appendix compares the QPI dataset discussed in the main body with other partial datasets collected under the same conditions, to both demonstrate repeatability and to determine which peaks in the FFT maps are artefacts arising from periodic noise. From this comparison we can conclusively establish that those peaks highlighted in green in 3a are artefacts arising from periodic noise. We also demonstrate the repeatability of these measurements by showing datasets collected on different crystal samples and using different STM instruments, which show the same QPI patterns.

Figure 3: Comparison of Different Datasets for Repeatability

Exp 1 - Symmetrised

Exp 1 - Raw

Exp 2

Exp 3

(a) FFT map at E_F for $CeTe_3$, symmetrised around $k_y = 0$ and $k_x = 0$. This is the dataset used in the main body of this thesis. Artefacts caused by periodic noise are highlighted in green. (b) Raw dataset (i.e. not symmetrised) of the map shown in (a). (c) FFT map at E_F collected using a different single crystal sample and a different tip, collected 3 months after the dataset shown in (a,b). No artefacts like those highlighted in (a) are seen, however cross-like artefacts arising from performing an FFT on a distorted real-space image are present. (d) FFT map at E_F collected using a different single crystal sample and a completely separate STM instrument to the previous two datasets.